Characterizing Sediment Transport and Stability in Remote River Systems

by

Andrew Clow

A thesis
presented to the University of Waterloo
in fulfillment of the
thesis requirement for the degree of
Master of Applied Science
in
Civil Engineering

Waterloo, Ontario, Canada, 2020

Author's Declaration

This thesis consists of material all of which I authored or co-authored: see Statement of Contributions included in the thesis. This is a true copy of the thesis, including any required final revisions, as accepted by my examiners.

I understand that my thesis may be made electronically available to the public.

Statement of Contributions

Important contributions were provided toward the completion of this thesis by Dr. Bruce MacVicar and Winston Wade (SNC-Lavalin Inc.) by providing direction and technical expertise.

I certify, with the above qualifications, that this thesis and research in which it refers is the product of my own work.

Abstract

Canada is a large country with vast networks of linear infrastructure, such as roads and pipelines, that unavoidably intersect with water ways. Engineers must be able to characterize geomorphologic processes and channel stability for the design of infrastructure at water crossings. This process is not always straightforward. Water crossings frequently occur in remote locations which makes access for collecting field data difficult and poses an increased health and safety risk to field staff. Stream stability is closely linked to sediment transport and both remain difficult to parameterize due to extreme sensitivities to estimates of discharge, thresholds of motion, inter-particle dynamics, and flood history. The uncertainty around precipitation and flows has been heightened with the onset of climate change as events that used to be considered "extreme" are becoming more common place.

A field program and modelling framework (Alluvial Stability Indexing Model (ASIM)) were developed to be used alongside existing spatial and hydrological modelling software to expand the capabilities of SNC-Lavalin Inc. to provide additional information to decision makers for the design of linear infrastructure at crossings with alluvial systems. ASIM allows for sediment transport to be assessed in relatively remote and hence poorly parameterized channels over different time scales and climate scenarios. Sediment transport is linked to channel stability and relative stability can be characterized within a river network at the reach scale. The field program supports ASIM by incorporating less time-intensive measurements of surficial sediment characteristics and channel geometry using advancements in unmanned aerial vehicle (UAV) technology and photogrammetry software.

Chauncey Creek was used as the river catchment to test the field program and it was confirmed that grain size distribution (GSD) and geometry data can be collected quickly in places with limited access or elevated health and safety risks. Data from a UAV was shown to be within an accuracy of 1 - 5% without georeferenced control markers and three passes of survey locations were sufficient to collect high resolution photos and data 3-D models. The comparisons between Wolman pebble counts, paint-and-pick, and photosieving showed that photos from UAVs can be analyzed with BASEGRAIN to acquire GSDs within 8% Ψ. The channel properties in Chauncey Creek appear to follow reasonable relationships relative to a stream power index and simplifications were made for modelling purposes.

ASIM was shown to perform similarly to a model developed by G. Parker (2004) and total continuity of mass was maintained. A scenario that matched conditions measured in the field for Chauncey Creek showed that the slope, elevation, and dominant grain size in the steepest sections would change to the greatest degree. Different flow scenarios suggest that the model approaches a common future, but the extent and speed of the changes depend on the magnitude and recurrence of floods. Different geometrical scenarios show that widening a channel could have more noticeable impacts downstream than narrowing a channel, but this conclusion will likely depend on sediment loading and channel geometry in neighbouring reaches.

Acknowledgements

I would like to thank Dr. Bruce MacVicar for providing me with the opportunity to study with him and for all of his understanding throughout my entire process of completing a master's degree. I would also like to thank Winston Wade and the water resources team at SNC-Lavalin Inc. for putting their faith in me, supporting me in the field, and making sure having fun was a mandatory activity.

I would like to thank the University of Waterloo, SNC-Lavalin Inc. and Mitacs for providing financial support through the Mitacs Accelerate Program.

I would like to thank my friends, family, and staff and fellow students at the University of Waterloo for making the last two years enjoyable and helping me through any hard times.

Table of Contents

List of Figures

List of Tables

Abbreviations

ASIM Alluvial Stability Indexing Model iv, v, xii, 58–64, 68, 69, 72–74, 77, 80–82, 84, 109–114

BC British Columbia xi, 20, 21, 25, 26

CDEM Canadian Digital Elevation Model 40, 49, 50, 74

DEM digital elevation model 3, 11, 12, 24, 25, 40, 50, 56, 74

GCP ground control point 32

GIS Geographic Information System 3, 40

GSD grain size distribution iv, xi, 3, 9, 11, 18–20, 23–25, 27, 29–32, 34, 35, 37–39, 41, 42, 44–46, 51, 52, 55–57, 59, 61, 62, 74–79, 82, 85, 96, 103, 106, 109–111, 113, 114, 137

NHN National Hydrographic Network 40, 74

SfM Structure-from-Motion 3, 19, 31–34, 40

UAV unmanned aerial vehicle iv, 3, 4, 18, 20, 23–25, 31, 33, 34, 38, 40, 48, 50, 56, 109, 114

List of Symbols

α coefficient of material transferred to the substrate as the river bed aggrades 64

α_r Manning-Strickler resistance coefficient 65

δ_j change in elevation of the interface between the active layer and substrate at node j (m) 71

η bed surface elevation (masl) 63

η_{int} elevation of the interface between the active layer and substrate (masl) 71

λ wavelength of light (μm) 34

λ_p sediment porosity (%) 63

μ grain size distribution median 43, 45

ν kinematic viscosity (m^2/s) 15

ω specific stream power (W/m^2) 8

ω' stream power index 45

ω_c critical specific stream power (W/m^2) 16

$\phi_{i,j}$ regression variable for the ith size class in reach j 67

Ψ classification system unit for grain size measurements 28, 38, 39

Ψ_{ci} centre of the i^{th} size class (Ψ) 39

Ψ_i particle size of the i^{th} size class (Ψ) 43

Ψ_m arithmetic mean of Ψ measurements from a grain size distribution (Ψ) 39, 74, 75

Ψ_x x^{th} percentile of a particle-size distribution (Ψ) 39

ρ fluid density (kg/m^3) 8

ρ_s sediment density (kg/m^3) 14

σ grain size distribution sorting coefficient 43, 45

τ total boundary shear stress averaged over the width of the river (N/m^2) 8

τ^* Shields stress (dimensionless shear stress) 14, 16

τ_c^* critical Shields stress (critical dimension shear stress) 14, 16

τ_c critical shear stress (N/m^2) 15

$\tau_{sg,j}^*$ Shields number based on the surface geometric mean size in reach j 66

$\tau_{ssrg,j}^*$ critical Shields number in reach j calculated from the surface sand fraction 66

A_C catchment area (km^2) 41

$A_{C,j}$ catchment area upstream of reach j (km^2) 61

$A_{C,M}$ catchment area upstream of the hydrological model location (km^2) 61

A_j river area linked to the elevation of node j (m^2) 68

A_s sample area (mm^2) 29

a_u upwinding coefficient 64

b_{blur} motion blur (px) 34

$b_{i,j}$ hiding function for size class i in reach j 67

D diameter of bed material particles (m) 7

D_{50} median grain size (mm) 29, 45

D_{gi} geometric mean size of the ith size class (mm) 35

D_{gm} geometric mean of grain size distribution (mm) 39

D_i representative diameter of the ith size class (mm) 67

$D_{pass,i}$ passing sieve size for the ith size class (mm) 44

$D_{ret,i}$ retaining sieve size for the ith size class (mm) 44

d_{dif} diffraction limit (μm) 34

F_i fraction of surface material in the ith size class (%) 63

$F_{s,j}$ surface sand fraction in reach j (%) 65

f focal length width (mm) 31

f_{ci} converted proportion of a sample in the ith size class 35

$f_{l,i}$ fraction of sediment exchanged between the substrate and surface material in the ith size class (%) 63

f_{oi} observed proportion of a sample in the ith size class 35

$f_{s,i,int,j}$ fraction of material in the top substrate layer in the ith size class in reach j (%) 64

G_{Ψ_i} frequency of a Gaussian distribution for the ith size class 43

g acceleration due to gravity (m/s^2) 8

h camera height above ground (m) 31

l ground sample distance (mm) 31

j counting variable describing the index of a reach or node 72

k counting variable describing the time step 72

$k_{s,j}$ roughness height in reach j (m) 65

k_u kurtosis of a distribution 44

L_a active layer thickness (m) 63

$L_{a,j,old}$ active layer thickness from the previous time step in reach j (m) 64

L_s maximum thickness of substrate layers (m) 69

l_j length of reach j (m) 67

M_j elevation of the interface between the active layer and substrate at node j (masl) 69

m total number of time steps 72

$m_{\%i}$ percentage frequency by weight for particles retained in the ith size class (%) 39

N_{f-stop} f-stop of the aperture 34

n total number of reaches 72

n_a active layer coefficient 65

n_k roughness height coefficient 65

n_p number of particles 29

n_s number of grain size classes 35

p_{bi} bedload transport fraction for the ith size class (%) 63

Q_b bedload discharge (m^3/s) 7

$Q_{bT,j}$ total bedload transport rate in reach j (m^2/s) 67

$Q_{down,j}$ change in total sediment flow in the reach downstream of node j (m^3/s) 68

$Q_{up,j}$ change in total sediment flow in the reach upstream of node j (m^3/s) 68

Q_w water discharge (m^3/s) 7

$Q_{w,j}$ river flow in reach j (m^3/s) 61

$Q_{w,M}$ river flow at the hydrological model location (m^3/s) 61

q_b unit bedload discharge by immersed weight 16

q_b^* dimensionless bedload transport rate 16

$q_{bi,j}$ unit bedload transport rate for the ith size class in reach j (m^2/s) 67

q_{bT} total unit bedload transport rate (m^2/s) 63

$q_{w,j}$ river flow per unit width in reach j (m^2/s) 65

R submerged specific gravity of sediment 66

R_{Di} frequency of a Rosin distribution for the ith size class 44

R_e shear Reynolds number 15

R_h hydraulic radius (m) 8

S channel slope (m/m) 7

S_{det} camera sensor pixel width (μm) 31

S_j channel slope in reach j (m/m) 65, 66

s grain size distribution sorting coefficient 44

s_G grain size distribution sorting coefficient for calculating ideal Gaussian distribution 43

s_k skewness of a distribution 44

s_R grain size distribution sorting coefficient for calculating ideal Rosin distribution 44, 75

T_j total sediment thickness including the active layer and substrate in reach j (m) 72

t time after start date (s) 63

t_{ss} shutter speed (s) 34

u river velocity averaged over the cross-section (m/s) 8

u_* shear velocity (m/s) 15

$u_{*,j}$ shear velocity in reach j (m/s) 65

u_c critical shear velocity (m/s) 15

V total sediment volume in the model domain (m^3) 72

v drone velocity (mm/s) 34

$W^*_{i,j}$ dimensionless unit bedload transport rate for the ith size class in reach j 67

w channel width (m) 8

w_{ac} active channel width (m) 41

w_j width of reach j (m) 67

Δx distance between nodes assuming a constant nodal spacing along the entire domain (m) 64

x_e integer dimension required for converting between different grain size distribution methods 35

Chapter 1

Introduction

Canada is the second largest country in the world with vast networks of linear infrastructure including over 1,000,000 km of roads, 75,000 km of railways, 110,000 km of large diameter pipelines, and 840,000 km of pipelines in total (Natural Resources Canada, 2016b; Central Intelligence Agency, 2019). With 9% of the area in Canada covered by water (Central Intelligence Agency, 2019), infrastructure often has to cross river networks with the aid of bridges or through burial. Despite the commonality of river crossings, Canada covers an area with 15 distinguishable hydrological ecozones (Statistics Canada, 2018), which means that engineers have to design for a diverse set of criteria, and sufficient data is not always available. The Water Survey of Canada is the national hydrometric program that curates the data collected at publicly funded hydrometric gauges and only 2,100 stations are currently active (Environment and Climate Change Canada, 2020), most of which are located near urbanized areas. Infrastructure design requires knowledge about the potential for geomorphological changes to alluvial systems such as aggradation, degradation, local scour, general scour, channel migration, and avulsion. These changes are closely tied to channel geometry, flow regime, stream stability, sediment supply, and sediment transport capacity. Predicting the rate of sediment transport and stream stability remains difficult to parameterize due to extreme sensitivities to estimates of discharge, thresholds of motion, interparticle dynamics, and flood history (Wohl, 2015; Saletti et al., 2015; Petit et al., 2015).

Uncertainty in the field of fluvial geomorphology is further heightened by potential changes to climate at the global scale and land-use. Modern climate change has been widely accepted (IPCC, 2014), but the consequences of these changes, specifically to river morphology, are not completely understood (Spencer & Lane, 2017). Canada will be highly susceptible to global warming and climate change because of impacts on glacier melting rates, permafrost layers, snowmelt events, and precipitation seasonality (Bush et al., 2019). While global temperature trends predict a gradual rise in average temperature across the globe (Liverman, 2009; New et al., 2011; Lynas, 2008), precipitation estimates are less consistent (IPCC, 2014). There has been a national upward trend in precipitation in Canada since the 1950s, but local trends and seasonality of precipitation can vary regionally (Environment and Climate Change Canada, 2017). Canada is also a country that has experienced a gradual trend toward a higher percentage of people living in urban areas and away from rural areas (Statistics Canada, 2015). As this trend continues, there will be a change in land-use toward urbanization and impermeable land surfaces. These land-use changes add another degree of uncertainty that has been shown to have a significant impact on the channel flows and sediment loads (Hollis, 1975; Brabec et al., 2002).

Research is underway around the world to transform the way decisions are made around rivers. With the increasing availability of digital elevation models (DEMs) with fine resolutions, it is possible to quickly determine a watershed drainage area, the stream channel network, and channel slope (Tarboton et al., 2009; Schwanghart & Kuhn, 2010; Roux et al., 2015; Sangireddy et al., 2016). With this basic information, it is possible to estimate cumulative flows using empirical relations (Wilson et al., 2007; López-Vicente et al., 2014) or to link Geographic Information System (GIS) with hydrologic models for more sophisticated predictions of discharge (Arnold et al., 1998; Olivera et al., 2006; Nielsen et al., 2017). Technology is also allowing researchers to collect surficial grain size distribution (GSD) information more rapidly. What historically required manual measurements (Wolman, 1954; Leopold, 1970; Bunte & Abt, 2001) was shown to be feasible through the use of automated photosieving (Detert & Weitbrecht, 2012; Purinton & Bookhagen, 2019) and low-cost unmanned aerial vehicles (UAVs) (Woodget & Austrums, 2017; Carbonneau et al., 2018). Photogrammetry and Structure-from-Motion (SfM) algorithms allow high-resolution DEMs to be affordably developed at the local scale (Smith et al., 2015; Clapuyt et al., 2016; James et al., 2017).

The goal of this research is to quantify the hazard of event-based and long-term geomorphological change to linear infrastructure that is in proximity to or cross alluvial water channels, so engineers and property owners are better-informed to make decisions regarding the design and maintenance of infrastructure. The research is broken down into two separate objectives. The first objective is to develop a modelling framework that will allow sediment transport to be characterized over different time scales and climate scenarios in regions that are difficult to access and therefore require more resources to parameterize. The second objective is to design a field program where sufficient information can be collected to parameterize geomorphologic conditions for modelling purposed while limiting the complexity of measurements and time required of personnel in the field. These objectives are combined to expand the environmental services that SNC Lavalin Inc. (SNC Lavalin) are able to provide while striving to limit additional time spent in the field and processing data. The modelling framework was designed to be used in conjunction with software that is already being used by SNC Lavalin for existing projects, and the field program utilizes consumer-grade UAVs or phone cameras to quickly collect photos that can be used to determine channel geometry and bed particle sizes. The software that will be used alongside the development of the modelling framework include the following:

- FAST is an in-house software tool currently being used and developed by SNC-Lavalin. FAST is a vital tool in processing large amounts of data as it allows for automated retrieval of flow and climate data from Environment Canada's system of climate stations and HYDAT database. FAST also provides users with the ability to readily create hydrologic model inputs (for Raven – described below) and discretize catchment basins. The intention is to add functionality to this tool throughout the modelling process.

- Raven is a hydrological modelling framework developed at the University of Waterloo. Raven provides users full customization of the hydrological processes and spatial discretization to design a hydrological model with the simplicity or complexity appropriate to each project. Many hydrologic processes are specific to cold regions, such as Canada, and are available in Raven (Chernos et al., 2017).

The results of this research could support engineering consultants by providing a less labour intensive field protocol for characterizing geomorphological properties of alluvial river channels. This would provide economic benefits by reducing field visit expenses and limiting exposure to hazards associated with field visits such as working near moving water and in remote locations. The numerical model could be used with a range of climate scenarios and sediment transport equations to characterize the range of outcomes and the degree of uncertainty. A more well-informed decision with regards to engineering and maintenance means less risk to infrastructure and environment.

Chapter 2

Literature Review

2.1 River Characterization

Researchers and professionals use different methods to characterize rivers, both qualitatively and quantitatively, in an attempt to describe physical and biological processes across a wide range of fields of study (Downs & Gregory, 2004). For example, aquatic biologists may be interested in water quality and sediment calibre, drinking water providers in availability and water quality, and hydraulic engineers in flow regimes and channel geometry, to name but a few. The focus of this research was directed toward geomorphologic and hydraulic characterization of natural river systems in regions where field access is difficult and channels are relatively steep ($> 3\%$ slope). Most of the river systems of interest are alluvial. Alluvial systems flow in channels comprised of alluvium, which is sediment eroded and transported by the rivers themselves.

2.1.1 Channel Properties

A key concept for describing geomorphological processes in alluvial systems is the graded river. First proposed by Mackin (1948), the graded river concept suggests that a river will naturally adjust its flow path, and therefore slope, to maintain a balance between river flow and sediment transport. This concept was further developed by Lane (1955), who presented the following relationship:

$$Q_w \cdot S \propto Q_b \cdot D \tag{2.1}$$

where Q_w is the water discharge (m^3/s), S is the channel slope (m/m), Q_b is the bedload transported by the river (m^3/s), and D is the diameter of the sediment particles in transport (m). Additional terms, including channel depth and critical Shields number, were added to Equation 2.1 by Eaton and Church (2011). By characterizing these variables, the geomorphology and hydraulic geometry of a river can be described.

The discharge in a river can be described relative to hydraulic geometry following a variety of methods. One method is to use the "bankfull discharge" which is sometimes, but not always, synonymous to the "dominant discharge" (G. P. Williams, 1978; Hey & Thorne, 1986; Czech et al., 2016). Bankfull discharge is the discharge that flows in a full channel without over-topping the banks and partially flowing over the floodplain, but specific definitions describing how to locate the banks and recurrence rate of this discharge vary (G. P. Williams, 1978; Downs & Gregory, 2004; Gregory & Madew, 1982). The definition used for dominant discharge can also be described as the flow "associated with the peak of cumulative sediment transport for a given streamflow magnitude and frequency of occurrence. It is the discharge that is generally doing the work (sediment transport) that results in the average morphologic characteristics of alluvial channels" (García, 2008a, p. 1093).

In highly mobile alluvial channels, another option is to follow the definition of an active channel, which is described by Liébault and Piégay (2001, p. 171) as "the portion of the bed regularly (once or several times a year) disturbed by flow" (Church, 1992). With this definition, the channel width varies over time and is dependent on bedload transport as well as river flow. In scenarios where the bed load is reduced without drastic changes to river flow, the active channel would decrease in size as bedforms stabilize (S. A. Schumm, 1977; Liébault & Piégay, 2001). Using this definition involves locating the edge-of-bank at the boundary of vegetation growth (Alber & Piégay, 2011; Liébault & Piégay, 2001).

Channel slope is not always explicitly defined as to how it is measured and can follow the energy grade line, water surface, or the surface of the bed (Lane, 1955; Hey & Thorne, 1986; Julien & Wargadalam, 1995), but the slope is typically measured at the bed level and averaged over a set distance (Charlton, 2007). Some researchers use measurements at the vegetation line or high-water mark elevation as the river slope (S. P. Rice & Church, 2001).

Two other river characteristics that are relevant for the characterization of bedload sediment transport are the boundary shear stress and specific stream power. Boundary shear stress is the force that acts on the channel bottom due to the weight of the water moving over its surface (García, 2008a). For the case of steady, uniform flow, boundary shear stress is described as:

$$\tau_b = \rho g R_h S \tag{2.2}$$

where ρ is the fluid density (kg/m^3), g is the acceleration due to gravity (m/s^2), and R_h is the hydraulic radius (m). In channels that have a width greater than 20 times the depth, the hydraulic radius is approximately equal to the flow width (García, 2008a). Alternative methods are used for non-uniform flows but require more information (Charlton, 2007; Chansen, 1999; Sturm, 2010).

Specific stream power represents the amount of work a river can exert on the channel averaged over the channel width (Bagnold, 1966). Specific stream power is calculated with one of the following equations:

$$\omega = (\rho g Q_w S)/w \tag{2.3}$$

$$\omega = \tau u \tag{2.4}$$

where ω is the specific stream power (W/m^2), w is the channel width (m), τ is the total boundary shear stress averaged over the width of the channel (N/m^2), and u is the river velocity averaged over the cross section (m/s) (Petit et al., 2005). Going forward, specific stream power, or stream power per unit width, will be referred to as stream power. First proposed by Bagnold (1977) as an alternative predictor of bedload transport, stream power has the benefit that detailed knowledge of depth and velocity is not required for its measurement when using Equation 2.3 (Ferguson, 2005), and it was found to be more highly correlated to sediment transport intensity than average shear stress and depth-averaged velocity (C. Parker et al., 2011). Stream power can also be used to anticipate changes in stream processes such as incision and aggradation (DiBiase & Whipple, 2011; Ferencevic & Ashmore, 2012; Lague, 2014).

The calibre of sediment is often described using the diameter of particles that make up the GSD of surface sediment. Figure 2-1 depicts the surface layer which only includes sediment that is exposed to the flowing water (Church et al., 1987; Bunte & Abt, 2001). Surface roughness is a descriptor of the resistive force that sediment has on flowing water and is often characterized by a dominant particle size that is multiplied by a scalar (Kamphuis, 1974; G. Parker, 2006; Powell, 2014). The "dominant" particle size is typically a relatively large particle within a GSD or the geometric mean.

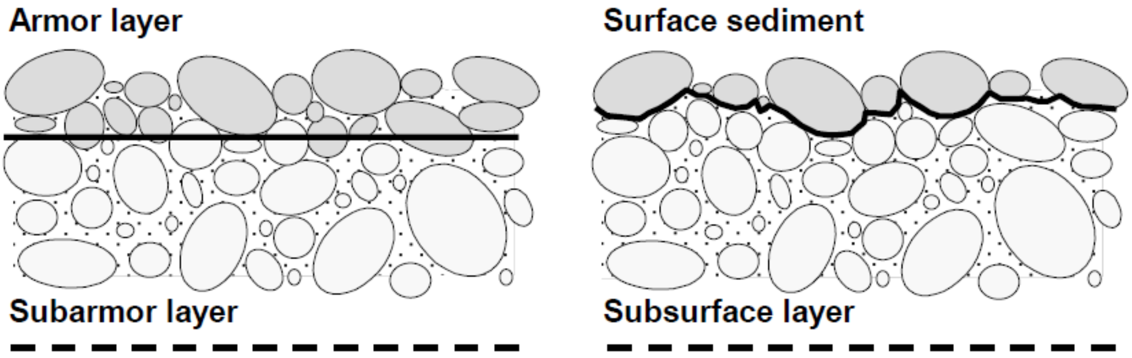

Figure 2-1: Depiction of particles included in the surface sediment; from Bunte and Abt (2001).

2.1.2 Channel Form

Researchers classify rivers into channel types using a combination of qualitative and quantitative observations to convey what river processes can be expected to be observed (S. A. Schumm, 1985; Nanson & Croke, 1992; Downs & Gregory, 2004). Leopold and Wolman (1957) first introduced a river type classification system that distinguishes between rivers that are straight, meandering and braided. This classification system was then further refined to include anabranching channels by Nanson and Knighton (1996). Figure 2-4 depicts different channel types and relative properties. Although channels are often described using

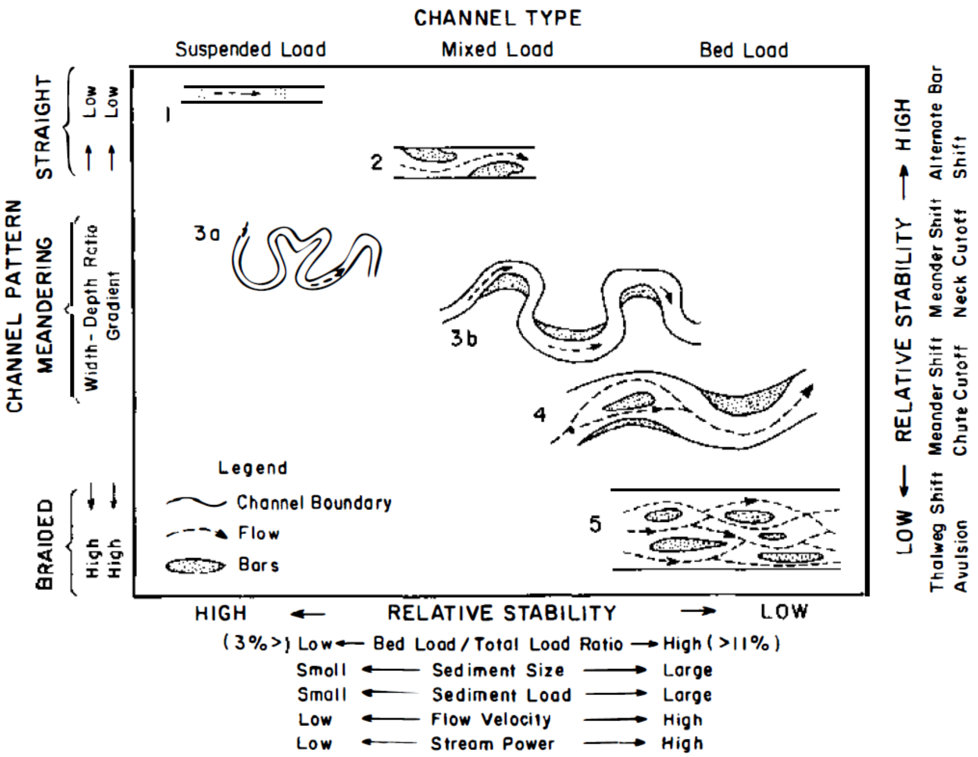

Figure 2-2: Channel classification based on pattern and type of sediment load, showing types of channels, their relative stability, and some associated variables; from S. A. Schumm (1985).

discrete categories, it must be remembered that these represent a continuum, and there is often overlap between the channel types (Downs & Gregory, 2004; Charlton, 2007). To minimize the subjective nature of classification systems, researchers have developed thresholds to distinguish between the channel types. Stream power was used by van den Berg (1995) and Kleinhans and van den Berg (2011), who characterized lower thresholds for the more mobile channel types with braided being the most mobile.

2.1.3 Reach Segmentation

A river's hydraulic geometry and channel type will vary along their length as the slopes change, and additional water and sediment loads are added to the system. Rivers are commonly discretized into reaches that are river sections with relatively uniform characteristics (García, 2008b). Similar to the general characterization of a river, the reach segmentation process can be done using an array of variables depending on the field of study. Methods for delineating reaches within the field of fluvial geomorphology include defining local controls and slope transitions (Bevan et al., 2018), channel and valley width discontinuities (Alber & Piégay, 2011), gravel bar formation (Martínez-Fernández et al., 2019), or inputs of abundant water and sediment (S. P. Rice & Church, 2001). To highlight the latter, S. P. Rice and Church (2001) introduced the idea of "sediment links". A sediment link is a river segment that is delineated based on water and sediment load sources such as alluvial fans from mountainsides, large tributaries, and non-alluvial inputs. Within each sediment link, the channel slope and surficial GSD show well defined downstream trends that explain some of the noise observed in downstream trends when characterizing a river channel as a whole.

There is some inherent subjectivity in existing methods for segmenting reaches, but some automation techniques have been applied to make the process more objective. Martínez-Fernández et al. (2019) completed a study that looked at various ways to automatically segment rivers by using aerial photographs, DEMs, and discharge data. The results of this study showed that primary geomorphic variables (channel gradient and active channel width) were the most straightforward data to acquire and effective at segmenting a river compared to stream power and sediment transport capacity when looking at river processes such as gravel bar formation. Alber and Piégay (2011) describe another quantitative delineation methods that is based on channel slope, watershed area, valley bottom width, and active channel width discontinuities. Their method follows a two-step process. The river is first disaggregated into evenly sized segments (10, 25, or 100 m lengths) before characterizing the river in each segment. The segments are then aggregated into broader reaches with homogeneous parameters.

2.1.4 Basin-Wide Processes

Channel properties in natural rivers are geographically variable and tend to follow specific processes in the downstream direction. The most indisputable is a decrease in elevation, which leads to increases in drainage area and often flow. Linking back to Mackin's (1948) version of a graded relationship (Equation 2.1), an increase in flow could correspond to a decrease in slope, increase in sediment calibre or bedload transport rate, or a combination of all three. The change in slope usually becomes more gradual downstream, and the elevation profile in the longitudinal direction of rivers are concave-up in shape (Leopold & Maddock Jr., 1953; Snow & Slingerland, 1987). Average bed material grain sizes typically decrease gradually from boulders to gravel until a sharp transition to sand occurs (Mackin, 1948; Knighton, 1980; S. Rice, 1998). These processes were visualized by Church (1992) and are shown in Figure 2-4.

Headwater regions are sometimes referred to as the production zone and are where most of the sediment in a river originates (Charlton, 2007). Sediment ranging in size from silt and clay to large boulders can enter stream channels from steep hillslopes (Dietrich & Dunne, 1978; Benda & Dunne, 1997; An et al., 2017). Headwater regions often have a supply of sediment that exceeds the capacity of a river to transport the material and are described as "transport-limited". The downstream areas in rivers are usually "supply-limited" and have a transport capacity that exceeds the supply of sediment (Charlton, 2007; García, 2008b). Although rivers typically have an increase in sediment transport capacity in the downstream direction, specific stream power and a river's capacity to move large sediment decreases as a result of changes in slope and channel width. Sediment originating in production zones supply the bed material for the entire length of a river, and changes in the headwater could correspond to changes in stability and habitat downstream (Liébault & Piégay, 2001; Neupane & Yager, 2013; Ferrer-Boix & Hassan, 2014).

Measuring the hydraulic geometry of an entire river system in the field can be very time consuming, and the resolution of most readily available DEMs is too coarse to allow estimation of channel width and depth from topography (Cazorzi et al., 2013). One way around this is to use empirical relationships that describe hydraulic variables relative to discharge (Leopold & Maddock Jr., 1953). Leopold and Maddock Jr. (1953) found that

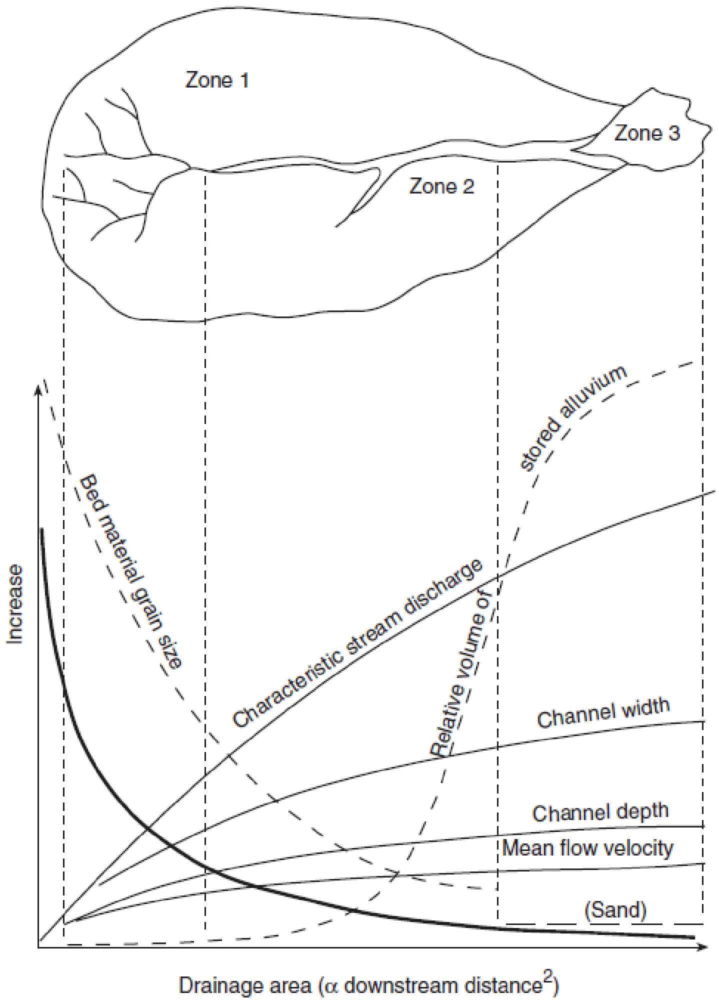

Figure 2-3: Schematic representation of the variation in channel properties through a drainage basin. Zone 1 represents the headwaters and production zone, Zone 2 represents the transfer zone, and Zone 3 represents the zone of deposition; from Charlton (2007); original source Church (1992); based on a concept from S. A. Schumm (1977).

a power function with the form aQ^b could be fitted to describe the channel width, depth, mean velocity, and suspended sediment. The coefficients a and b vary for each variable and from one system to another. Other researchers found that a single power function did not address every system evenly, so other relationships were proposed with combinations of flow, median grain size, and slope with varying success (Bray, 1982; Julien & Wargadalam, 1995; Julien, 2015; Gholami et al., 2017). Relating hydraulic geometry to flow is convenient because the flow has also been correlated closely with the catchment area (Wolman & Leopold, 1957; Leopold et al., 1964), and the power-law relationships relating channel width to discharge hold for catchment areas in mountainous regions (Julien, 2015; Sofia et al., 2015). These relationships would not eliminate the need to obtain field measurements unless an empirical relationship has already been validated for the given region. However, this simplified approach means fewer measurements along the length of a river would be necessary if no data is available.

2.2 Bedload Sediment Transport

2.2.1 Incipient Motion and Thresholds

Researchers often use the flow condition described as incipient motion to predict when the transport of surface sediment in alluvial channels will occur. As the flow in a river increases, so too does the force it applies on sediment. Incipient motion occurs when the force of water is just strong enough to move sediment (Shields, 1936; Dey, 1999; Dey & Ali, 2019). Researchers have described a range of threshold values for hydraulic conditions that correspond to the incipient motion of sediment particles. A threshold for incipient motion was first proposed by Shields (1936), who described it in terms of the dimensionless shear stress. The dimensionless shear stress (τ^*) is commonly referred to as the Shields stress and is calculated from:

$$\tau^* = \frac{\tau}{(\rho_s - \rho)gD} \tag{2.5}$$

where ρ_s is the specific gravity of the sediment (kg/m^3) (Shields, 1936). The critical Shields stress (τ_c^*) is the threshold value of Shields stress for incipient motion and was shown to be dependent on the shear Reynolds number:

$$R_e = u_* D/\nu \tag{2.6}$$

where R_e is the shear Reynolds number, u_* is the shear velocity (m/s), and ν is the kinematic viscosity (m^2/s). The relationship between critical Shields stress and shear Reynolds number becomes constant for large particles, but a broad range of values have been measured in flumes and nature (Andrews, 1983; Petit et al., 2015; Dey & Ali, 2019). Researchers have found the critical Shields stress can depend on a variety of factors, including the relative size of other surface particles, which is often described as the "hiding factor" (Einstein, 1950; G. Parker & Klingeman, 1982; Andrews, 1983; Ferguson, 1994), relative roughness (flow depth/surface roughness) (Buffington & Montgomery, 1997; Shvidchenko & Pender, 2000; Lamb et al., 2008; Prancevic & Lamb, 2015), and slope (Mizuyama, 1977; Rickenmann, 2001; Hassan et al., 2005; Lamb et al., 2008; Prancevic & Lamb, 2015).

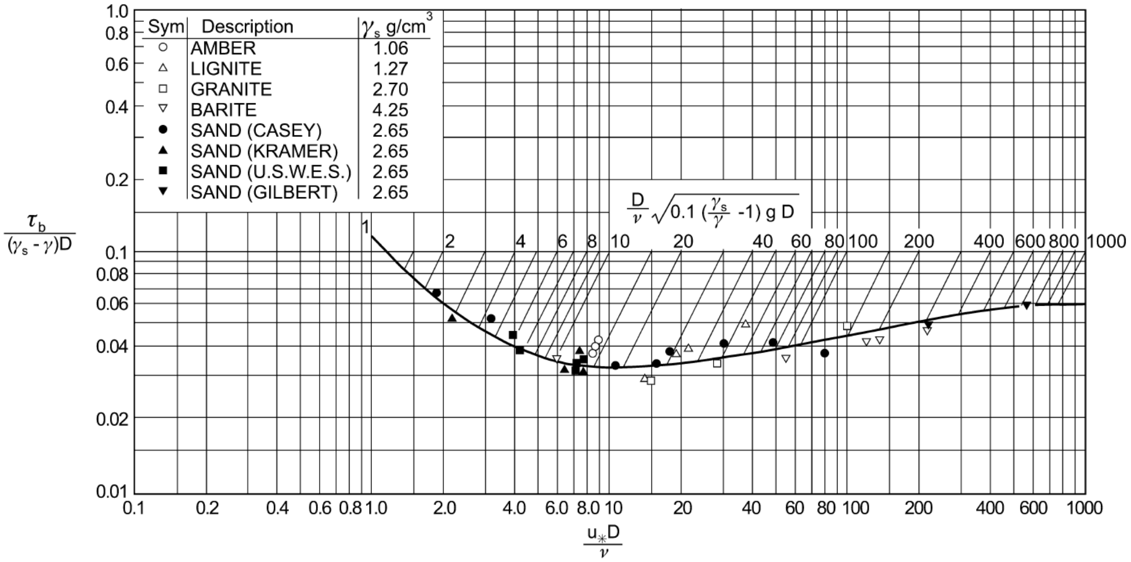

Figure 2-4: Shields diagram for initiation of motion; from García (2008a); original source Vanoni (1964).

Bagnold (1977) introduced the use of specific stream power to describe the threshold of sediment entrainment as an alternative to shear stress. This threshold equals the product of critical shear stress (τ_c) and critical shear velocity (u_c) and is now commonly described as the critical specific stream power ($\omega_c = \tau_c u_c$). Bagnold (1980) derived a relationship between critical stream power, particle diameter, and flow depth that was used for predicting incipient motion to varying degrees of success (G. Williams, 1983; Ferguson, 2005; Petit et al., 2005). Similar to critical Shields stress, critical stream power is dependent on hiding effects and bed sorting (Ferguson, 2005; C. Parker et al., 2011) but was found to be independent of slope and relative roughness (C. Parker et al., 2011; Ferguson, 2012; Prancevic & Lamb, 2015). Ferguson (2005) presented an updated equation for critical stream power that is more versatile as it accounts for hiding effects, relies on the slope instead of channel depth, and distinguishes between particle sizes in transport and the bed.

2.2.2 Sediment Transport Intensity

Sediment transport intensity of the bedload can be predicted using similar hydraulic characteristics to those used to describe incipient motion. The most common method applied today uses shear stress and was first proposed by Meyer-Peter and Müller (1948):

$$q_b^* = 8(\tau^* - \tau_c^*)^{3/2} \tag{2.7}$$

where q_b^* is the dimensionless bedload transport rate, τ^* is the Shields stress, τ_c^* is the critical Shields stress (Mueller et al., 2008). A common stream power method was presented by Bagnold (1980) and later modified by Martin and Church (2000):

$$q_b = 0.0139(\omega - \omega_c)^{3/2}(D^{1/4}/d) \tag{2.8}$$

where q_b is the unit bedload transport by immersed weight and ω_c is the critical specific stream power (W/m^2). Whether based on shear stress or stream power, approaches that use thresholds are very sensitive to how the threshold is selected (Martin & Ham, 2005). The major drawback of using these methods is that downstream fining trends cannot be modelled because individual grain sizes are not distinguished.

Equations that predict the sediment transport rate for individual particle size classes are described as fractional sediment transport equations and are also calculated using thresholds. G. Parker (1990) presented a fractional sediment transport equation that was suitable for coarse sediment, but a second model had to be used if high proportions of sand were also present (Cui & Parker, 2005). Wilcock and Crowe (2003) presented a new equation that could be used for a more extensive range of sediment sizes. This version has seen wide-spread use in 1-D models that predict elevation change and sediment transport (Lewicki et al., 2007; Viparelli et al., 2010; Müller & Hassan, 2018). To address one of the shortcomings of Wilcock and Crowe (2003), Yager et al. (2007) and Yager et al. (2012) presented a version that is more suitable for steep channels.

2.2.3 Basin-Wide Models

River catchments are routinely modelled using hydrologic models to predict the magnitude of flows for a variety of climactic scenarios (Arnold et al., 1998; Chernos et al., 2017), but sediment transport models for the purposes of characterizing stream stability at a basin scale are less common. 2-D and 3-D sediment transport models such as HEC-RAS, iSIS, and Mike21C work well for small reaches, but the processes are difficult to scale to a full river basin (United States Bureau Reclamation, 2006; Wu & Wang, 2007). Morphological models cover a range of applications to include habitat, hydrology, and morphologic processes through mostly qualitative approaches (Rinaldi et al., 2013; Belletti et al., 2015). Researchers have also described channel stability with qualitative approaches in the form of channel evolution models (S. A. Schumm, 1984; Hawley et al., 2012; Cluer & Thorne, 2014).

Most 1-D numerical models that simulate aggradation and degradation can be described as decoupled models, where flow and channel bed characteristics are updated separately at each time step (Cui et al., 1996; Lewicki et al., 2007). Sediment transport relationships that use shear stress (G. Parker, 1990; Wilcock & Crowe, 2003) were integrated into a 1-D decoupled sediment transport model by Cui et al. (1996) and G. Parker (2004). Cui et al.'s (1996) approach has been verified through flume studies (An et al., 2017) and used to study sediment loading regimes (Müller & Hassan, 2018). This model has also been used at the basin scale to understand the impact of urbanization on bed material transport (Lewicki et al., 2007) and the effects of loading from tributary sources on fish habitat (Neupane & Yager, 2013). Other 1-D sediment transport models that are decoupled include BESMo (Müller & Hassan, 2018), BASEMENT (Radice et al., 2012; Vetsch et al., 2018), RubarBE (El Kadi Abderrezzak et al., 2008; El Kadi Abderrezzak & Paquier, 2009; Camenen et al., 2018), and SETRAC (Chiari et al., 2010). Coupled models have been used, but involve a more complex numerical solution through the inclusion of continuity and momentum equations (Rahuel et al., 1989; Wu & Wang, 2007; Cao et al., 2004; Wickert & Schildgen, 2019; Papanicolaou et al., 2004).

A 1-D energy approach was used by C. Parker et al. (2015) who introduced the model ST:REAM, which characterizes stability based on the relative stream power in reaches compared to neighbouring reaches. Soar et al. (2017) proposed a River Energy Audit Scheme which follows a similar approach to ST:REAM, but uses a measurement of annual energy in excesses of the critical stream power as an indicator. The River Energy Audit Scheme requires GSD information to calculate critical stream power and excess energy, so an extensive sediment sampling program was required for the study region. The stream power has been used for incision models by predicting rates of incision from the drainage area and slope of a river, but this is applied to bedrock channels (Whipple & Tucker, 1999; Lague, 2014)

2.3 Field Methods for Measuring Surficial Grain Size Distributions

Characterizing the surficial sediment layer in alluvial channels is critical for understanding geomorphological characteristics because it is a dominant variable for calculating the sediment transport intensity and surface roughness. Methods for characterizing the surficial layer in the field vary because of the range of possible scenarios and particle size ranges that can be encountered. The GSD in gravel-bed rivers (D $\geq$8 mm) have traditionally been measured at discrete locations using grid sampling techniques such as Wolman pebble counts (Wolman, 1954; Leopold, 1970) or areal sampling (e.g. paint-and-pick, photosieving) (Bunte & Abt, 2001). These methods involve a large amount of field work, so researchers have assessed the potential for emerging technologies related to imaging and laser scanning to develop faster methods that maintain the accuracy of traditional methods. Recent improvements to software, camera, and UAV technology has led to the advent of automated and more rapid methods for characterizing surficial GSD. Photosieving can now be partially automated using software such as BASEGRAIN (Detert & Weitbrecht, 2012) or Pebblecounts (Purinton & Bookhagen, 2019). Another technique used to identify the GSD from a photo is autocorrelation. Autocorrelation uses photos with known GSDs to develop relationships between statistical properties in photos, such as a contrast and pixel intensity to particle size. These relationships can, in turn, be used to approximate particle sizes in photos with unmeasured GSDs (Rubin, 2004; Warrick et al., 2009).

Besides automated methods for looking at individual photos, photogrammetry and SfM techniques can be used to make 3D from a series of 2D images and have also been applied to GSD characterization. SfMs models can be used directly through the use of properties such as the standard deviation of bed elevations (Aberle & Nikora, 2006; Detert et al., 2017) or indirectly with photogrammetry software (Carbonneau et al., 2018). One of the most notable improvements in GSD characterization is advent of spatially continuous GSDs using roughness parameters from 3D models (Woodget & Austrums, 2017; Vázquez-Tarrío et al., 2017; Neverman et al., 2019). These methods also make it easier for defining entire catchments at a lower budget (Dugdale et al., 2010). Laser scanners are more accurate than SfM, but the difference depends on camera quality (Detert et al., 2017) and are more expensive.

2.4 Summary of Research Gaps

The field of geomorphology is developing quickly and new technologies for modelling sediment transport and measuring grain size distributions in the field are becoming more feasible. The research presented in this study highlight a gap in the literature surrounding the link between rapid field measurements and models for sediment transport and channel evolution. This study tries to address this gap through the development of a system that would provide engineers the ability to assess stability around stream courses in a way that decisions around infrastructure can be made with more confidence. A new system would also present the opportunity to test it for field cases to assess its practicality and functionality.

Chapter 3

River Section and Particle Size Characterization

3.1 Field Methods

A field program was designed to provide a dataset of basin-wide river characteristics for the calibration of the sediment transport model. The field program utilizes recent technological improvements in measuring GSDs by using a UAV to reduce the amount of time personnel had to spend in the field.

3.1.1 Study Area: Chauncey Creek

The Rocky Mountains are located in Canada and the US and are oriented in a north-south direction, forming the continental divide through the southern part of BC and Alberta. Major transportation networks pass through the Rocky Mountains, and the steep slopes lead to a high number of river channels that need to be crossed by roads, rail networks, and pipelines. The selected study area, Chauncey Creek, is a typical river catchment within the Rocky Mountains and undergoes geomorphic processes that are common in mountainous regions. Mountain channels often lie in narrow flood plains with steep channels and hillslopes ($\geq$10%), and abundant supplies of sediment enter the channels directly from the hillslopes.

Chauncey Creek is located near the town of Elkford in BC, and the basin lies on the west side of the BC border with Alberta. The creek flows in a south-westerly direction toward the Fording River and away from the mountain ridge that parallels the provincial border. The surficial geology of the local ecodistrict is a thin and discontinuous till (Agriculture and Agri-Food Canada, 2013). The downstream boundary of the selected Chauncey Creek region is located 600 m upstream from the confluence with the Fording River. The catchment area above the downstream boundary covers an area of 34.4 km^2 and is shown in Figure 3-1. The slopes in the catchment area are quite steep with an average channel slope of 7% and an average hillside slope of 40%.

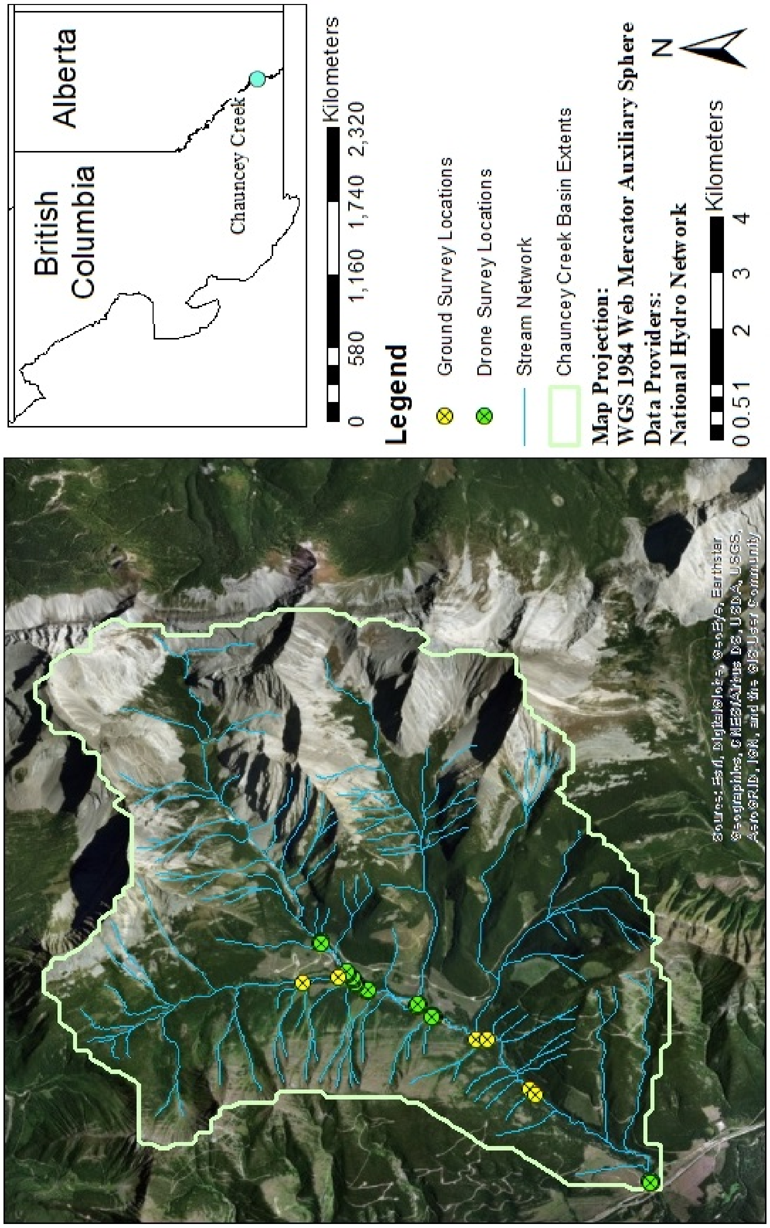

Figure 3-1: Chauncey Creek catchment extents

The Chauncey Creek basin was selected for this study because of a few desirable characteristics:

1. Chauncey Creek is a headwater stream with an abundant large supply of sediment from steep hill slopes. Aerial photos show that the creek erodes through large alluvial fans for the initial 3 km. There is also the added benefit that there is no upstream alluvial source of sediment except for the hill slopes that needed to be defined.
2. The profile of the main channel is shown in Figure 3-2 and has an overall concave-up shape with two distinct sections (Natural Resources Canada, 2016a). A 1 km region splits the two sections with large alluvial fans, which increase the sediment load to the downstream section. Three large tributaries flow into Chauncey Creek between 4 km and 6 km from the upstream boundary and provide additional point sources of water and sediment. The slope averages 10.1% and 3% upstream and downstream of the confluence, respectively (Figure 3-3). The change in slope from the top of the river to the outlet results in a measurable difference to GSD throughout the basin which is desirable for identifying sediment links and testing sorting processes in the modelling framework.
3. There are minimal direct anthropogenic impacts on the catchment, except an access road and a few acres of cleared trees. The absence of infrastructure means that the river basin would be formed by unregulated floods and natural processes.
4. Chauncey Creek flows through an alluvial channel. Alluvial channels are unrestricted to degrade to the depth of bedrock, and no exposed bedrock was found in the lower 5 km of main channel during the field program.

The locations for UAV surveys were chosen to cover a range of locations spread along the channel with a focus on confluence locations. Two major side tributaries were identified, and surveys were located upstream and downstream of both locations. A survey was completed near the downstream boundary of Chauncey Creek before it flows under a bridge and into Fording River. A washed-out bridge near the top of Chauncey Creek was also surveyed. Figure 3-1 shows the locations of UAV surveys and additional ground locations

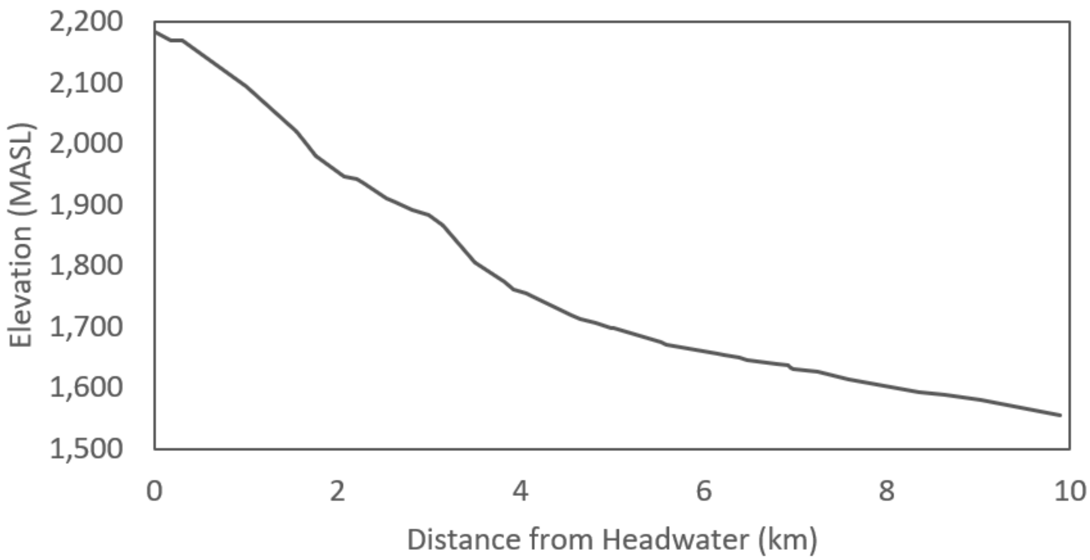

Figure 3-2: Chauncey Creek channel elevation; elevations derived from DEM data from Natural Resources Canada (2016a)

where qualitative notes were taken within the extents of the Chauncey Creek catchment. The survey locations were all situated in areas with limited tree cover to allow for a safe flight path for the UAV and to photograph broad areas of exposed sediment.

3.1.2 Test Areas: Elk River and Mamquam River

There are many different ways of measuring surficial GSDs with different approaches leading to relatively coarser or finer estimates of the distribution parameters (Bunte & Abt, 2001). The modelling described in this thesis uses the Wilcock and Crowe (2003) sediment transport equations, which were developed using GSD measurements directly comparable to physical sieving with square-hole sieves. Various researchers have compared photosieving analyses to physical sieves and summarized the relationships that can be used for equivalent comparisons (Strom et al., 2010; Graham, Reid, & Rice, 2005). Field measurements were taken to confirm the relationships shown by Strom et al. (2010) and Graham, Reid, and Rice (2005).

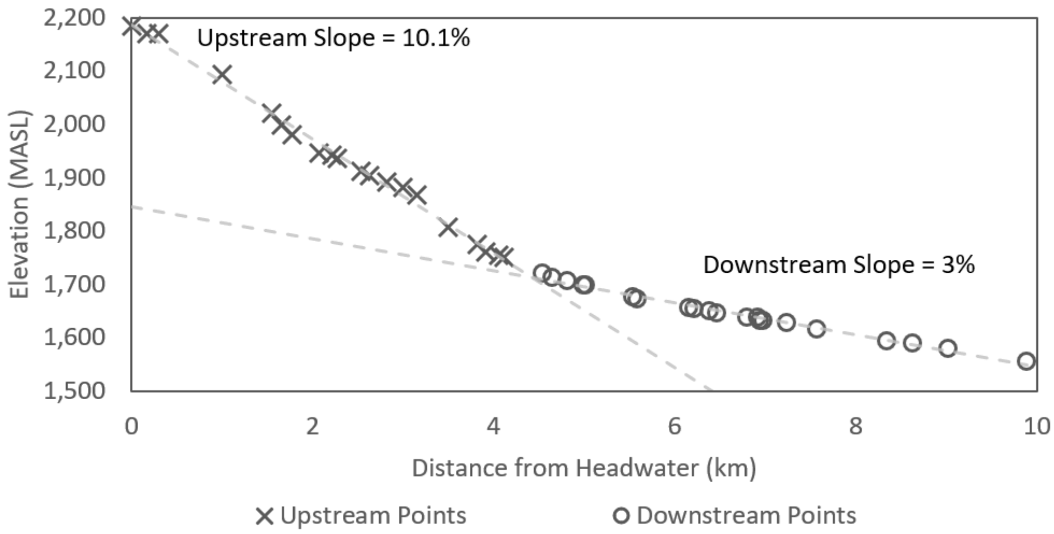

Figure 3-3: Average channel slopes in Chauncey Creek; elevations derived from DEM data from Natural Resources Canada (2016a)

Access to the Chauncey Creek was limited due to project limitations and early seasonal snowfall, so other sites were chosen for conducting tests to compare GSD measurement techniques. The Elk River near Elkford was selected for the Wolman pebble count comparisons, and a paint-and-pick comparison was performed at a site on the Mamquam River in Squamish, BC (Figure 3-4). These test counts were only done to test sampling methods, and the results were not used for modelling purposes.

The Wolman pebble count locations along the Elk River are in the same major watershed as Chauncey Creek, and similar geology and grain sorting were expected. The Elk River has greater flows than Chauncey Creek, but has a shallower slope and lower stream power so smaller particles were present. Located closer to the west coast of BC, the Mamquam River is not in the Rocky Mountains and would be expected to have different geology, but after inspecting the site, a similar grain sorting was found. The paint-and-pick site was selected for its ease of accessibility while being remote enough that UAV flying was permitted.

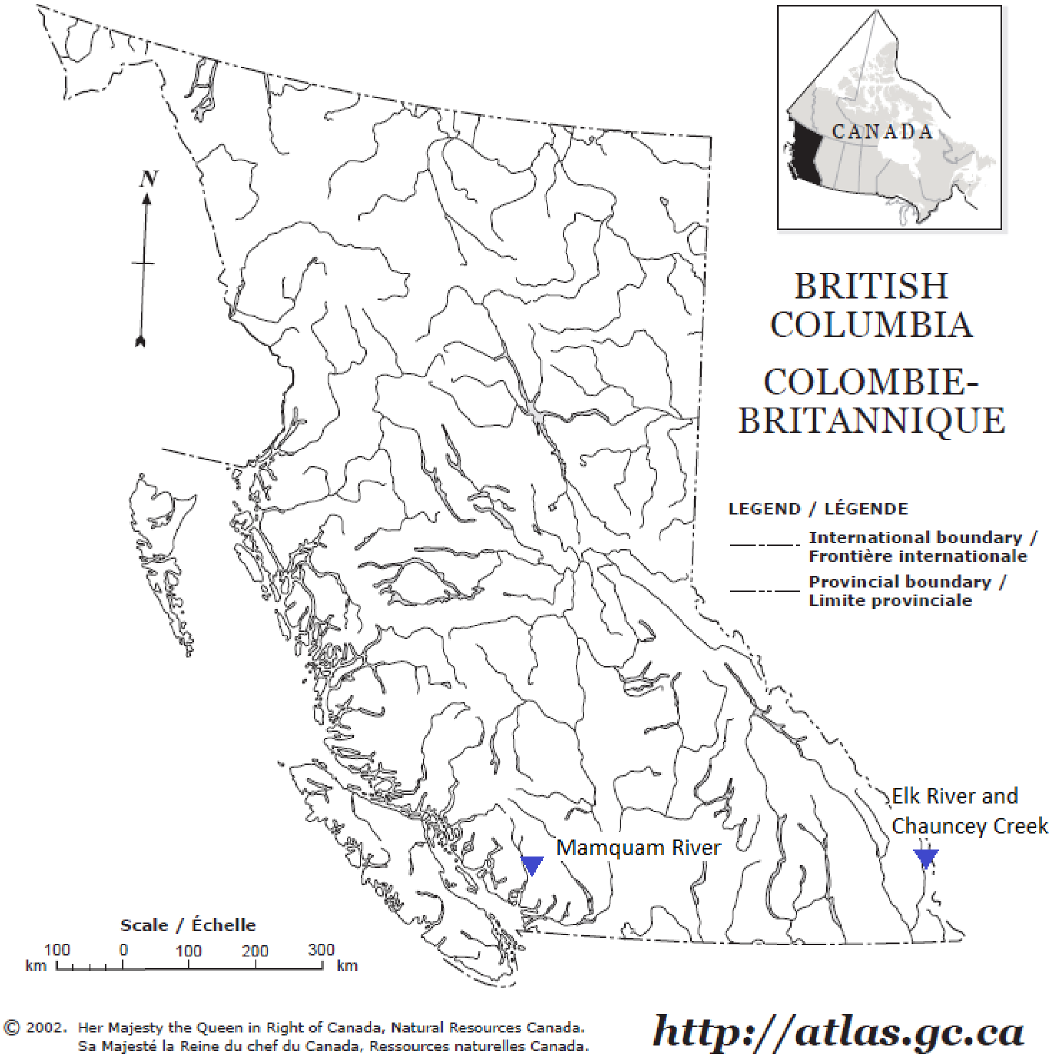

Figure 3-4: Field study locations in BC

3.1.3 Grain Size Distribution Measurements

Surface sampling was the focus of the field study. The surface layer is generally used to describe the surface roughness of an alluvial channel and only includes the particles that are exposed (Figure 2-1). Various measurement techniques can be used to sample the surface sediment and each one can be categorized under one of the following descriptions (Diplas & Sutherland, 1988):

- Grid sampling - Individual surface particles in the field are counted at grid indexes or along a traverse and sized by measuring the b-axis or using a gravelometer. Both "pebble counts" and "grid counts" from Bunte and Abt (2001) would fall within this category.
- Areal sampling - Surface particles within a square are sampled by photographing the selected region, using an adhesive to remove all the particles, or manually with the aid of spray paint to identify surface particles. Particle sizes are measured using a sieving or by counting individual particles.
- Line sampling - Every particle along a line is collected from the field and measured into size classes by sieving.

Following the naming convention from Bunte and Abt (2001), each sampling method can be categorized as a volumetric, grid, or areal sample. Within each of these sampling methods, the GSD can be analyzed "by-weight" or "by-count". The naming convention for each sampling method and analysis is a combination of these details (e.g. a volumetric sampling method that is analyzed by weight is described as volume-by-weight). Six different methods are possible when using these names. The three methods used in this study include:

- volume-by-weight (Also referred to as a bulk sieve analysis)
- grid-by-number (e.g. Wolman pebble counts)
- area-by-number (e.g. photosieving and paint-and-pick)

Wolman Count

Wolman pebble counts were completed following the methods described by Wolman (1954) and Leopold (1970) and later summarized by Bunte and Abt (2001). The traverses proceeded in grid-like patterns that covered a single geomorphological element (point bars and mid-channel bars), and spacing between counts of particles was 2 to 3 paces depending on the estimated maximum grain size and area of the gravel bar. Particles were selected after taking the regular number of steps and picking the one that was immediately below the large toe of the leading foot. At the same time, the researcher's gaze was adverted. The Wolman pebble counts did not include wading because they were done to compare to photosieving techniques, which were only used to measure dry, exposed sediment. With time permitting, 100 particles are counted and classified into half Ψ classes based on the length of the second largest dimension (b-axis) following the Wentworth scale (Table 3.1). Samples with 100 particles are considered standard Bunte and Abt (2001), but in locations where time was limited, a minimum of 50 particles were classified. A gravelometer (Figure 3-5) was used to measure Ψ class of particles for more consistent results and less operator bias. This device has precut holes that match half Ψ classes that a researcher can pass particles through to classify particles by size.

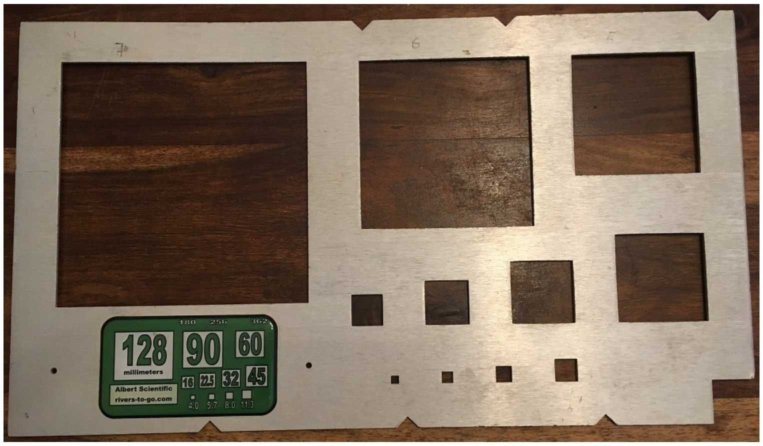

Figure 3-5: Gravelometer

Table 3.1: Sediment size classes (Wentworth scale)

Description of Particle Size	$\Psi = \log_2$	Maximum b-axis Length (mm)
Boulder	>8	>256
Large cobble	8	256
	7.5	181
Small cobble	7	128
	6.5	90.5
Very coarse gravel	6	64
	5.5	45.3
Coarse gravel	5	32
	4.5	22.6
Medium gravel	4	16
	3.5	11.3
Fine gravel and finer	3	8

Paint-and-Pick

The second method for collecting surface GSD measurements was to use a manual sampling technique (Bunte & Abt, 2001) with the aid of orange spray paint. This method is sometimes referred to as a "paint-and-pick" method. Similar to a Wolman pebble count, a paint-and-pick count involves classifying individual sediment particles by size. Instead of walking and measuring random particles, the goal is to count every particle within a manageable area without counting particles that were initially buried. The sample area size was selected using an estimated D_{50} and the following equation from Graham, Reid, and Rice (2005):

$$A_s = n_p D_{50}^2 \tag{3.1}$$

where A_s is the required sample area (mm^2), D_{50} is the median grain size (mm), and $n_p \geq 300$ is the number of particles. All particles with paint on them were measured using a gravelometer. Particles larger than the 8 mm hole were counted and recorded.

Photosieving

As an alternative to standard pebble counts, photos of surface particles can be analyzed with software to estimate the GSD. Photosieving is a technique where a photo is taken from a standard height and pebbles are measured directly from the image using a reference scale (Adams, 1979). BASEGRAIN is an example of computer software that can be used to automate the process of detecting and measuring individual particles (Detert & Weitbrecht, 2012). Photos to measure GSDs were taken with a hand-held iPhone SE and from higher elevations using a DJI Mavic 2 pro. The Mavic 2 Pro has a 20 megapixel 1" camera sensor with a 28 mm equivalent focal range, and the maximum flight time is approximately 30 minutes on a full charge. The iPhone SE has an 8 megapixel 1/3.0" camera sensor with a 29.7 mm equivalent focal range. Hand-held photos included a known scaling device within the frame of each image so that pixel resolution could be found directly from each photo.

Photo resolution limits photosieving, and camera specifications determine how high above the ground a photo can be taken to cover as much area as possible while still being able to detect small particles. Detert and Weitbrecht (2012) noted that grain areas smaller than 20 px are hard to detect and recommend a default detection limit of 23 px, citing results from Graham, Rice, and Reid (2005). This pixel size is a little misleading in that Graham, Rice, and Reid (2005) refer to a minimum b-axis detection length equal to 23 px while Detert and Weitbrecht (2012) refer to particle area. This difference means that the flight height could be set to nearly five times as high when following the advice of Detert and Weitbrecht (2012). It was decided that a particle diameter of 4.8 px (area of 23 px) would be considered the lower detection limit following the methods of Detert and Weitbrecht (2012) while recognizing that other studies have used particle detection lengths of as little as 3 px (Carbonneau et al., 2018). The allowable camera height was calculated using a ground sampling distance, the distance on the ground covered by each pixel, small enough to detect an 8 mm particle and the following relationship from O'Connor et al. (2017):

$$h = \frac{l \times f}{S_{det}} \tag{3.2}$$

where h is the camera height above ground (m), l is the ground sample distance (mm), S_{det} is the pixel width (μm), and f is the focal length (mm). Table 3.2 shows a comparison of camera details and grain size detection limits at various camera heights.

Table 3.2: Camera details

Specification	Units	iPhone SE	DJI Mavic 2 Pro	
Lens focal length (35 mm equiv.)	mm	29.7	28	
Pixel width	μm	1.5	2.4	
Height above ground	m	1.5	3	7
Ground sample distance	mm/px	0.42	0.46	1.12
Minimum grain size	mm	2.01	2.21	7.80
	Ψ	1	1.5	3

3.1.4 Photogrammetry Surveys

Photogrammetry is the process of combining 2D photographs taken from different locations and angles of the same subject to make 3D models. Within the field of photogrammetry, SfM is a technique which uses photos from a motion sequence. The two objectives for completing SfM surveys were to:

1. obtain photographs of exposed sediment that could be analyzed using photosieving software to find GSD properties; and
2. model 3D terrain of river geometry to characterize channel width, provide supporting visuals, and identify morphological elements.

The first objective is more complicated than simply taking off with a UAV and taking photos of the entire area because, for photosieving to work, the scale of each photo must be known. A ruler can be placed within the frame of each shot for hand-held cameras, but it is not practical to lay enough rulers on the ground to ensure each photo from an aerial survey includes one. Agisoft software made it possible to satisfy the second objective of creating a 3D terrain model using SfM algorithms while in turn supporting the first objective by providing camera heights for each photo using methods similar to those described as robotic photoseiving by Carbonneau et al. (2018). The camera heights can be used with a rearranged version of Equation 3.2 to find the GSD of each particle.

Ground control points (GCPs) were made to provide easily distinguishable points that could be identified in nearby photos. The markers were printed to also include a 40 cm scale and large reference number on 40 cm x 28 cm pieces of paper before being laminated (Figure 3-6). Due to a small amount of resizing during the printing process, the scales were measured to be 39.8 cm in length. The circular barcodes produced within Agisoft were chosen for the GCPs as they can be detected automatically in each photo. Carbonneau et al. (2018) showed that GCPs are not necessary for robotic photoseiving, but James et al. (2017) showed that strongly georeferenced GCPs (10 mm horizontal accuracy and 20 mm vertical accuracy) can improve surface precision by a factor of 3 when compared to surveys with weakly georeferenced GCPs (50 mm horizontal accuracy and 100 mm vertical accuracy). GCPs were placed throughout the survey areas, but they were not georeferenced at the time of the flight due to a lack of sufficiently accurate equipment.

Figure 3-6: Ground control point

SfM surveys can be taken using a range of different camera settings and flight paths depending on the required information and quality of the camera. The surveys were flown in grids to take enough photos of the river such that an entire geomorphological unit was photographed and that images have sufficient overlap with each other for software to detect common points and edges that are present in multiple neighbouring photos. Millimetre accuracy was required for individual photos, but the same accuracy was not required of the 3D model. Research shows that error within a SfM model can be reduced by taking nadir photos from multiple heights and as well as a series of pictures from oblique angles (Clapuyt et al., 2016; James & Robson, 2014; James et al., 2017; Carbonneau et al., 2018). Table 3.3 shows a list of flight paths flown by scientists conducting geomorphology studies which were used for reference.

Table 3.3: Reference flight paths

Researcher	Flight Height	Camera Angle	Camera/Resolution
Carbonneau et al. 2018	7 m	nadir	2 - 3 mm
	20 m	nadir	
	60 m	oblique (20° from nadir)	
Vázquez-Tarrío et al. 2017	30 m	nadir	5 Mpx GoPro
Neverman et al. 2019	3 m	nadir	1.5 mm
	3 m	oblique	

The flight plan chosen for Chauncey Creek included three passes over the selected survey areas. For all three passes, the UAV was manually flown following a grid-like pattern with a horizontal overlap of 50%. Preset flight paths would have been difficult for the survey locations because there was a high degree of variability in survey location shape and trees taller than 7 m presented obstacles for the UAV.

Photo quality can be reduced due to high contrast conditions, uneven colouration of particles from precipitation (Detert & Weitbrecht, 2013), and motion blur. Photos were taken during dry conditions and when there were no harsh shadows to minimize error. However, there were some instances when small amounts of precipitation fell, and there was not enough time to allow the sediment to dry completely. Motion blur was calculated using the following equation from O'Connor et al. (2017):

$$b_{blur} = \frac{v \times t_{ss}}{l} \tag{3.3}$$

where b_{blur} is the motion blur (px), v is the drone velocity (mm/s), and t_{ss} is the shutter speed (s). The speed of the drone was limited to 2 m/s and 3 m/s at 7 m and 20 m flight heights, respectively, with a shutter speed of 1/320 s which results in a 3.8 px blur at 7 m. Ideally, the shutter speed would have been 1/1600 s as recommended by Clapuyt et al. (2016) or at least slow enough such that the motion blur was less than 1.5 px as supported by O'Connor et al. (2017).

The drone camera set-up was also checked for whether or not it would be diffraction limited. A photo that is diffraction limited could result in reduced photo sharpness and can be identified using the following equation from O'Connor et al. (2017):

$$\frac{d_{dif}}{2} = 1.22\lambda \times N_{f-stop} \tag{3.4}$$

where d_{dif} is the diffraction limit (μm), λ is the wavelength of light (μm), and N_{f-stop} is f-stop of the aperture. This calculation suggests that the drone would be diffraction limited with an f-stop of 2.8, so some diffraction was unavoidable. O'Connor et al. (2017) suggests some diffraction is often acceptable; however, photos with aperture settings higher than f/4 were avoided to limit the amount of diffraction. The three passes flown at each survey location are summarized below:

1. The first pass was flown at a height of 7 m above the landing zone, and the camera was pointed straight down to take nadir photos. The UAV was flown with a speed of 2 m/s to ensure 25% forward overlap. These photos were used for both GSD measurements and SfM model creation.

2. The second pass was flown at the height of 20 m, and again, the camera was pointed straight down. This pass was flown at a faster speed (3 m/s) and wider spacing because the ground scale of the photos were larger than for the first pass.

3. The third pass was flown following the same grid and speed as the second pass but with the camera pointed 20° from nadir. The UAV was rotated 180° horizontally for each line of the grid in this pass so that half of the photos would be orientated in an opposing direction.

3.2 Field Data Processing

3.2.1 Single-Sample Grain Size Distribution Analysis and Conversions

There are many different methods for measuring the surface GSDs of laboratory flume studies and alluvial river beds in the field; not all of the standard techniques are directly comparable. This section describes three properties of each method that were considered when making comparisons, which include the:

- geometry of the sample;
- measurement size boundaries and Ψ bin size; and
- method of measuring diameter.

Sample Geometry: Voidless Cube Model

When comparing sampling methods, the geometry of the sample and the statistical likelihood of obtaining the same GSD from the same sediment deposit must be evaluated. The "voidless cube model" described by Kellerhals and Bray (1971) provides a geometrical relationship between the different sampling methods (Section 3.1.3) which led to a series of conversion factors that can be applied for comparisons. The general conversion factor is written as:

$$f_{ci} = f_{oi} D_{gi}^{x_e} \Bigg/ \left\{ \sum_{i=1}^{n_s} f_{oi} D_{gi}^{x_e} \right\} \tag{3.5}$$

where f_{oi} is the observed proportion of the sample in the ith size class with geometric mean size D_{gi}, x_e is the integer dimension required for the conversion (determined from Table 3.4), n_s is the number of grain size classes, and the sum effects a renormalization of the distribution to give the converted proportions f_{ci} (Church et al., 1987). It should be noted that grid-by-number is directly comparable to volume-by-weight, and no conversion factor is needed (Church et al., 1987; Diplas & Sutherland, 1988; Bunte & Abt, 2001; Wilcock & Crowe, 2003).

Table 3.4: Conversion factors for samples collected by various methods; from Kellerhals and Bray (1971) and edited by Bunte and Abt (2001). Numbers in gray bars express the conversion factor as the exponent of D.

	Conversion to				
Conversion from	Volume-by-weight	Grid-by-number	Grid-by-weight	Area-by-number	Area-by-weight
Volume-by-weight	1	1	D^3	$1/D^2$	D
	0	0	3	-2	1
Grid-by-number	1	1	D^3	$1/D^2$	D
	0	0	3	-2	1
Grid-by-weight	$1/D^3$	$1/D^3$	1	$1/D^5$	$1/D^2$
	-3	-3	0	-5	-2
Area-by-number	D^2	D^2	D^5	1	D^3
	2	2	5	0	3
Area-by-weight	$1/D$	$1/D$	D^2	$1/D^3$	1
	-1	-1	2	-3	0

A modified version of the voidless cube model (modified cube model) was developed by Diplas and Sutherland (1988) to account for bias not originally addressed by Kellerhals and Bray (1971) when converting from area-by-weight to grid-by-number or volume-by-weight methods. Bunte and Abt (2001) provide characteristics of sampling methods for whether the voidless cube model or modified cube model is more appropriate (Table 3.5). The sample locations for the Wolman pebble count comparisons are more closely aligned with characteristics matching the voidless cube model, so -1 was used as the exponent in this study. This method matches Strom et al. (2010), who also found that the exponent from the voidless cube model provided the best relationship comparing photosieving to Wolman pebble counts and grid samples.

Table 3.5: Approximate value of the conversion factor exponent required for converting the particle-size distribution of an area-by-weight sample into a volume-by-weight sample in deposits of different characteristics, based on results of several studies; from Bunte and Abt (2001).

Approximate value of the conversion factor exponent -1.0	 -0.5	 0
Determined from voidless cube model (Kellerhals and Bray 1971)	Determined from void-containing cube model (Diplas and Sutherland 1988)	
Coarse and fine matrix-supported gravel with high sand content	Frame-work supported gravel, esp. coarse gravel deposits	Fine frame-work gravels
Deposits of low porosity	Deposits of high porosity	
Coarse gravel deposits	Deposits of fine gravel and sand	
No depth penetration of adhesive e.g., adhesive tape	Deep penetration of adhesive into subsurface sediment	
Poorly sorted gravel deposits	Well-sorted gravel deposits	Very-well sorted gravels
Photo-sieving		

Data Truncation and Bin Sizes

Each GSD measurement has a minimum particle size that can be representatively measured depending on the method used. For example, a volumetric sieve analysis using a minimum square-hole size of 4 mm would only represent the 2 mm to 4 mm grain size adequately if it is already known that no particles smaller than 2 mm are present in the sample.

For the comparison of samples, Church et al. (1987) recommends using a common sample range. Traditional pebble counts such as the Wolman pebble count were found to under-represent particles smaller than 8 mm in diameter (S. Rice, 1995), and photosieving is dependent on the camera resolution and height from which photos are taken (Graham, Rice, & Reid, 2005; Detert & Weitbrecht, 2013). These types of measurement errors can lead to a skewed GSD that is often most noticeable in small size classes unless there is a significant proportion of sand (Graham et al., 2010). 8 mm was found to be a suitable lower boundary for photosieving counts using UAV imagery from 7 m above the ground (Table 3.2). For that reason, and on recommendations for Wolman pebble counts by S. Rice (1995), all GSD measurements were truncated below 8 mm. Equal bin sizes should also be used (Wolman, 1954), so half Ψ classes were used for all GSD measurements.

Diameter Measurement and Square-Hole Approximation

All the previously described GSD sampling methods use one of two measurements for classifying a particle by size. A particle's size class is determined by either measuring the b-axis or sieving the particle through a series of square-holes. For methods to be adequately compared, a conversion factor must be applied (Church et al., 1987). Stähly et al. (2017) recommends a factor 0.86 or a linear fit from 0.78 to 0.95 when comparing physically measured particle b-axis to square-hole sieve analyses. However, the b-axis measured from photosieving methods such as BASEGRAIN (now referred to as b'-axis) is underestimated because of partial burial, overlapping, and the angling of particles (Graham et al., 2010; Stähly et al., 2017). Ultimately, Stähly et al. (2017) found that a correction factor is unnecessary when comparing the b'-axis to square-hole measurements because the introduced errors tend to counteract each other.

3.2.2 Grain Size Distribution Comparisons

The basis for the Wilcock and Crowe (2003) model is a grid-by-number count using square-hole sieves to measure particle sizes, so all sampling methods were adjusted to be equivalent to grid-by-number methods before being compared. Table 3.6 shows the collected GSD sampling measurements and how they have been converted for comparison and to define Chauncey Creek surface sediment characteristics. All methods have been truncated to a minimum size class with a lower bound of 8 mm (Ψ 3.5 class).

Table 3.6: Sediment size measurement methods and conversions

Location	Method	Standard Name	Measurement	K-B Exponent
Chauncey Creek	Photosieving	area-by-number	b'-axis	2
Elk River	Wolman Count	grid-by-number	Square hole	0
	Photosieving	area-by-number	b'-axis	2
Mamquam River	Paint-and-Pick	area-by-number	Square hole	2
	Photosieving	area-by-number	b'-axis	2

The geometric mean and grain size percentiles represent variables used for calculating sediment transport rates and were selected for comparison of samples. The geometric mean was calculated using an frequency distribution approach adapted from Bunte and Abt (2001) and is equivalent to the arithmetic mean of the distribution when reported in Ψ-units:

$$D_{gm} = 2^{\Psi_m} \tag{3.6}$$

$$\Psi_m = \frac{1}{100}\sum_{i=1}^{k}(\Psi_{ci} \cdot m_{\%i}) \tag{3.7}$$

where D_{gm} is the geometric mean of a GSD in mm, Ψ_m is the arithmetic mean of Ψ measurements from a GSD, Ψ_{ci} is the centre of the i^{th} size class (Ψ), and $m_{\%i}$ is the percentage frequency by weight for particles retained in the i^{th} size class. Percentiles were calculated by interpolating the logarithmic dataset (Bunte & Abt, 2001):

$$\Psi_x = (x_2 - x_1) \cdot \left(\frac{y_x - y_1}{y_2 - y_1}\right) + x_1 \tag{3.8}$$

where Ψ_x is the x^{th} percentile of a particle-size distribution (Ψ), y_1 and y_2 are the two values of cumulative percent frequency immediately less than and greater than the desire cumulative frequency y_x, and x_1 and x_2 are the particles in Ψ-units associated with the frequencies y_1 and y_2.

3.2.3 Defining River Geometry

The longitudinal profile of the main stem in Chauncey Creek was characterized using the elevation and slopes from the Canadian Digital Elevation Model (CDEM) and National Hydrographic Network (NHN) (Natural Resources Canada, 2015, 2016a) using FAST. Sediment links were identified by analyzing the curvature in slope trends and locating point sources of water and sediment from aerial photos. Slope was also measured directly from UAV derived DEMs by using the channel elevation at the upstream and downstream boundaries of each survey location and measuring the channel length.

Spatial data comes in a variety of resolutions depending on the method of data collection (Vetsch et al., 2018). The CDEM has a vertical resolution of 1 m and horizontal resolution between 20 and 25 m whereas the UAV derived DEMs have 1 cm vertical resolution and between 2 and 3 cm horizontal resolution. Ideally, the higher resolution DEM would be used. However, the issue with the UAV derived DEMs is that they only cover reach lengths ranging from 30 to 70 m. Channel slope can vary over short distance due to the presence of different morphological elements such as riffles and pools, so averaging slope over a long distance relative to the meander spacing is recommended (Harrelson et al., 1994). Because of this, channel slope is defined using the CDEM derived slope averaged over distances of 500 m, and slopes from UAV derived DEMs were compared.

Channel width, for the purpose of this study, was defined as the distance from bank-to-bank where the banks are located at "the elevation at which the width/depth ratio (W/D) of the cross-section becomes as minimum" similar to one method for calculating bank-full conditions described by G. P. Williams (1978). River geometry is highly variable and hard to define from DEMs in mountain channels because of insufficient resolution. It is possible to extract channel widths from aerial photos, but this can be difficult due to vegetation obscuring views of the banks and the banks may not be well defined.

The UAV SfM models were exported as DEMs and had a much higher resolution ($<$ 2 cm) than regional datasets. GIS software was used to delineate a cross-section from the DEM and measure river bathymetry. Bathymetry under the flowing water would not be representative of the actual river bed because photos are not able to penetrate the water surface evenly. However, the active channel width calculation is only dependent on the geometry of the exposed banks during low flows and, therefore, was not affected by the bathymetry under the water. An Excel subroutine was used to find the banks that result in the lowest width-to-depth ratio at individual cross-sections (Figure 3-7).

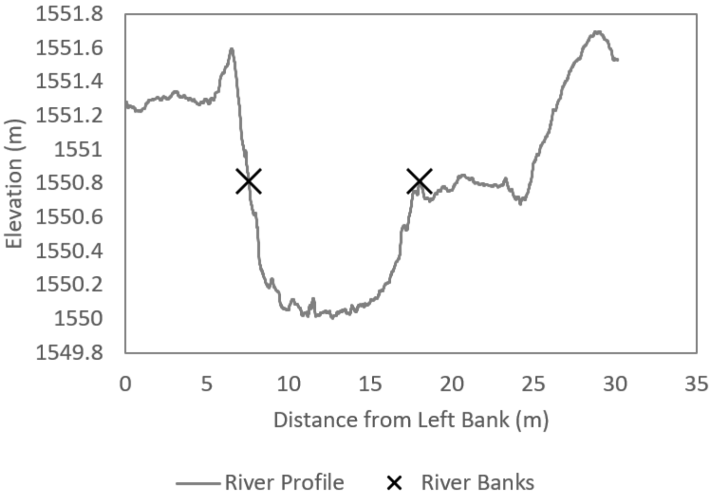

Figure 3-7: Example of bank identification for channel width measurements

Mountain stream widths have been found to follow a power-law relationship relative to catchment area (Julien, 2015; Sofia et al., 2015):

$$w_{ac} = aA_C^b \tag{3.9}$$

where w_{ac} is the active channel width, A_C is the catchment area (km^2), and a and b are empirically derived constants. A power function was developed for Chauncey Creek using multiple measured cross sections from each survey location to define the channel width for the full modelled extents.

3.2.4 Defining Surficial Grain Size Distributions

Modelling a river catchment would be infeasible if GSD measurements were required in every reach, so a relationship that could be used to describe the GSD throughout the entire catchment was characterized using a series of individual measurements. Photosieving with BASEGRAIN was used to define the surficial GSDs at each survey location. The work flow used in BASEGRAIN is shown in Appendix C. The area-by-number distributions measured by photosieving were converted to volume-by-weight distributions using Equation 3.5 and an exponent $x_e = 2$ (Table 3.4) to match measurements used by Wilcock and Crowe (2003). Multiple aerial samples in a single survey location were considered to be part of the same population, and particle counts were added together to produce a single GSD for the reach. The surficial GSD varies across morphological elements within an individual survey location, so similar morphological elements were chosen in each survey location. Figure 3-8 shows how GSDs at a single survey location can vary depending on where in a morphological element the measurements are taken, and Figure 3-9 shows where the measurements were taken in relation to the active channel for the measurements in Figure 3-8.

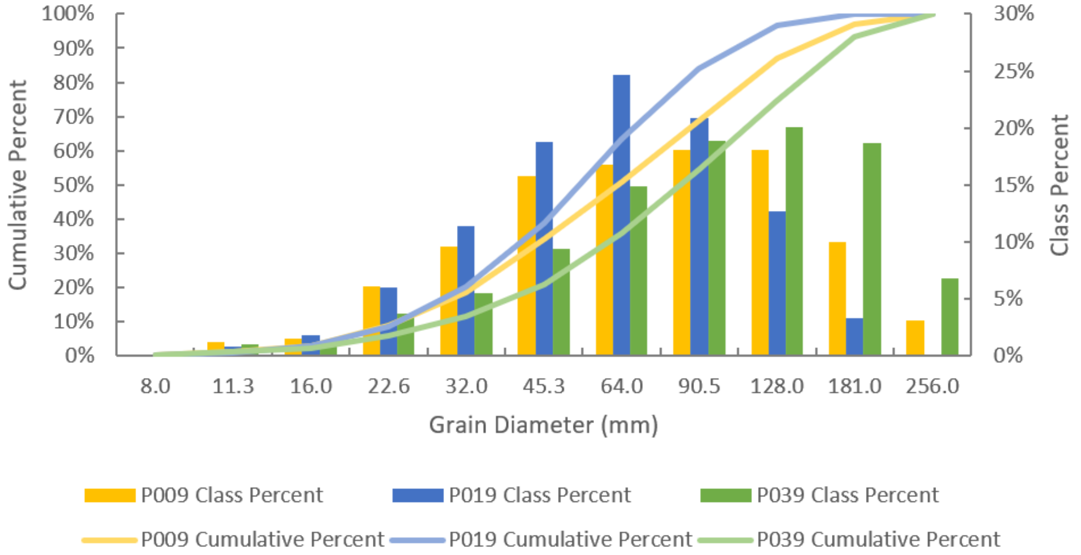

Figure 3-8: Example of different grain size distributions measured at the same survey location

Before a relationship for the catchment could be characterized, the shape of the measured distributions had to be determined. The GSD at each location was checked for

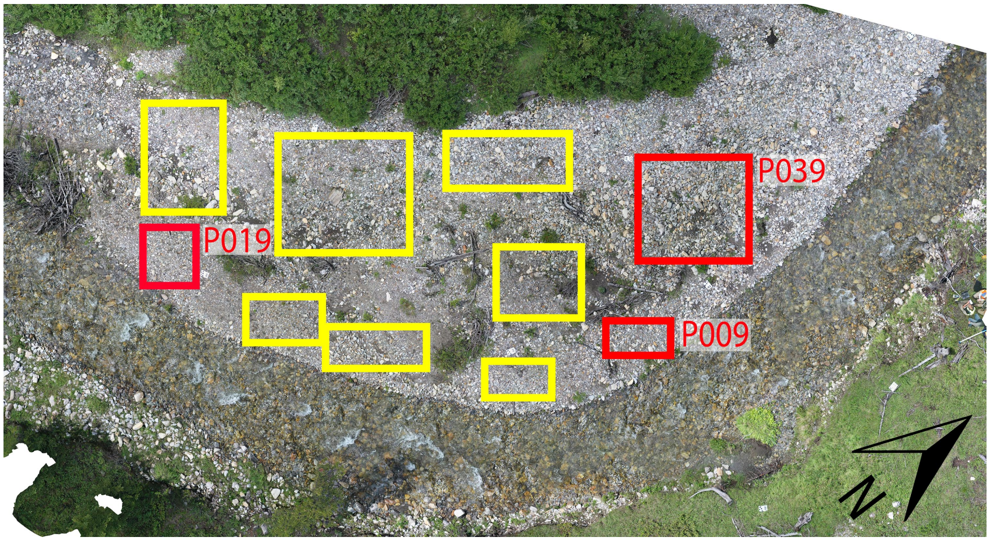

Figure 3-9: Example of BASEGRAIN measurement locations at a single survey location. Red rectangles indicate measurements that are shown in Figure 3-8 and yellow rectangles indicate additional measurements that were made along the point bar. The creek is flowing southwest.

normality by evaluating the goodness-of-fit to the best-fit Gaussian distribution and best-fit Rosin distribution following the methods described by Bunte and Abt (2001) and incorporating the suggestions from Schleyer (1987). The best-fit Gaussian distribution was calculated using:

$$G_{\Psi_i} = \frac{1}{\sigma \cdot \sqrt{2\pi}} \cdot \exp\left(-\frac{(\Psi_i - \mu)^2)}{2\sigma^2}\right) \tag{3.10}$$

where G_{Ψ_i} is the frequency of a Gaussian distribution for the ith size class, Ψ_i is the particle size of the ith size class in Ψ units, μ is taken as the distribution median, and σ is the standard deviation. σ in Equation 3.10 is substituted for a sorting coefficient (s_G) as suggested by Schleyer (1987):

$$s_G = 0.75(\Psi_{75} - \Psi_{25}) \tag{3.11}$$

The best-fit Rosin distribution was calculated using:

$$R_{Di} = \exp - \left(\frac{D_{ret,i}}{D_{mode}}\right)^{S_R} - \exp - \left(\frac{D_{pass,i}}{D_{mode}}\right)^{S_R} \tag{3.12}$$

where R_{Di} is the frequency of a Rosin distribution for the ith size class, $D_{pass,i}$ is the passing sieve size for the ith size class (mm), $D_{ret,i}$ is the retaining sieve size for the ith size class (mm), and s_R is a sorting coefficient:

$$s_R = \frac{2.15}{\Psi_{18.4} - \Psi_{68.4}} \tag{3.13}$$

A distribution was considered normal if it had a goodness-of-fit relative to the Gaussian distribution greater than 95% and a better fit when compared to a Rosin distribution. The goodness-of-fit were calculated for the Gaussian and Rosin distributions using the following equations:

$$\%Gaussfit = 100\% - \frac{1}{n_s - 1}\left|(\sum m_{\%i} - \sum G_{\%i})\right| \tag{3.14}$$

$$\%Rosinfit = 100\% - \frac{1}{n_s - 1}\left|(\sum m_{\%i} - \sum R_{\%i})\right| \tag{3.15}$$

where $\sum m_{\%i}$ is the cumulative percent frequency for the ith size class, $\sum G_{\%i}$ is the cumulative percent frequency for the ideal Gaussian distribution, and $\sum R_{\%i}$ is the cumulative percent frequency for the ideal Rosin distribution. If the GSD was found to be normal, then the sorting (s), skewness (s_k), and kurtosis (k_u) were evaluated using methods by Folk and Ward (1957) as summarized by Bunte and Abt (2001):

$$s = \frac{\Psi_{84} - \Psi_{16}}{4} + \frac{\Psi_{95} - \Psi_{5}}{6.6} \tag{3.16}$$

$$s_k = \frac{\Psi_{50} - \Psi_{5}}{\Psi_{95} - \Psi_{5}} - \frac{\Psi_{84} - \Psi_{50}}{\Psi_{84} - \Psi_{16}} \tag{3.17}$$

$$k_u = \frac{\Psi_{95} - \Psi_{5}}{2.44 \cdot \Psi_{75} - \Psi_{25}} \tag{3.18}$$

The results of this method for calculating the sorting and skewness coefficients can be compared to the classification systems described by Folk and Ward (1957) to label the distribution as “poorly sorted” or “positively skewed”.

After finding the appropriate distribution, relationships defining the GSD for the length of Chauncey Creek were derived from distribution properties (μ, σ) at individual locations relative to an index of stream power. The stream power index (ω') was calculated using catchment area in lieu of flow because the precise relationship between bankfull flow and catchment area was not known, but a linear relationship was assumed. The resulting equation for stream power index does not include gravity or density terms and is as follows:

$$\omega' = A_C S / w \tag{3.19}$$

3.3 Field Results

3.3.1 Sampling Method Comparisons

The Wolman count comparison was completed at four locations along the Elk River (Table 3.7). Sites Elk 2-1, 2-2, and 2-3 were located on point bars along the same meander, and site Elk 1 was located approximately 3 km downstream of Elk 2-1. Figure 3-10 shows an example photo of what was used as an input to BASEGRAIN, and Figure 3-11 shows the results of the segmentation process for the same photo. Figure 3-12 shows the graphical comparison of measurements at all four sites, and Table 3.8 shows the percent difference in GSD percentiles measured at each site. The GSD percentiles from Wolman count and photosieving measurements were generally very close with differences in Ψ_{30} measurements $\leq 8\%$ and differences in Ψ_{90} measurements $\leq 3\%$ Ψ. Photosieving results were smaller than Wolman count measurements for percentiles less than D_{60}, and the difference was greater for smaller percentiles. Visual inspection of the BASEGRAIN result photos showed that particles were more often over-segmented than under-segmented. Over-segmentation is the case in automatic photosieving where a single particle is defined as multiple smaller particles, and under-segmentation is the case where multiple particles are defined as a single large particle.

The paint-and-pick comparison was completed on a 0.7 m x 0.7 m (0.49 m^2) area of sediment on the Mamquam River (Figure 3-13). Using Equation 3.1, that area is sufficiently large to count 300 particles as long as the D_{50} is less than 40 mm. Photos were

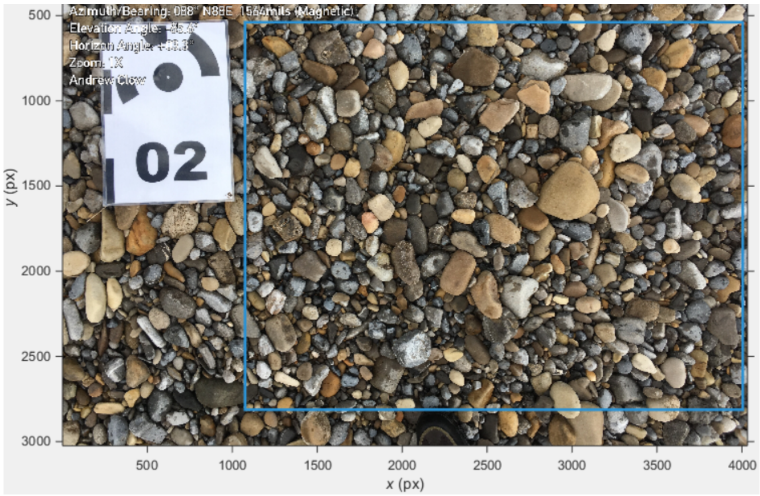

Figure 3-10: Example of a photo used to measure surficial GSDs for the Wolman pebble count comparison at Elk 1

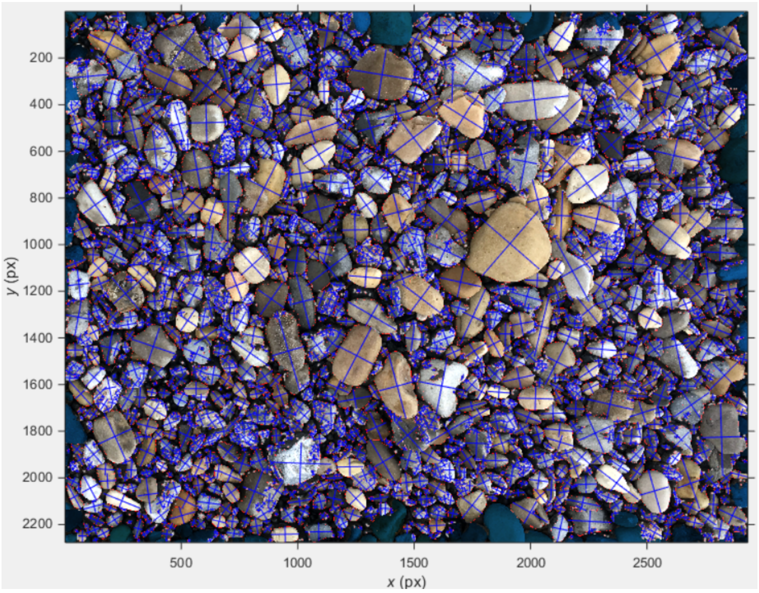

Figure 3-11: The result of particle segmentation in BASEGRAIN for the photo in Figure 3-10

Table 3.7: Location details for the Wolman count comparisons

Location	Pebbles Counted	Photos Analyzed	Geomorphological Element
Elk 1	100	4	Central bar
Elk 2-1	53	3	Leeward side of point bar
Elk 2-2	50	2	Central area of point bar
Elk 2-3	101	8	Upwind side of point bar

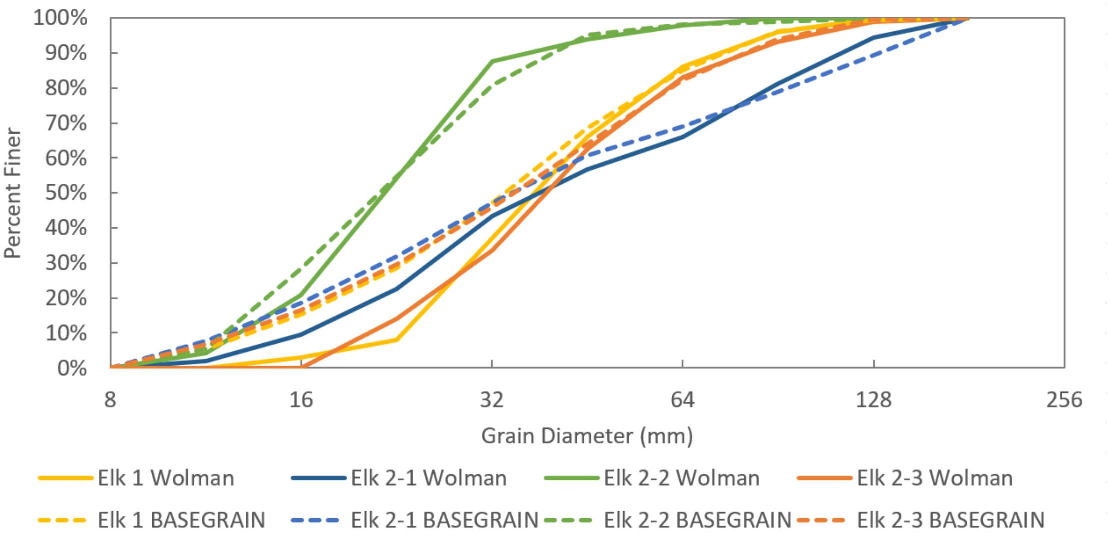

Figure 3-12: Comparison of BASEGRAIN counts to Wolman counts on the Elk River

Table 3.8: Wolman count comparison

	% Difference (Ψ)			
Selected Particle Sizes (D_x)	Elk 1	Elk 2-1	Elk 2-2	Elk 2-3
30%	-7%	-5%	-3%	-8%
50%	-3%	-3%	-1%	-3%
90%	0%	3%	2%	0%
Geometric Mean	-5%	-3%	0%	-5%

taken of the paint-and-pick region before an orange spray paint was applied to be used for photosieving. iPhone photos were taken from roughly 1.5 m above the ground, and UAV photos were taken from heights of 2 m and 5 m. The image taken from a lower height was expected to be more accurate because it had a finer resolution (0.3187 mm/px and 0.7931 mm/px at 2 m and 5 m heights, respectively). However, it was found that the difference between measurements was less than 0.5% (mm), so only one set of results is shown for the UAV. Figure 3-14 shows the results from paint-and-pick measurements compared to the photosieving measurements. The paint-and-pick results were between 3% and 7% (Ψ) smaller than the photosieving measurements for all percentiles (Table 3.9).

Figure 3-13: Photo of paint-and-pick sample area used for photosieving analysis

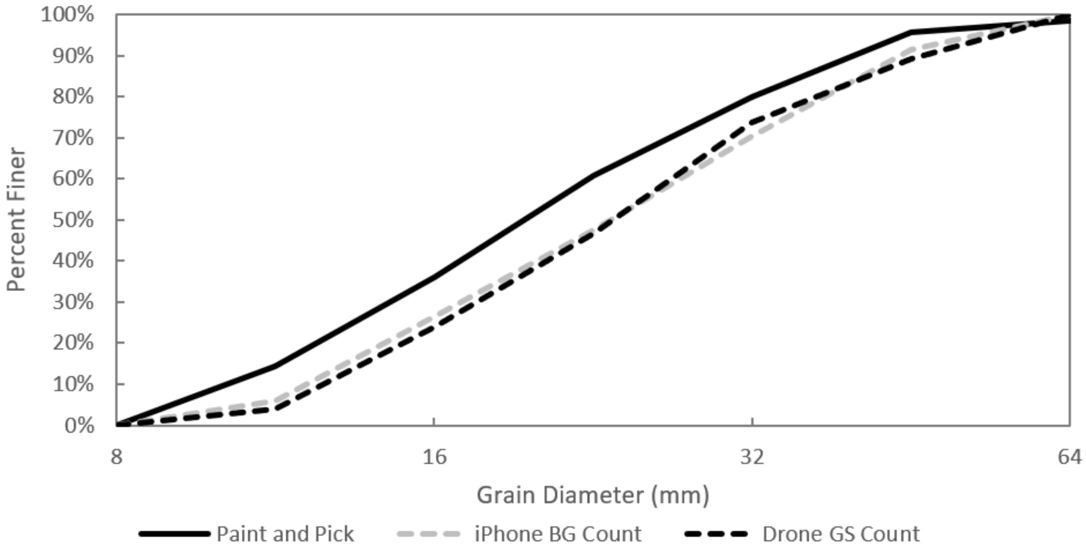

Figure 3-14: Comparison of BASEGRAIN counts to paint-and-pick count

Table 3.9: Paint-and-pick comparison

	Measured Percentiles (Ψ)			% Difference (Ψ)	
Selected Particle Sizes (D_x)	Paint-and-Pick	UAV	iPhone	UAV	iPhone
30%	3.86	4.13	4.08	7%	6%
50%	4.28	4.55	4.55	6%	6%
90%	5.32	5.51	5.52	4%	3%
Geometric Mean	4.32	4.56	4.54	5%	5%

3.3.2 River Characteristics

Analyzing the longitudinal profile of Chauncey Creek showed that there was a large variability in slopes measured from the CDEM along the channel, but reach slopes were more consistent downstream of the major confluence (Figure 3-15). Residuals were calculated relative to linear slope trends separated into two sections: upstream of the major confluence, and downstream of the major confluence. The trend in residuals can help identify locations of concavity and convexity. Reaches with slopes that are lower than the average channel slope can be identified by observing a positive trend in the calculated residuals. The peaks in residuals were areas where the slope becomes higher than the average slope and were determined to be the tops of sediment links. The locations of sediment link boundaries, point sources of significant sediment loading, correspond well with the residuals. Three sediment links were identified and are shown in Figure 3-15. A moving average showed that there were two sections with relatively steep slopes at 1 km and 3 km down from the headwater (Figure 3-16). The slopes measured from the UAV derived DEMs ranged from 3% to 6% and showed a decreasing trend similar to that of the slopes measured from the CDEM.

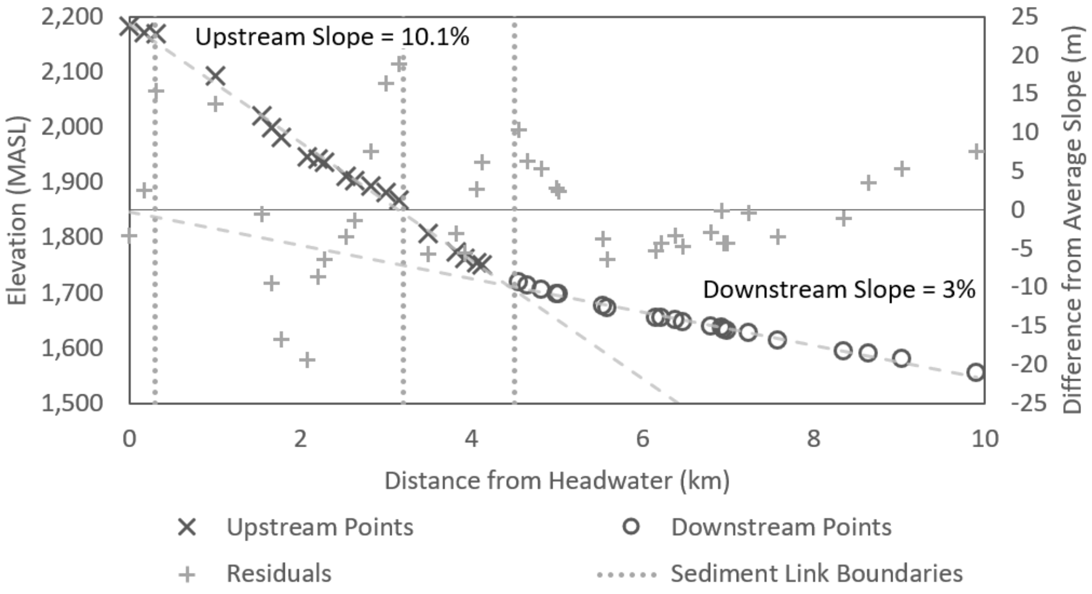

Figure 3-15: Chauncey Creek longitudinal elevations and residuals relative to average slope

The channel width was characterized by a power function relative to the catchment area. The data set of width measurements included eight individual cross-sections. The DEMs of the survey locations and locations of the cross-sections are shown in Appendix A. Width measurements were not used from SL07 because of the proximity of trees and vegetation on both banks which cause uneven bank measurements from the DEM, and SL06 was no longer flowing at average flows. Survey location SL03 included three measurements:

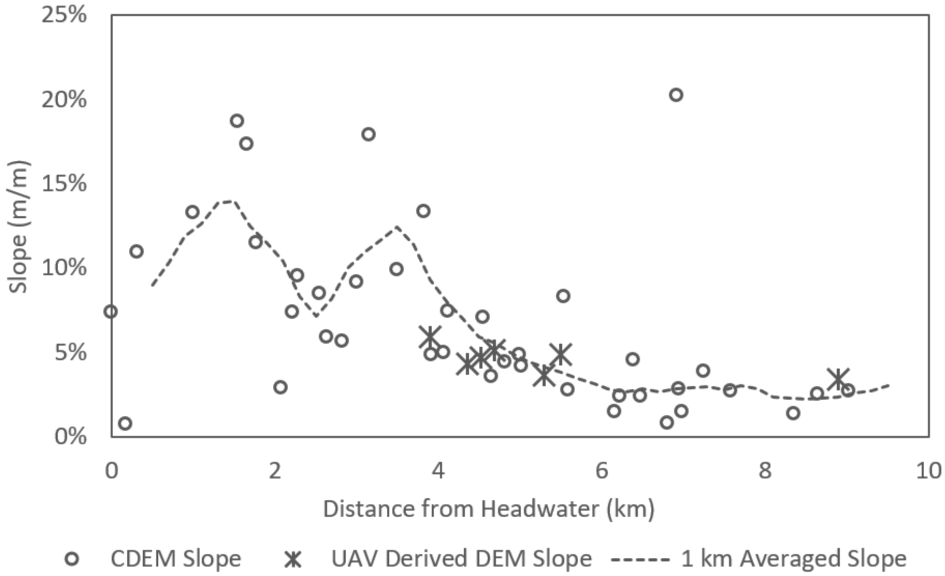

Figure 3-16: Average channel slope in Chauncey Creek

one on the main stem upstream of the confluence, one on the side tributary upstream of the confluence, and one on the main stem downstream of the confluence. Measurements were located upstream of bends where point bars were surveyed and cross sections were chosen to pass through areas with limited vegetation where possible. Figure 3-17 shows the relationship of channel width relative to the catchment area and the power function used to describe Chauncey Creek for modelling purposes.

GSDs were characterized at seven different survey locations. Between three and ten photos were analyzed at each site, but only results from similar morphological elements were chosen for characterizing the Chauncey Creek basin. The selected images were typically at the upstream end of point bars for survey locations at prominent meanders. Aerial photos indicating the locations of GSDs measurements are shown in Appendix B. Some survey locations had intricate flow patterns with woody debris and large living trees, but areas immediately downstream vegetation were avoided where possible. For sites where multiple photos were used, particle counts were added together with the assumption that photos were taken of the same sample population. GSDs at each survey location for checked

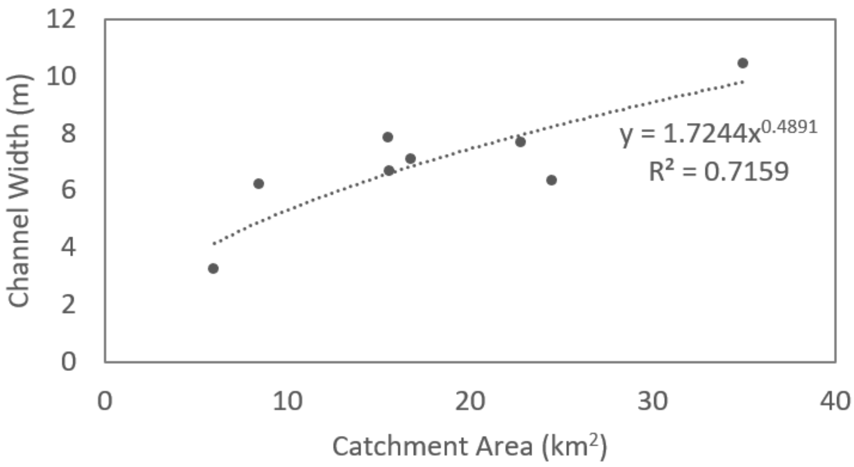

Figure 3-17: Channel width measurements in Chauncey Creek relative to catchment area

for goodness-of-fit relative to Gaussian and Rosin distributions and Gaussian distribution statistics were calculated. Table 3.10 shows the GSD statistics for each survey location. The GSD at each survey location was found to be well represented by a Gaussian distribution. The distributions were found to be poorly sorted ($1 < \text{s} < 2$) and nearly symmetrical or positively skewed ($-0.1 < s_k < 0.3$).

The GSD at each survey location was plotted relative to channel slope (Figure 3-18) and an index of stream power (Figure 3-19). The correlation between the D_{90} and the stream power index was the most significant trend observed and showed a positive trend. There was a slight positive trend observed for the D_{gm}, and the D_{30} remained relatively constant.

Table 3.10: Chauncey Creek grain size distribution statistics

Survey Location	D_{gm}	D_{90}	% Gaussian Fit	% Rosin Fit	Sorting	Skewness	Kurtosis
SL01	75.0	217.9	96.1%	84.8%	1.2	0.09	1.6
SL02	73.5	167.7	95.7%	87.7%	1.0	0.17	1.7
SL03	58.7	169.6	95.5%	85.5%	1.2	-0.05	1.5
SL04	71.8	222.7	96.2%	93.3%	1.3	0.11	1.5
SL05	74.3	261.9	96.1%	91.0%	1.4	0.03	1.4
SL07	86.5	324.4	95.9%	83.3%	1.5	0.03	1.4
SL08	81.5	316.1	96.6%	85.8%	1.4	-0.03	1.5

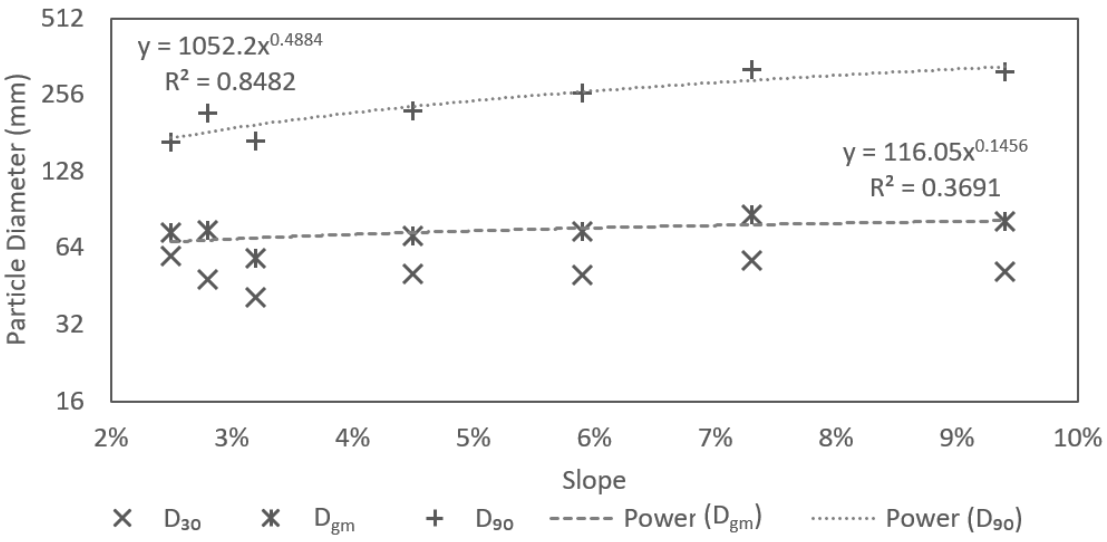

Figure 3-18: Chauncey Creek surficial grain sizes relative to channel slope

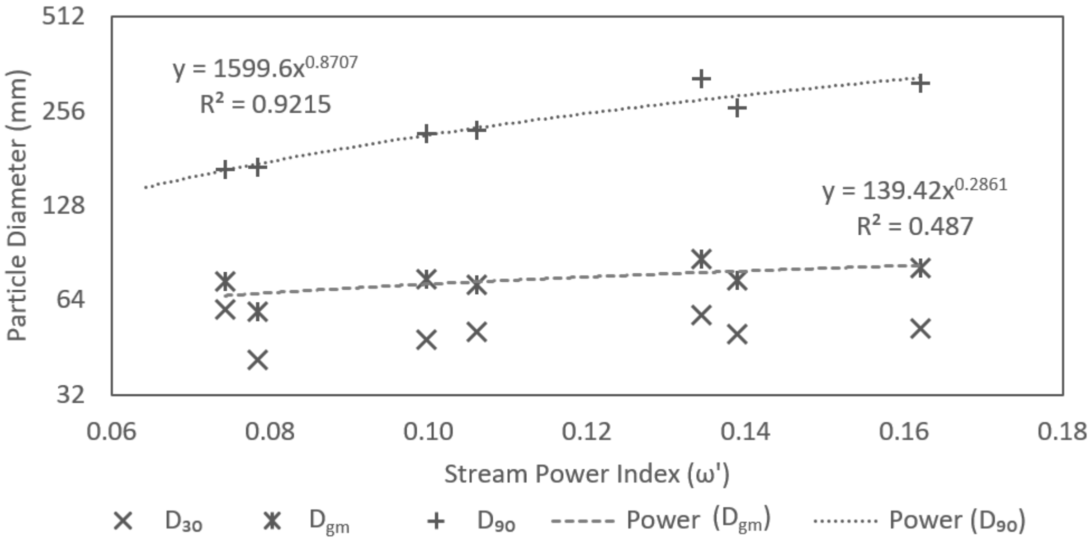

Figure 3-19: Chauncey Creek surficial grain sizes relative to an index of stream power ($\omega' = A_C S/w$)

3.4 Field Discussion

3.4.1 Sampling Method Comparisons

Comparing the GSD measurements from photosieving and Wolman counts presented only minor differences between the two measurement techniques, with the Wolman count measurements being slightly larger. Over-segmentation in the photosieving process leads to a finer GSD and could be one reason for the photosieving measurements being smaller than the Wolman count measurements. BASEGRAIN did not perform as well for larger GSDs and over-segmentation of large gravels and cobbles was common. Photo quality was less than ideal in some locations because of damp sediment conditions and the irregular appearance of some large particles. Manual adjustments were made with a focus on the larger particles and could explain why a smaller difference was measured for larger percentiles.

The paint-and-pick comparison showed that the photosieving measurements were consistently coarser than the paint-and-pick GSD by 0.23 Ψ on average. This difference could be accounted for with the use of an alternate conversion factor. The paint-and-pick diameters were measured using square holes, which should be comparable to photosieving the b'-axis measured with photosieving (Stähly et al., 2017). Stähly et al. (2017) applied two conversion factors that cancel out: one to convert from square-hole measurements to b-axis measurements and a second one to convert b-axis to b'-axis measurements. However, the conversion factors were found to vary based on particle size and sphericity, ratio of b-axis to the c-axis (shortest axis). Sediment that is completely spherical would have the same measured b-axis using either a square-hole approach or ruler, while a completely flat particle could have as much as a 40% difference between the two measurement methods (Church et al., 1987). The measurements may need to be converted for these methods to be directly comparable at the site. If b'-axes are multiplied by 0.85, then the Ψ measurements would change by - 0.235. This change would narrow that difference between the photosieving and paint-and-pick measurements to less than or equal to 1% (Ψ). It is less likely that over- or under-segmentation is the cause of the difference between photosieving and paint-and-pick measurements because very similar GSDs were measured from 3 separate photos.

3.4.2 River Characteristics

Sediment links (S. P. Rice & Church, 2001) are characterized by sediment inputs, including alluvial fans, and can be identified by trends in slope. Three sediment links were identified where the residuals peaked. The first link starts near the upstream boundary and extends for approximately 3 km. The second sediment link is the result of large alluvial fans that cover a roughly 1 km of the channel and continues until the confluence of the first large tributary. The third sediment link starts from the confluence of the first major tributary and extends to the downstream boundary. The upper two sediment links cause a more distinct change in slope than the third sediment link (Figures 3-15 and 3-16). Sediment links typically correspond to regions with a downstream fining trend. The measured GSDs show that the most recognizable downstream fining is at the upstream region in the third sediment link. The coarser D_{90} found near the downstream boundary could indicate that the third sediment link should be split up into multiple links, but more measurements would need to be taken to support the finding.

Channel width in stable, gravel-bed rivers has been described by many researchers with an equation of the form $w = aQ^b$ where a ranges from 2.85 to 5.876 and b ranges from 0.42 to 0.743 with most settling around 0.5 (Gholami et al., 2017). The channel widths measured using UAV derived DEMs resulted in a basin-wide relationship $w = 1.72A_C^{0.489}$. The exponent of the measured relationship is within the expected range when a discharge is assumed to be linearly related to area as has been found for small catchments in humid regions (Vianello & D'Agostino, 2007).

Statistics for the GSD at each survey location showed that a Gaussian fit best represents the distribution, and the skewness and kurtosis are relatively constant throughout the catchment. The sorting coefficients were found to have a positive relationship relative to slope and stream power. Most fluvially transported sediment in gravel-bed rivers match a Gaussian distribution, so this result indicates that the survey locations were downstream of hillslope sediment loads (Bunte & Abt, 2001). The skewness was found to be nearly symmetrical or skewed toward the fine side when using the classification of skewness from Folk and Ward (1957), which is also typical for gravel-bed rivers (Bunte & Abt, 2001). The sorting was found to range from 1.0 to 1.5 and can be described as poorly sorted (Folk

& Ward, 1957). The kurtosis was found to range from 1.4 to 1.7, but it is not often used as a descriptor of sediment distributions. Kurtosis could, however, be used to compare synthetic grain size distributions used for modelling purposes to what is found in the field.

The GSDs were compared to channel slope and stream power. Weak trends were found for the D_{30} and D_{gm}, and a strong trend was found for the D_{90} relative to both channel slope and stream power. The trend in coarse grain sizes is beneficial for modelling flow properties as they are strongly related to roughness, which allows for a relatively accurate assessment of resistance to flow, flow depth, and shear stress at different discharges. The functions relating D_{90} to slope and stream power have exponents of 0.5 and 0.87, respectively. The result for stream power matches functions relating surface particle diameters to dimensionless stream power. C. Parker et al. (2011) proposed a relationship where $\omega_c^* \propto \frac{1}{D_i^{3/2}}$ which equates to $D_i \propto \omega_c^{*2/3}$. Therefore, downstream fining could be considered the result of limited mobility of the coarsest sizes of sediment, which suggests that it is important to distinguish the sediment links and identify the size distributions at the upstream limit of each link. Downstream it appears that the decrease in the large particle size can be strongly related to the stream power so fewer measurements would be required.

Chapter 4

Sediment Transport Model

4.1 Model Specifications

To meet the objectives of this thesis, a new model (Alluvial Stability Indexing Model (ASIM)) was developed to assess the relative stability of river reaches throughout a catchment and how changes to a river network, such as installing a culvert or bridge, would affect geomorphological processes. A 1-D model was chosen to reduce the resolution requirements for spatial data, and a decoupled, fractional sediment transport process conceptual model was chosen to predict sorting trends of varying grain sizes. ASIM was built on the research from important contributions to sediment transport modelling over the last 20 years. These include the model developed by Cui et al. (1996) and G. Parker (2004), who used a discretized versions of the Wilcock and Crowe (2003) sediment transport equation to model fractional sediment transport and Exner equation (Exner, 1925) to model elevation change. ASIM also follows methods developed by Viparelli et al. (2010) to allow for cyclical aggradation and degradation of the substrate. Novel aspects of the new formulation of these algorithms include the allowance for side tributaries to be modelled and for the width and length of reaches to vary, which is particularly important in mountainous catchments. Another novelty relative to other models is that ASIM can be linked with FAST and the Raven hydrological model. These programs allow for the results to be upscaled to the landscape scale very quickly. Figure 4-1 shows the model workflow and the order of reach processes being calculated.

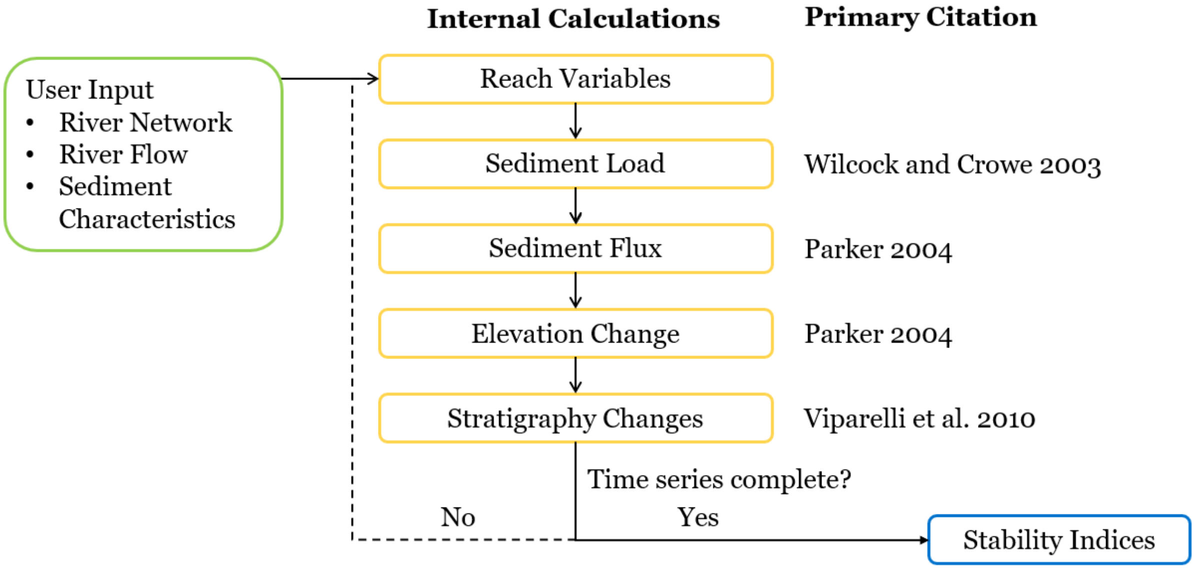

Figure 4-1: ASIM workflow. Citations indicate the primary resource for the methods being applied

4.1.1 Model Inputs

ASIM requires three sets of data from external sources: river network details, flow data, and characterization of the surficial and substrate GSDs in the river channel and sediment flowing into the upstream boundaries.

River Network

The river network describes the geographical properties of the modelled reaches within the river basin. ASIM processes variables that are associated with two types of elements: reaches and nodes. The river network details are loaded into ASIM through a list of reaches. Nodes only contain elevation information and are initiated from the reach descriptions. Reaches in the river network are sorted by catchment area so that downstream reaches do not precede reaches that flow into them. The reach details required in ASIM include the following information:

- Reach number: numerical index used to identify the reach
- Reach length: horizontal distance from the upstream node to the downstream node
- Catchment area: land area where surface runoff would flow into the upstream node of the reach
- Start elevation: elevation of the upstream node
- End elevation: elevation of the downstream node
- Drains from: numerical index of the upstream node
- Drains to: numerical index of the downstream node

A schematic of how a typical reach is discretized is shown in Figure 4-2. The discretization method in ASIM resembles RubarBE (El Kadi Abderrezzak et al., 2008; El Kadi Abderrezzak & Paquier, 2009), where the hydraulic and sediment transport equations are calculated in cells that are offset from one another. In the case of ASIM, hydraulic equations are calculated at the centre of reaches, and sediment transport loads are calculated at the nodes. For the purposes of mass balance, control volumes are linked to nodes and include half of the sediment volume in the reaches immediately upstream and downstream of a node.

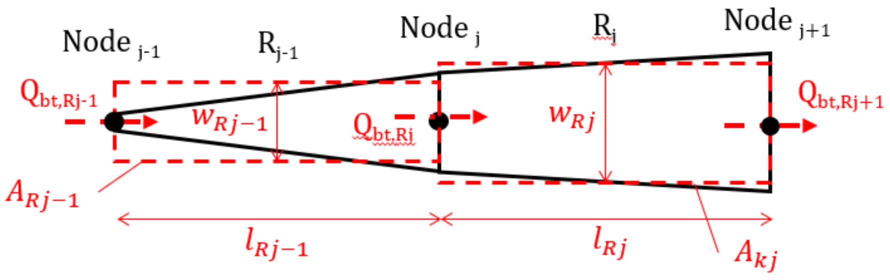

Figure 4-2: Schematic representation of a typical reach

River Flow

River flow is defined using a time series of flow data from a single, nearby location. The Raven hydrological model was used to generate the hydrological data for the development and testing of ASIM, but historical flow from a nearby gauge could also be used. The flow time series used for testing model functionality is publically available and can be requested through the University of Waterloo. Flow in each reach is scaled assuming a linear relationship relative to the catchment area (Vianello & D'Agostino, 2007; Wolman & Leopold, 1957). This assumption only holds in small catchments with humid climates, so a different relationship would need to be charactized for larger catchments. Flows in individual reaches are scaled with the following equation:

$$Q_{w,j} = Q_{w,M} \frac{A_{C,j}}{A_{C,M}} \tag{4.1}$$

where $Q_{w,j}$ is the river flow in reach j, $A_{C,j}$ is the catchment area upstream of reach j, $Q_{w,M}$ is the river flow at the hydrologic model location, and $A_{C,M}$ is the catchment area at the hydrologic model location. The downstream boundary of the modelled river is the ideal location to collect flow data, but this would not be feasible for many remote catchments. The hydrologic data should be sourced from a nearby catchment with similar weather patterns and geography for locations without any direct measurements.

Sediment Supply

ASIM handles the GSD information for three types of sediment:

- Feed distribution: the sediment flowing into the river at the upstream boundaries
- Substrate distribution: the sediment below the active layer in the river channel
- Reach active layer distribution: the sediment within the active layer for each reach

Each distribution is input as an array of percentiles for each size class following the Wentworth scale. The substrate distribution is assumed to be the same as the active layer distribution because no measurements were taken of the substrate. However, this assumption can be relaxed for rivers with more information describing the substrate. Figure 4-3 shows the sediment layers for Reach 1 and the relative location of bedload transport rates.

User Inputs

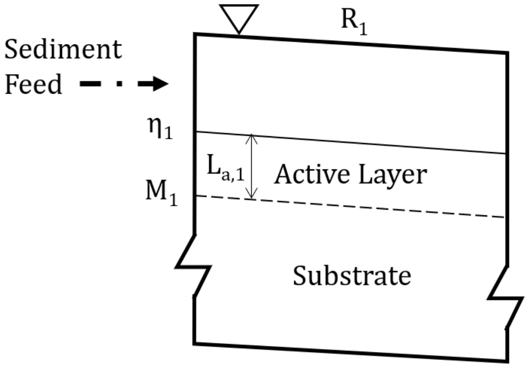

Figure 4-3: Schematic representation of sediment layers in Reach 1

Additional variables based on catchment basin characteristics also need to be specified. Details that must be specified include the following variables:

- Width to catchment area coefficients: These are coefficients used to calculate width based on catchment area using Equation 3.9.
- Substrate layer thickness: Layer thickness should be specified such that a homogeneous GSD is present in each layer, but thinner layers require more computational time. Each substrate layer is initiated with the same GSD.
- Total substrate thickness: This value represents the total thickness of substrate that can be degraded. This value can be seen as the level of bed rock, and if the model reaches this point at any node, it is recommended to adjust the parameters or extent the substrate thickness.
- Feed rate: The sediment load defined at the upstream boundaries.

4.1.2 Model Fundamentals

The driving principles in ASIM stem from research by G. Parker (1991) and Cui et al. (1996) who provide a version of the Exner equation that is related to fractional sediment transport. The Exner equations summarized by Cui et al. (1996) describe the change in channel elevation and sediment fractions over time caused by changes in sediment flux and active layer thickness. The continuous differential equations describe the mass balance of sediment that occurs through a river network and are as follows:

$$\frac{\partial \eta}{\partial t} + \frac{1}{1-\lambda_p}\frac{\partial q_{bT}}{\partial x} = 0 \tag{4.2}$$

$$\frac{\partial}{\partial t}(L_a F_i) + \frac{1}{1-\lambda_p}\left(\frac{\partial q_{bT} p_{bi}}{\partial x} - f_{I,i}\frac{\partial q_{bT}}{\partial x}\right) = f_{I,i}\frac{\partial L_a}{\partial t},\ i = 1, 2, ... \tag{4.3}$$

where η is the elevation of node j (masl), λ_p is the sediment porosity (%), t is the time after start date (s), $f_{l,i}$ is the fraction of sediment exchanged between the substrate and surface material in the ith size class (%), L_a is the active layer thickness (m), F_i is the fraction of surface material in the ith size class (%), q_{bT} is the total unit bedload transport rate (m^2/s), p_{bi} is the bedload transport fraction for size class i (%). The discretized representations of these equations were shown by G. Parker (2004) and are as follows:

$$\eta_j\big|_{t+\Delta t} = \eta_j - \frac{1}{1-\lambda_p}\left.\frac{\partial q_{bT}}{\partial x}\right|_j \Delta t \tag{4.4}$$

$$F_{i,j}\big|_{t+\Delta t} = F_{i,j} - \frac{1}{L_{a,j}}(F_{i,j} - f_{li,k})\frac{\partial L_{a,j}}{\partial t}\Delta t + \frac{1}{L_{a,j}(1-\lambda_p)}\left(-\left.\frac{\partial q_{bT} p_{bi}}{\partial x}\right|_j + f_{li,j}\left.\frac{\partial q_{bT}}{\partial x}\right|_j\right)\Delta t \tag{4.5}$$

where the subscript j indicates the node or reach index related to each term. The control volumes for the mass balance following these equations are connected to the nodes between each reach and not the reaches themselves. Both of the previous equations are driven by the sediment flux across each control volume. The sediment flux across the control volume j is described as the change in sediment transport rates across the reaches upstream and downstream of node j. The equations used in ASIM originate from the unit sediment flux and fraction unit sediment flux described by G. Parker (2004) for a model with constant nodal spacing and channel width along the entire domain:

$$\left.\frac{\partial q_{bT}}{\partial x}\right|_j = a_u \frac{q_{bT,j} - q_{bT,j-1}}{\Delta x} + (1 - a_u)\frac{q_{bT,j+1} - q_{bT,j}}{\Delta x} \tag{4.6}$$

$$\left.\frac{\partial q_{bT} p_i}{\partial x}\right|_j = a_u \frac{q_{bT,j} p_{bi,j} - q_{bT,j-1} p_{bi,j-1}}{\Delta x} + (1 - a_u)\frac{q_{bT,j+1} p_{bi,j+1} - q_{bT,j} p_{bi,j}}{\Delta x} \tag{4.7}$$

where Δx is the distance between nodes (m), and $a_u = 0.75$ is the upwinding coefficient (G. Parker, 2004). The following equations are also fundamental to the processes described in Equations 4.4 and 4.5.

$$f_{li,j} = \begin{cases} f_{s,i,int,j} & \text{for } \left.\frac{\partial \eta}{\partial t}\right|_j < 0 \text{ (degradation)} \\ \alpha F_{i,j} + (1 - \alpha) p_{bi,j} & \text{for } \left.\frac{\partial \eta}{\partial t}\right|_j > 0 \text{ (aggradation)} \end{cases} \tag{4.8}$$

$$\frac{\partial L_{a,j}}{\partial t} \Delta t \cong L_{a,j} - L_{a,j,old} \tag{4.9}$$

where $\alpha = 0.5$ is the coefficient of material transferred to the substrate as the river bed aggrades (Hoey & Ferguson, 1994; Toro-Escobar et al., 1996), $f_{s,i,int,j}$ is the fraction of material in the top substrate layer in the ith size class in reach j (%), and $L_{a,j,old}$ is the active layer thickness of the previous time step in reach j (m). Equation 4.8 describes the sediment fractions that will be introduced to the active layer and differs for conditions of aggradation and degradation. Equation 4.9 is a simplification to describe the change in active layer thickness across time intervals.

4.1.3 Calculate Reach Variables

ASIM initiates each time step by updating reach variables that describe the conditions at the onset of each day. These variables are dependent on results from the previous time step but do not depend on neighbouring reaches within the current time step. These variables describe the reach as a whole and are not specific to any single grain size. The reach variables, the applicable equations used for their calculation, and citations are listed in this subsection.

Unit flow:

$$q_{w,j} = Q_{w,j}/w_j \tag{4.10}$$

where $q_{w,j}$ is the river flow per unit width in reach j (m^2/s).

Slope:

$$S_j = \frac{\eta_j - \eta_{j-1}}{l_j} \tag{4.11}$$

D$_{50}$: Refer to Equation 3.8

D$_{90}$: Refer to Equation 3.8

D$_{gm}$: Refer to Equation 3.6

Roughness height:

$$k_{s,j} = n_k D_{90,j} \tag{4.12}$$

where $k_{s,j}$ is the roughness height (m) and $n_k = 2$ is the roughness height coefficient (Kamphuis, 1974; G. Parker, 1990).

Active thickness:

$$L_{a,j} = n_a D_{90,j} \tag{4.13}$$

where $n_a = 2$ is the active layer coefficient (G. Parker, 2004).

Fraction sand:

$F_{s,j}$ is the surface sand fraction in reach j (%) and equals the fraction of sediment that is less than or equal to 1 Ψ.

Shear velocity:

$$u_{*,j} = \left(\frac{k_{s,j}^{1/3} q_w^2}{\alpha_r^2} \right)^{3/20} g^{7/20} S_j^{7/20} \tag{4.14}$$

where $u_{*,j}$ is the shear velocity of reach j (m/s), $\alpha_r = 8.1$ is the Manning-Strickler resistance coefficient, S_j is the channel slope of reach j (m/m) (G. Parker, 1990).

Shields number:

$$\tau^*_{sg,j} = \left(\frac{k_{s,j}^{1/3} q_w^2}{\alpha_r^2 g}\right)^{3/10} \frac{S_j^{7/10}}{RD_{sg,j}} \tag{4.15}$$

where $\tau^*_{sg,j}$ is the Shields number based on the surface geometric mean size of reach j, R is the submerged specific gravity of sediment, and S_j is the channel slope of reach k (G. Parker, 2004).

Critical Shields number:

$$\tau^*_{ssrg,j} = 0.021 + 0.015\exp(-20F_{s,j}) \tag{4.16}$$

where $\tau^*_{ssrg,j}$ is the critical Shields number in reach j calculated from the surface sand fraction (Wilcock & Crowe, 2003).

4.1.4 Calculate Sediment Load

The sediment load is calculated using the sediment transport function developed by Wilcock and Crowe (2003) and discretized following methods by Cui et al. (1996) and G. Parker (2004). Sediment load is calculated at each node in the current time step before sediment flux is calculated.

Unit sediment flow for each grain size:

$$q_{bi,j} = F_{i,j}\frac{u_{*,j}^3}{Rg}W^*_{i,j} \tag{4.17}$$

$$W^*_{i,j} \begin{cases} 0.002\phi_{i,j}^{7.5} & \textbf{for } \phi_{i,j} < 1.35 \\ 14\left(1 - \frac{0.894}{\phi_{i,j}^{0.5}}\right)^{4.5} & \textbf{for } \phi_{i,j} \geq 1.35 \end{cases} \tag{4.18}$$

$$\phi_{i,j} = \frac{\tau^*_{sg,j}}{\tau^*_{ssrg,j}}\left(\frac{D_i}{D_{sg,j}}\right)^{-b_{i,j}} \tag{4.19}$$

$$b_{i,j} = \frac{0.67}{1 + \exp(1.5 - D_i/D_{gm,j})} \tag{4.20}$$

where $q_{bi,j}$ is the unit sediment transport rate for size class i at node j (m^2/s), $W^*_{i,j}$ is the dimensionless unit sediment transport rate for size class i at node j, $\phi_{i,j}$ is a regression variable, $b_{i,j}$ is the hiding function for size class i in reach j, D_i is the representative diameter of size class i (mm).

Total unit sediment flow:

$$q_{bT,j} = \sum_{i=1}^{n_s} q_{bi,j} \tag{4.21}$$

Bedload fraction:

$$p_{bi,j} = \frac{q_{bi,j}}{q_{bT,j}} \tag{4.22}$$

Total sediment flow:

$$Q_{bT,j} = q_{bT,j} w_j \tag{4.23}$$

where $Q_{bT,j}$ is the total bedload transport rate at node j (m^3/s).

4.1.5 Calculate Sediment Flux

Adjustments had to be made to equations 4.6 and 4.7 to account for reaches with variable lengths and widths. Firstly, the unit sediment flow calculated at each node was converted to total sediment flow by multiplying by the width to maintain continuity in the sediment mass balance. Secondly, the Δx term was adjusted to represent the horizontal area of the river that will change in elevation due to a change in node elevation. The resulting equation for unit sediment flux is:

$$\left.\frac{\partial q_{bT}}{\partial x}\right|_j = a_u \frac{2Q_{bT,j} - Q_{bT,j-1}}{l_{j-1}w_{j-1} + l_j w_j} + (1 - a_u)\frac{2Q_{bT,j+1} - Q_{bT,j}}{l_{j-1}w_{j-1} + l_j w_j} \tag{4.24}$$

where l_j is the length of reach j (m) and w_j is the width of reach j (m).

Simplified unit sediment flux

ASIM differs from Parker's model not only in that the reaches have variable widths and lengths, but side channels and confluences can also be added. Equation 4.24 was simplified for the calculations at atypical reaches, which include upstream and downstream boundaries as well as reaches immediately upstream and downstream of confluences. The simplified versions of Equation 4.24 is:

$$\left.\frac{\partial q_{bT}}{\partial x}\right|_{j} = \frac{2}{A_j}(a_u Q_{up,j} + (1 - a_u)Q_{down,j}) \tag{4.25}$$

where A_j is the river area linked to the elevation of node j (m^2), $Q_{up,j}$ is the change in total sediment flow in the reach immediately upstream of node j (m^3/s), and $Q_{down,j}$ is the change in total sediment flow in the reach immediately downstream of node j (m^3/s). Figure 4-4 shows a schematic that includes each of the atypical sections, and Table 4.1 shows how the equations for each type of reach have been adjusted. Note that a reach can to fall within two atypical categories (e.g. a reach at an upstream boundary could also be immediately upstream of a confluence in which case the "upstream boundary" and "upstream of confluence" adjustments would both be applied).

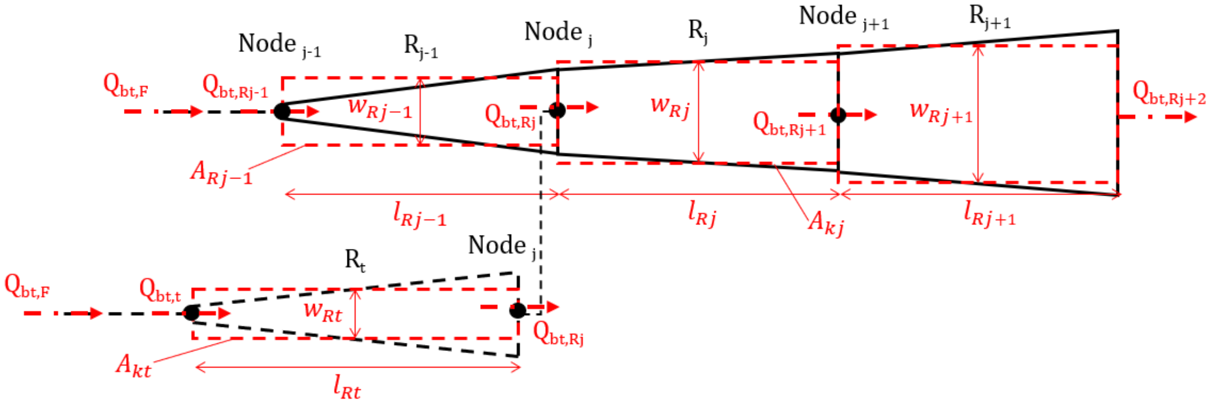

Figure 4-4: Schematic representation depicting each atypical reach type

Table 4.1: Variable adjustments for atypical reaches

Variable	Typical Section	Upstream Boundary	Downstream Boundary	Upstream of Confluence	Downstream of Confluence
A_j	$l_{j-1} * w_{j-1} + l_j * w_j$	$l_j * w_j$	Typ.	Typ.	$l_{Ri-1}w_{Ri-1} + l_{Ri}w_{Ri} + l_{Rt}w_{Rt}$
Q_{up}	$Q_{bT,j} - Q_{bT,j-1}$	$Q_{bT,j} - Q_{bT,F}$	Typ.	Typ.	$Q_{bT,j} - Q_{bT,t} - Q_{bT,j-1}$
Q_{down}	$Q_{bT,j+1} - Q_{bT,j}$	Typ.	0	$rQ_{bT,j+1} - Q_{bT,j}$	Typ.

4.1.6 Calculate Stratigraphy Change

G. Parker's (2004) model does not contain a memory of sediment fractions in the substrate. It is not necessary to have a memory of the substrate for systems that only aggrade or degrade. However, information will be lost for systems that undergo cycles of both aggradation and degradation. Stratigraphy memory in ASIM follows the same approach as Viparelli et al. (2010), which is based on research by Hoey and Ferguson (1994). The substrate is recorded in layers of constant thickness, and a variable datum is set to a constant depth below the initial bed elevation. Figures 4-5 and 4-6 show how the stratigraphy is stored in the model. The number of layers is calculated at the start of the model run and each time step using the following equation.

$$M_j|_{t=0} = \left\lfloor \left(\frac{\eta_j|_{t=0} - L_{a,j}|_{t=0}}{L_s} \right) \right\rfloor + 2 \tag{4.26}$$

where M_j is elevation of the interface between the active layer and substrate at node j (masl) and L_s is the maximum thickness of substrate layers (m).

For time steps with aggradation, the thickness of the top layer of the substrate will increase, and the sediment fraction in that layer will adjust. There are two cases that can happen when the substrate aggrades. The first case is that the interface between the active layer and substrate will rise in elevation, but the thickness of the top layer will remain less than the maximum thickness (L_s) and no new layer will be added. This case

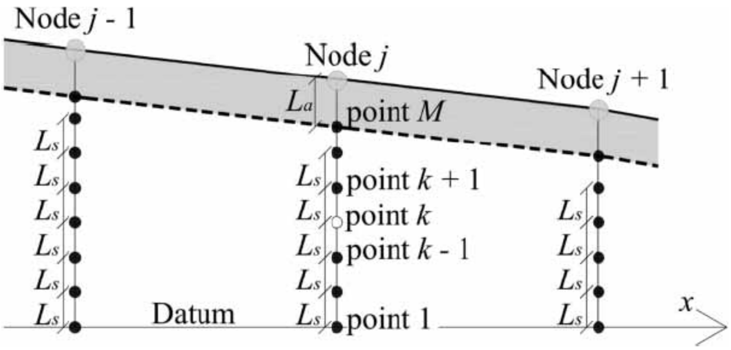

Figure 4-5: Schematic representation of the initial stratigraphy; from Viparelli et al. (2010). Illustration of grid used to track stratigraphic bed structure. (-) Bed elevation, (- -) active layer - substrate interface, (o) grain size distribution in this node is representative of layer between point $k-1$ and point k.

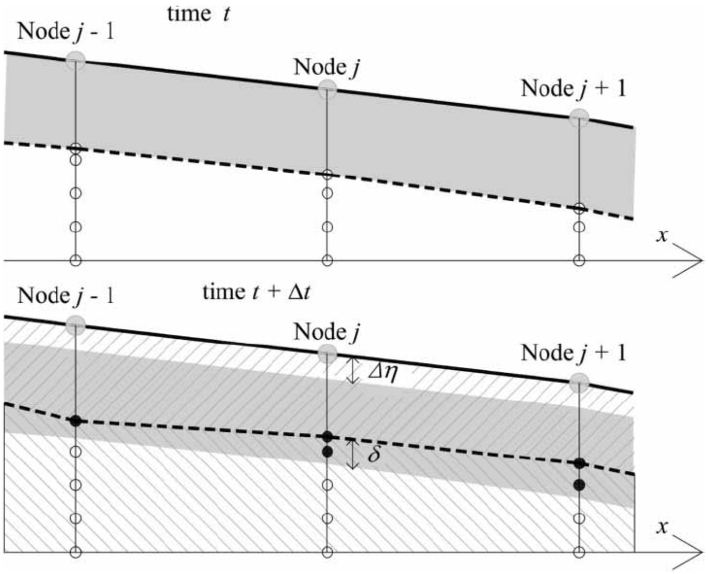

Figure 4-6: Stratigraphy for aggradation case; from Viparelli et al. (2010). Illustration of how grid changes as bed aggrades. (•) Grid extension to store newly-created stratigraphy as bed changes from time t to time $t + \Delta t$. At node $j-1$ the uppermost grid point is displaced upward. At nodes j and $j+1$, new grid points are added.

can be described with the following equation:

$$\eta_{int,j}\big|_{t+\Delta t} \leq (M_j\big|_{t+\Delta t} - 1)L_s = (M_j\big|_t - 1)L_s \tag{4.27}$$

where η_{int} is the elevation of the interface between the active layer and substrate (masl). If no new substrate layer is added, the sediment fractions in the top layer of the substrate are calculated with the following equations:

$$f_{i,j,M}\big|_{t+\Delta t} = \frac{\{f_{i,j,M}\left[\eta_{int,j} - (M_j - 2)L_s\right]\}\big|_t + \delta_j f_{Ii,j}}{\left[\eta_{int,j} - (M_j - 2)L_s\right]\big|_t + \delta_j} \tag{4.28}$$

$$\delta_j = \eta_{int,j}\big|_{t+Dt} - \eta_{int,j}\big|_t = (\eta_j - n_a D_{s90,j})\big|_{t+\Delta t} - (\eta_j - n_a D_{s90,j})\big|_t \tag{4.29}$$

where δ_j is the change in elevation of the interface between the active layer and substrate at node j (m).

The second case covers instances where the substrate aggrades and the top substrate layer exceeds the maximum thickness, so a new substrate layer is required. It is possible that more than one layer would need to be added, so the new number of storage layers is calculated with the following equation:

$$M_j\big|_{t+\Delta t} = \left\lfloor \left(\frac{\eta_j - L_{a,j}}{L_s}\right) \right\rfloor\Bigg|_{t+\Delta t} + 2 \tag{4.30}$$

The new layers will have fractions of sediment equal to the exchange fraction, and the previous, top layer of sediment will have sediment fractions calculated with the following equation:

$$f_{i,j,(M-1)}\Big|_{t+\Delta t} = \frac{\left\{f_{i,j,(M-1)}\left[\eta_{int,j} - (M_j - 2)L_s\right]\right\}\Big|_t}{L_s} + \frac{\left[(M_j - 1)L_s - \eta_{int,j}\right]\big|_t f_{Ii,j}}{L_s} \tag{4.31}$$

Calculating the sediment fraction after the substrate degrades is much simpler than when it aggrades, and the sediment fraction in the stratigraphy layers remains the same. Still, the number of layers and top layer thickness adjusts to account for the elevation lost.

4.2 Model Analysis

4.2.1 Model Checks

Model Continuity and Mass Balance

ASIM simulates sediment transport in a river network by iterating through a time series of hydrologic conditions and updating sediment volume by adjusting channel elevation at each time step. The change in sediment volume stored in the model should be accounted for in the sediment gained and lost at the upstream and downstream boundaries, respectively. The continuity in the model was checked with a mass balance calculation to identify if the change in volume in the stream bed reflects the sediment flux at the upstream and downstream boundaries. Total volume was calculated for initial conditions and after the model was run. The cumulative sediment flux for the system was measured at each time step using the following equations:

$$V = \sum_{j=1}^{n} l_j w_j \frac{T_j + T_{j+1}}{2} \tag{4.32}$$

$$V_{in} = \sum_{k=1}^{m} \frac{a_u q_{bT,F,k} + (1 - a_u) q_{bT,1,k}}{1 - \lambda_p} \Delta t \tag{4.33}$$

$$V_{out} = \sum_{k=1}^{m} \frac{q_{bT,n,k}}{1 - \lambda_p} \Delta t \tag{4.34}$$

where V is the total sediment volume in the model domain (m^3), T_j is the total sediment thickness in reach j (m), m is the total number of time steps, n is the total number of reaches, j is a counting variable describing the reach or node index, and k is a counting variable describing the time step.

The mass of each grain size was similarly checked using the adjusted equations:

$$V_i = \sum_{j=1}^{n} \sum_{k=1}^{m} l_j w_j \frac{T_{j,k} F_{i,j,k} + T_{j+1,k} F_{i,j+1,k}}{2} \tag{4.35}$$

$$V_{i,in} = \sum_{k=1}^{m} \frac{a_u q_{bi,F,k} + (1 - a_u) q_{bi,1,k}}{1 - \lambda_p} \Delta t \tag{4.36}$$

$$V_{i,out} = \sum_{k=1}^{m} \frac{q_{bi,n,k}}{1 - \lambda_p} \Delta t \tag{4.37}$$

Comparison to Parker

ASIM uses functionality from the model developed by G. Parker (2004) and made available for Excel. Model functionality in ASIM was checked using the same conditions as an example from Parker to identify if the model was performing as expected. There were three minor changes made in ASIM that resulted in differences. The difference in elevation simulations was compared to identify the significance of each change. The following changes were sequentially applied in ASIM to see how each one affects the final elevation:

- **Change 1**: the downstream sediment transport is calculated by assuming the sediment load in the last two nodes are equal;
- **Change 2**: a factor of two is applied to the upstream boundary sediment load in ASIM; and
- **Change 3**: channel slope is calculated in each reach instead of averaged across 3 nodes.

4.2.2 Modelled Scenarios

A series of scenarios were prepared to test the functionality of ASIM for Chauncey Creek. River geometry, flow, and initial sediment conditions were developed for a scenario that all other scenarios were based on and compared. This scenario is now referred to as the “Existing Scenario”.

The river network details were extracted from the CDEM and NHN (Natural Resources Canada, 2015, 2016a) for the Chauncey Creek basin using FAST. A total of 45 reaches were delineated between confluence locations where tributaries are defined in the shapefile from the NHN. Channel width is often difficult to extract from DEMs for mountain channels because the resolution of the DEM is too large relative to the channel width. Channel width was therefore calculated using a power function and the catchment area (Equation 3.9). The variables of the power function depend on the specific catchment and are shown in 3-17 for Chauncey Creek. The existing geomorphic conditions were based on measurements taken in the field and strive to match field conditions as closely as possible.

The hydrological flow data for this study were obtained from Raven simulations of a nearby catchment. The nearby catchment is located to the south of Chauncey Creek and has a catchment area of 136 km^2, which is roughly four times the size of Chauncey Creek. Although precipitation is highly variable in mountain regions, the nearby catchment was deemed to be appropriate because of the similarities in topographic relief and land coverage. The Raven model was calibrated using historical precipitation and flow data before being extended to a 105-year time-frame. The selected model was developed and calibrated by the team at SNC Lavalin for a nearby project and exemplified the ability that ASIM has to link with other studies. The Existing Scenario uses the first half of the synthetic flow data from the Raven model.

ASIM is a discretized model, so it would hypothetically be possible to measure the GSD from the field for each reach, but this would be very time-consuming. There would also be lost information when the measured particle sizes are combined into a single distribution for each reach. There were only seven discrete locations where the surficial GSD was measured in Chauncey Creek, so a synthetic GSD that could be interpolated at each reach based on a stream power index was developed for the initial conditions throughout the model domain. The function describing synthetic GSDs was calibrated to match the measured Ψ_m and Ψ_{90} as closely as possible and allowed for the creation of GSDs in regions that were not measured. The measured relationship only includes reaches with a stream power index ranging from 0.08 to 0.16, but this was expanded to a range of 0.06 to 0.20 for curve fitting. Other statistics that were considered when developing the synthetic distributions include sorting and skewness (Table 3.10).

All field GSD measurements (in Ψ units) were found to fit a Gaussian distribution better than a Rosin distribution, so Gaussian distributions were the starting point for developing a synthetic GSD that could be applied throughout the catchment. Distributions were assumed to have a mean and standard deviation that followed a power-law relative to the stream power index in a similar manner as the Ψ_{90}. GSDs were calculated using Equation 3.10 and the Ψ_m and Ψ_{90} were calculated using Equations 3.6 and 3.8, respectively. The coefficients for the power functions describing the mean and standard deviation relative to the stream power index ($\mu = a_\mu \omega'^{b_\mu}$, $\sigma^2 = a_\sigma \omega'^{b_\sigma}$) were found using two optimization methods where the function being optimized is described as:

$$f = \sum_{\omega' \in S} \Big| \Psi_{m,syn}(\omega') - \Psi_{m,obs} \Big| + 2 \Big| \Psi_{90,syn}(\omega') - \Psi_{90,obs} \Big| \tag{4.38}$$

where S is a series of ω' ranging from 0.06 to 0.20 in increments of 0.02. A higher weighting (a factor of 2) was applied to the Ψ_{90} because there was a more positive correlation between the Ψ_{90} and ω' than there was for Ψ_m. Initial attempts to find a global minimum resulted only in local minima, so a two step optimization approach was used. The grid search function in R was used first to narrow in on a global minimum and provide more suitable starting parameters for the Nelder-Mead and Hooke-Jeeves optimization algorithms (Kelley, 1999).

The GSDs measurements were often skewed slightly toward fine material, so synthetic GSDs that follow a "skew-normal" distribution were checked for suitability. The density function for the skew-normal distribution is similar to a normal distribution; it is a function of the mean and standard deviation, but there is an additional term, alpha, which indicates the degree of skewness that the distribution has (Azzalini, 1985, 2005). Alpha was not included as a variable to be optimized because it was found to trend toward a negative skew (skew toward coarse material) as opposed to a positive skew. A value of -0.2 was assumed for alpha when optimizing the skew-normal distribution.

The feed distribution was based on a Rosin distribution (Equation 3.12) to more closely match sediment load coming from hillslopes. A sorting coefficient (s_R) of -1.1 was selected to match similar sorting coefficients measured in the survey locations SL04, SL05, SL07 and SL08. The mode was selected as 64 mm (6 Ψ) to match survey location SL08 and to provide a distribution that would fit more cleanly within the truncation limits of the GSDs. The synthetic distributions were truncated so that the entire GSD would span from passing sieve sizes 4 Ψ to 9 Ψ.

Varied Hydrologic Scenarios

A set of simulations with various hydrologic time frames were completed to analyze how the model results would change for different hydrologic conditions and the same initial geomorphological conditions. This analysis was done to evaluate the sensitivity to hydrological forcing data and to identify the speed at which changes occur. Scenarios that exceed 105 years of duration experience a repeat of the same hydrologic data. Four additional hydrologic scenarios were simulated, and Table 4.3 shows the numerical details for each flow scenario.

- **Alternate Scenario**: A simulation that used the second half of the hydrologic time series.
- **Increased Scenario**: A simulation that used the first half of the hydrologic time series where each of the daily flows was increased by 10%.
- **Extended Scenario**: A simulation that used the entire hydrologic time series.
- **Looped Scenario**: A simulation that used the entire hydrologic time series six consecutive times.

Varied Geomorphic Scenarios

Two scenarios with different geomorphic conditions were simulated to evaluate how changing the river width in a reach would affect sediment transport upstream and downstream from the constriction or expansion. A narrow channel could be the result of installing a

Table 4.2: Flows scenarios

Statistic	Units	Existing	Alternate	Increased	Extended	Looped
Total days modelled	years	53	53	53	106	636
Average flow	m^3/s	0.40	0.47	0.44	0.44	0.44
Days exceeding 2 m^3/s	days	523	762	681	1285	6425
Max flow	m^3/s	6.68	9.11	7.35	9.11	9.11
2-year flood	m^3/s	3.45	3.61	3.79	3.61	3.61
5-year flood	m^3/s	4.89	5.02	5.38	4.89	4.89
20-year flood	m^3/s	6.39	6.70	7.03	6.62	6.62
50-year flood	m^3/s	6.68	9.11	7.35	8.15	8.15

Note: All flows are applicable at the downstream boundary of Chauncey Creek and are based on a catchment area of 34.8 km^2

bridge with structural supports that encroach on the bankfull width of the river, and an expansion could be a construct of river rehabilitation projects. The geomorphic scenarios are describe as the following:

- **Narrow Scenario**: A reach with slope 3.5% and 28 m length was adjusted to be 4.5 m instead of 9.2 m.
- **Wide Scenario**: A reach with slope 2.1% and 327 m length was adjusted to be 30 m instead of 9.2 m.

All scenarios that were used for comparing geomorphic conditions use the same flow series and GSDs as the Existing Scenario.

4.2.3 Geomorphological Indices

The ultimate goal of ASIM is to describe risk to infrastructure by characterizing the channel stability. S. A. Schumm's (1963) definition for a stable channel is "one that shows no progressive change in gradient, dimensions, or shape". It is generally assumed in fluvial geomorphology that rivers will trend toward a condition of quasi-equilibrium (Mackin, 1948; S. A. Schumm, 1985). Whether they are in a state of quasi-equilibrium or not, alluvial rivers will experience fluctuations in elevation, slope, sediment transported, and sediment calibre as seasonal and annual variations in water and sediment loading occur (S. A. Schumm, 1963; Charlton, 2007; García, 2008b). The model output was designed to highlight geomorphologic changes that would be critical for the design of linear infrastructure and rate those changes at the reach scale to represent the relative stability within the modelled domain. Four geomorphic indices were characterized to indicate the relative stability of each reach. The stability indices represent the change in a variable over the duration of the model simulation and include:

- **Elevation**: Long term changes in elevation are important for the design of both bridges and pipelines. Bridge designs need to make sure there is enough area below the bridge deck for water to flow under, but channel degradation and scour below the structural elements could also cause failure. Buried pipelines are less susceptible to rises in channel elevation, but exposure is possible in the case that the channel elevation decreases.
- **Slope**: Changes in slope could result in stronger small scale hydraulic forces to structural elements or erosion protection.
- **Surficial** D_{90}: Changes to surficial GSDs could affect local scour calculations.
- **Overall stability**: This is an overall indicator that represents a summary of the other indicators. This is currently the normalized sum of the absolute values of the previous three indices. However, individual indicators could be scaled depending on the application. For instance, if elevation is deemed to be unimportant, it could be given half or no weighting in the final calculation.

Each index was normalized by the absolute value of the reach with the greatest change. The elevation, slope, and surficial D_{90} indices include positive and negative changes, so those indices range from -1 to 1. The hydrologic and geomorphic scenario comparisons will evaluate how the relative stability of each reach varies for the conditions selected.

4.3 Modelling Results

4.3.1 Model Continuity

A mass balance check was completed for each run, and the results for the Existing Scenario are shown in Figure 4-7. The reach widths and lengths remain constant throughout the model, so all changes in volume are the result of changes in sediment layer thicknesses. Change in volume of individual particle size classes are also the result of changes to the GSD in each layer. The change in total mass throughout the model domain was balanced and could be explained by the mass entering the upstream boundary and mass discharged at the downstream boundary. The volume of sediment in the active layer increased rapidly at the start of the time series and continued to increase throughout the remaining time steps gradually. The active layer thickness is calculated from the D_{90}, so an increase in active layer volume reflects a coarsening trend and a more significant portion of fine sediment being discharged. The total sediment discharged from the downstream boundary was relatively constant but appeared to increase near the end of the modelling period.

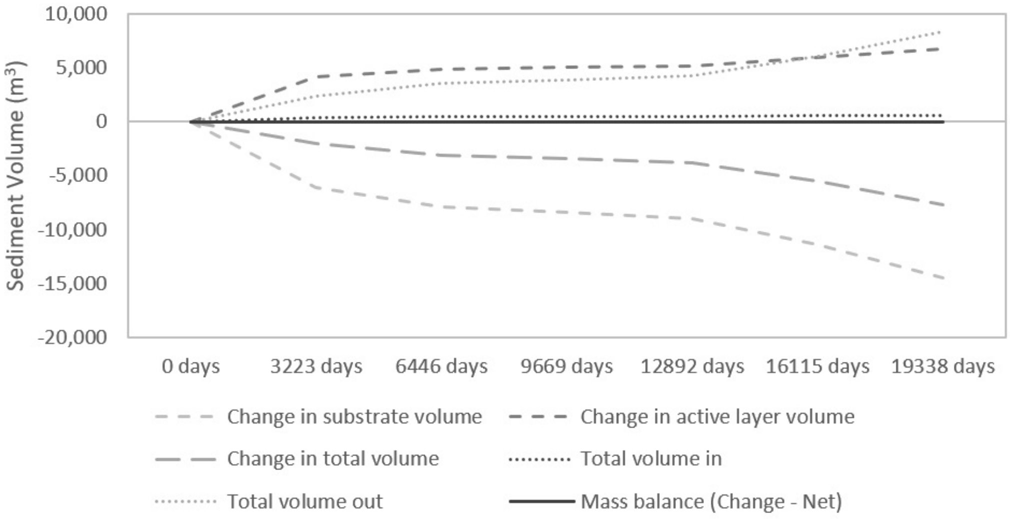

Figure 4-7: Changes in sediment volume for the Existing Scenario

The mass balance of individual particle sizes revealed that there was an imbalance. The volume for coarse gravel in the Existing Scenario is shown as an example in Figure 4-8. This figure shows that the total volume of coarse gravel consistently decreases, but volume in the substrate initially increases. The total volume and volume of coarse gravel decreases after the active layer thickness becomes stable. The imbalance of individual particle size classes indicates that 71 m^3 of coarse gravel disappears, which equates to 2.3% of the initial volume of coarse gravel in the active layer. Equations 4.5, 4.8, and 4.9 are used to calculate new sediment fractions and are the likely source of the mass imbalance. Another potential source of the imbalance is the calculation of sediment transfered between the active layer and substrate, but this also uses the exchange fraction calculated from Equation 4.8.

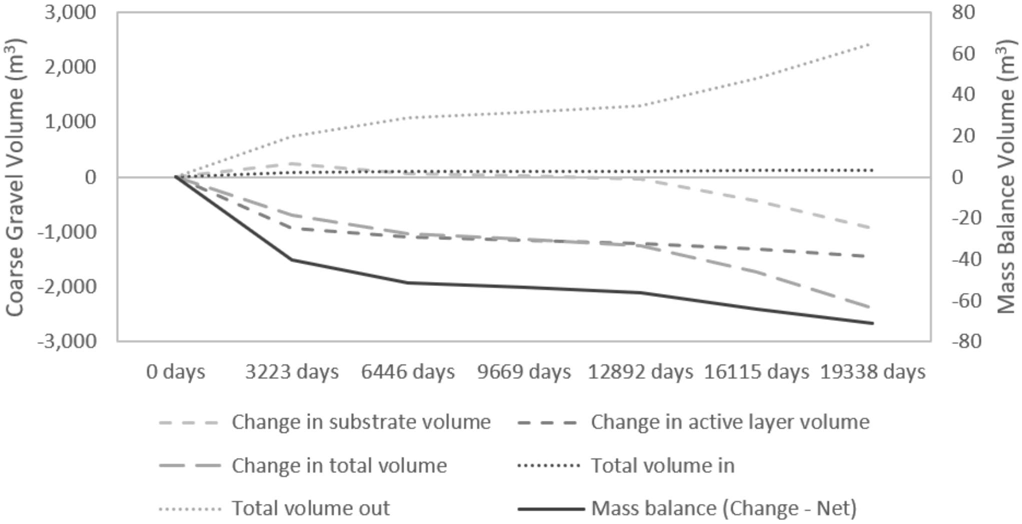

Figure 4-8: Changes in coarse gravel volume for the Existing Scenario

4.3.2 Comparison to Parker

The results from ASIM closely matched that of G. Parker's (2004) model, and only minor differences in the results were observed for changes to model functionality. The change at the downstream boundary (Change 1) had the smallest effect on results and the elevation differed from the results of Parker's model by a maximum of 0.01 m for total elevation changes of as large as 14 m. The change at the upstream boundary (Change 2) resulted in the most significant difference in results, but without this change, the total mass balance was not satisfied. Calculating the slope in every reach instead of across three nodes (Change 3) did not result in a significant difference, but the final elevation became less smooth and appeared to have peaks and troughs with a spacing of two nodes. ASIM was run with the slope calculated across three nodes for the Existing Scenario in Chauncey Creek, and the simulation showed an occurrence of reaches with positive slopes that allowed sediment to be transported through a high point. Figure 4-9 shows the compounding differences that each change made. There is a change between ASIM and Parkers model, but the difference is minor, and the overall functionality remains the same.

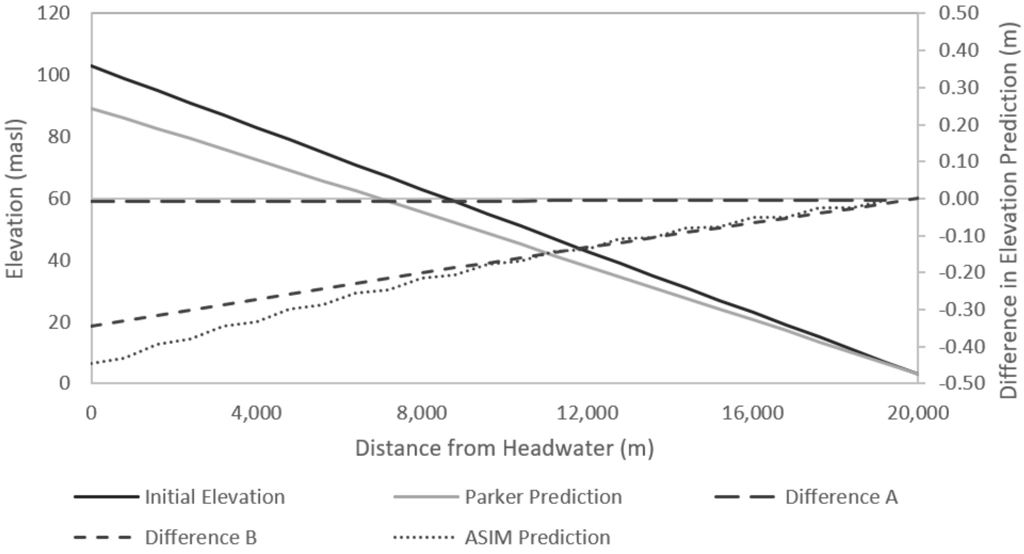

Figure 4-9: Differences between simulations from Parker's model and ASIM. The solid grey line depicts the simulated elevation from Parker's model, and the dashed lines depict the differences from various changes. Difference A corresponds to the results that include Change 1, Difference B corresponds to Changes 1 and 2, and ASIM Prediction corresponds to Changes 1, 2, and 3.

4.3.3 Synthetic Grain Size Distributions

Power function coefficients for calculating the mean and standard deviation from the stream power index were optimized to data collected in the field. The optimized coefficients are shown in Table 4.3. The Gaussian distribution optimization resulted in a smaller value for the goal function, but a similar optimization was found for the skew-normal distribution with an alpha value of -0.2. The probability distribution is shifted toward the coarse particle sizes when using passing sieve sizes instead of retaining sieve sizes, and this shift is more pronounced if full Ψ classes are used. The distribution was first fitted to half Ψ classes before being combined into full Ψ classes for use in ASIM. Bunte and Abt (2001) show the significance of using either the centre of a grain class of the retaining sieve size and how consistency must be maintained. Retaining sieve size was always used. Figures 4-10 and 4-11 show the synthetic GSD for a reaches with a stream power index equal to 0.06 and 0.2, respectively.

Table 4.3: Optimized synthetic distribution parameters

Variable	Gaussian Distribution	Skew-Normal Distribution
a_μ	7.19	8.25
b_μ	0.067	0.104
a_σ	9.71	6.54
b_σ	0.857	0.732
optimization f	1.93	2.24

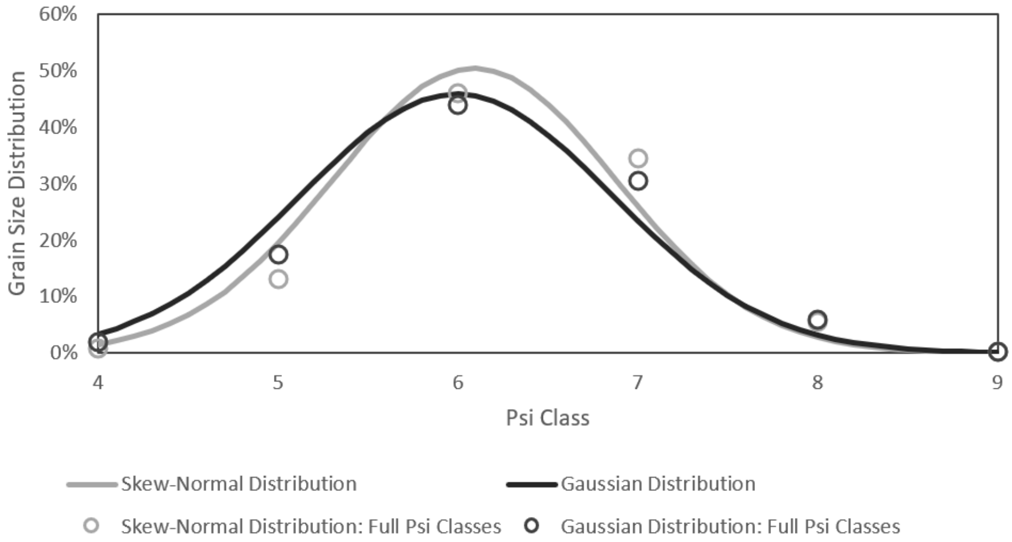

Figure 4-10: Synthetic grain size distributions for reaches with a stream power index of 0.06

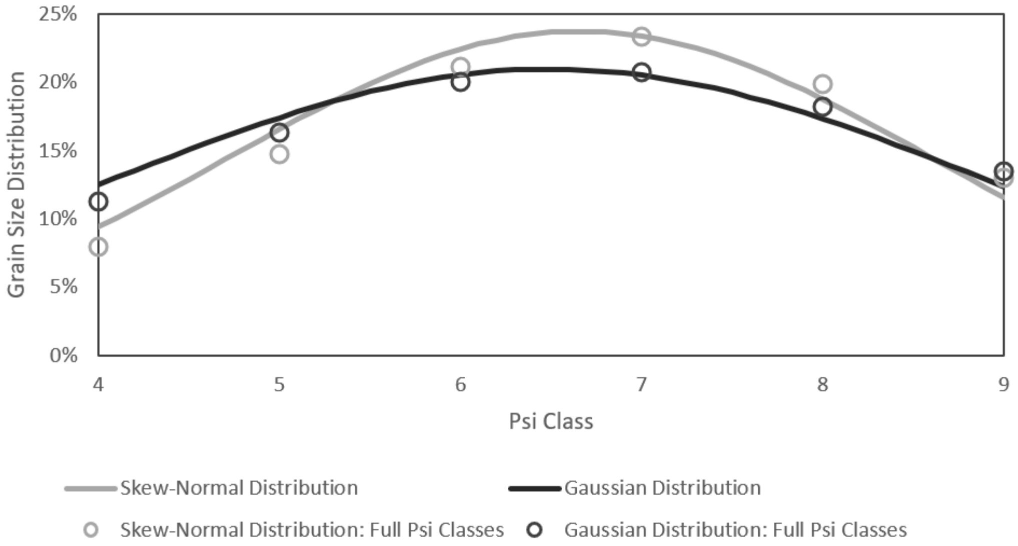

Figure 4-11: Synthetic grain size distribution for reaches with a stream power index of 0.2

4.3.4 Existing Scenario

The Existing Scenario was modelled to identify how ASIM would function for Chauncey Creek and to act as a basis to compare other scenarios. Figure 4-12 shows the elevation change that occurred in the first half of the simulation and after the entire flow time series was complete. The predicted elevation change was greater for the first half of the simulation (26 years), and the largest changes were simulated for reaches in the upper 4 km of the creek. Reaches in areas with a convex slope typically decreased in elevation, and reaches that were in concave areas were predicted to increase in elevation.

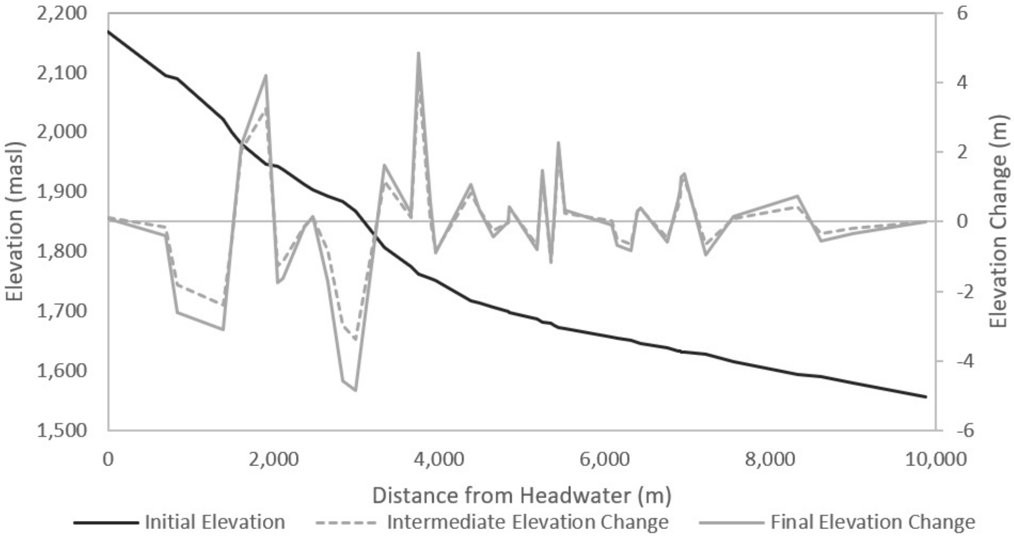

Figure 4-12: Elevation change for the Existing Scenario

The changes to slope after the simulation depict a similar trend as the elevations. Figure 4-13 shows the slope throughout the model domain before, halfway through, and after the simulation. Reaches that are relatively steep compared to nearby reaches were predicted to decrease in slope, and reaches that had relatively shallow slopes were predicted to increase in slope. The slope trends toward a smoother change throughout the catchment, and the absolute slope trend appears to correlate with the overall catchment area. Smaller catchment areas remained steeper than regions with a larger catchment area, but this could just be a reflection of trends in the initial conditions.

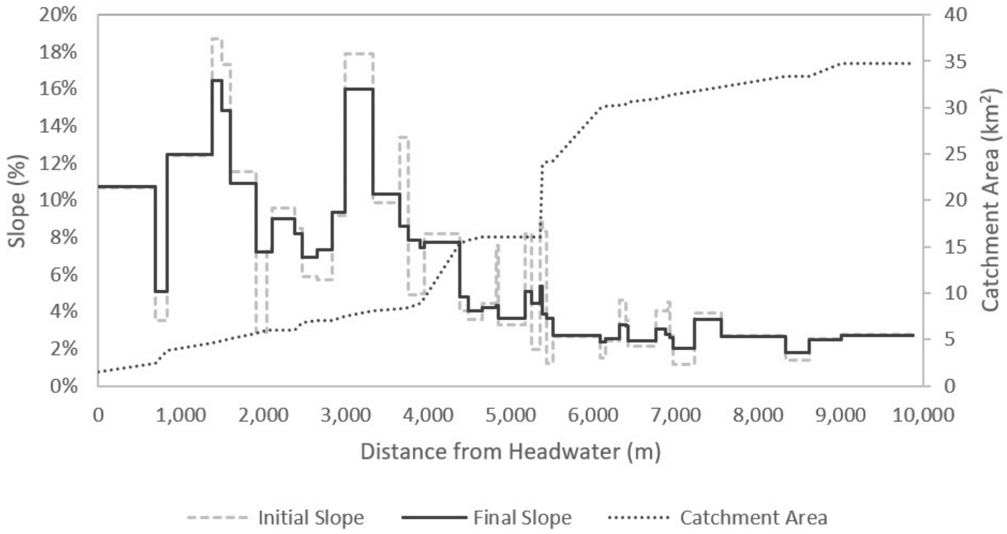

Figure 4-13: Slope change for the Existing Scenario

Figures 4-14 and 4-15 show the sediment distribution in the active layer at t = 0 and t = 19338, respectively. The results show that the majority of gravel is transported through the system and the distribution becomes more coarse as a result. There are variations between 5% and 20% for individual grain sizes from reach to reach, but these differences appear to become more pronounced. The two steepest reaches (roughly 1.5 km and 3 km downstream from the upstream boundary) had the strongest stream power for the initial conditions which corresponds to a larger proportion of boulders. These reaches become even coarser by the end of the model simulation and nearly 50% of the actively was characterized as boulders.

The stability indices are shown in Figures 4-16 to 4-19 and depict the relative stability of each reach. The elevation stability indices indicate that the reaches from 1 km to 4 km are the least stable. Slope is directly linked to elevation, but the slope stability indices indicate that the shorter reaches are less stable. The stability indices related to GSD is fairly consistent and most of the reaches were predicted to have a significant increase in D_{90}. However, there were six reaches spread throughout the catchment that were predicted to have a reduction in D_{90}. The overall stability indices suggesting that Chauncey Creek is the most stable near the model boundaries and least stable one-third of the way down the creek. This region corresponds to the top of a sediment link, and in the absence of sediment loads from tributaries, the model appears to be smoothing out irregularities.

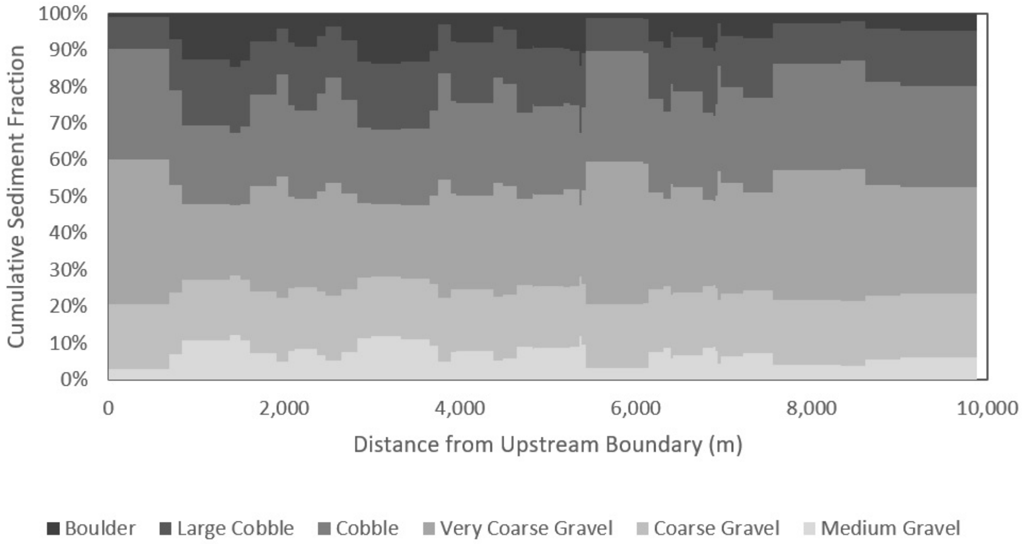

Figure 4-14: Initial surficial grain size distribution

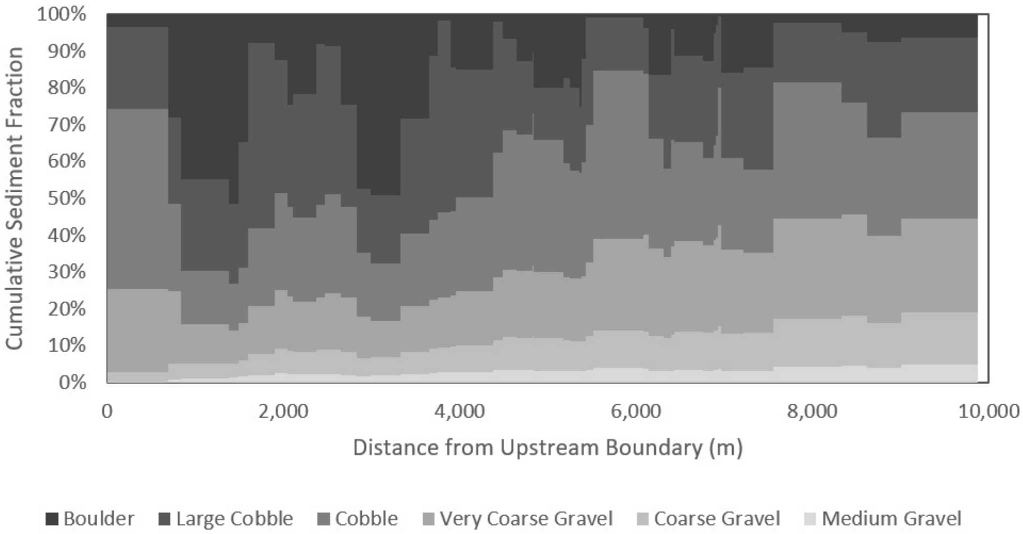

Figure 4-15: Final grain size distribution in the active layer for the Existing Scenario

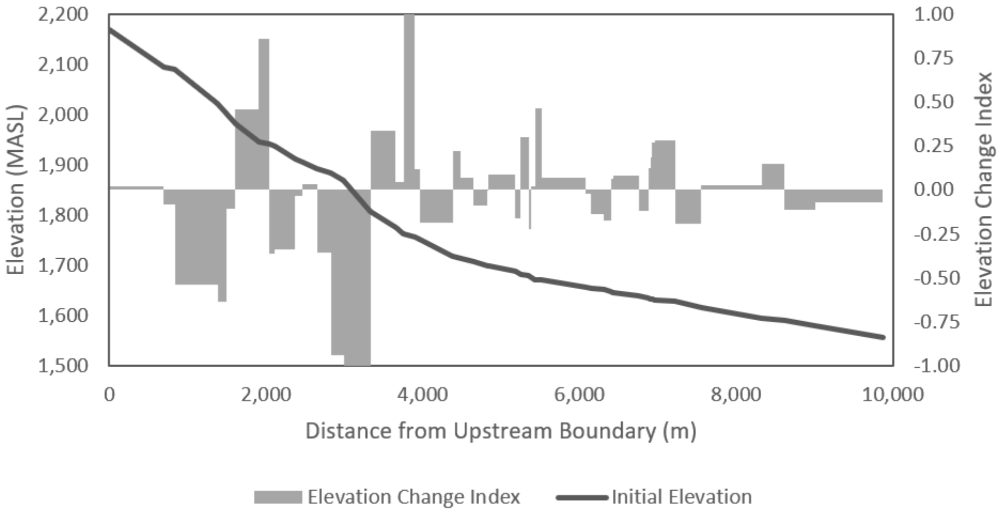

Figure 4-16: Elevation change index for the Existing Scenario

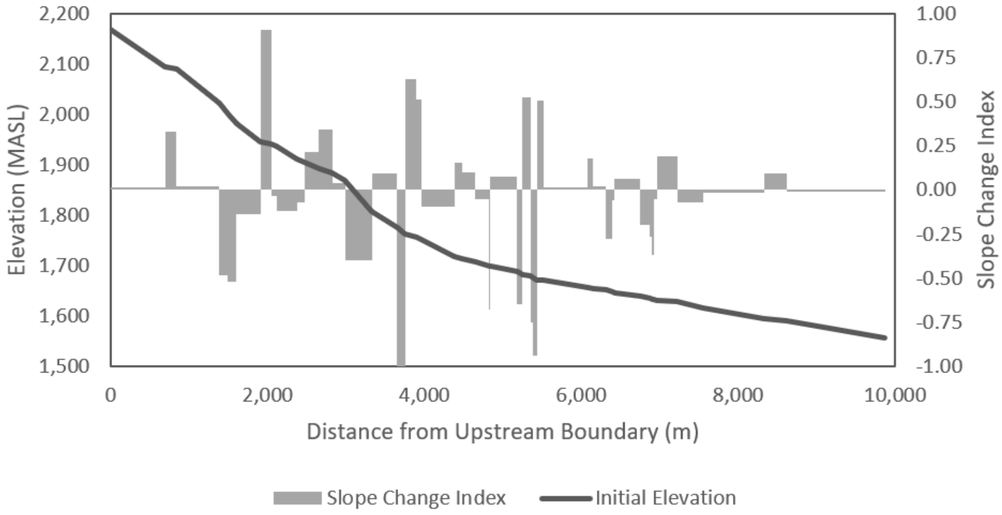

Figure 4-17: Slope change index for the Existing Scenario

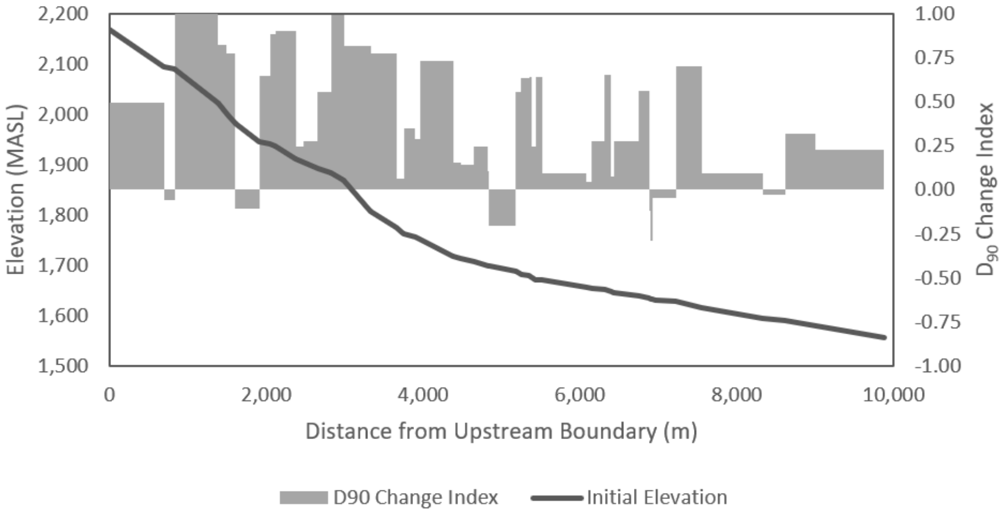

Figure 4-18: Sediment size change index for the Existing Scenario

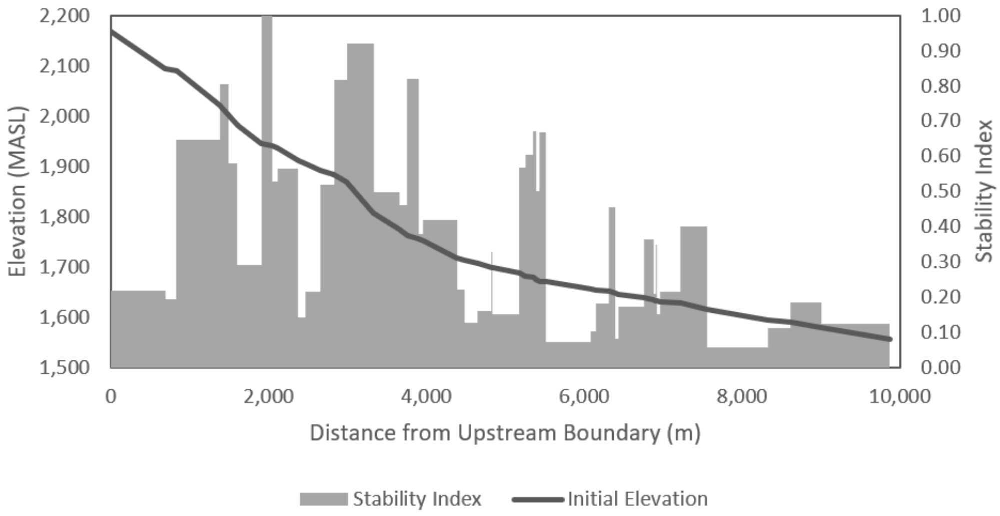

Figure 4-19: Overall stability index for the Existing Scenario

4.3.5 Hydrologic Forcing Scenarios

Alternate Flow Scenario

Floods for the Alternate Scenario with yearly return periods from 2 years to 20 years were approximately 5% greater than the Existing Scenario, but the peak flow was 36% greater, and there were 50% more days that exceeded a flow of 2 m^3/s at the outlet of the nearby catchment. This averages to approximately 20% increase in flow compared to the Existing Scenario. The result of the increase was most noticeable in the change to elevation in the upstream half of Chauncey Creek. The steep reaches that were simulated to decrease in elevation experienced the most significant change to elevation. The trend in changes to slope was maintained for both simulations, but slope for the alternate scenario had progressed further in becoming more smooth. The coarsening trend continued, and more fine material was transported out of the system. The change to stability indices showed that most reaches had a decrease in relative stability.

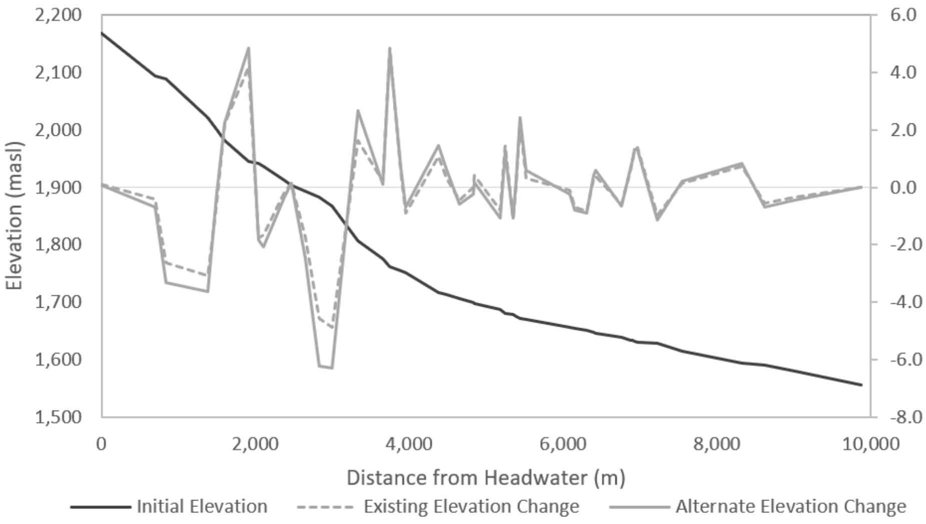

Figure 4-20: Elevation changes for the Alternate Scenario compared to the Existing Scenario

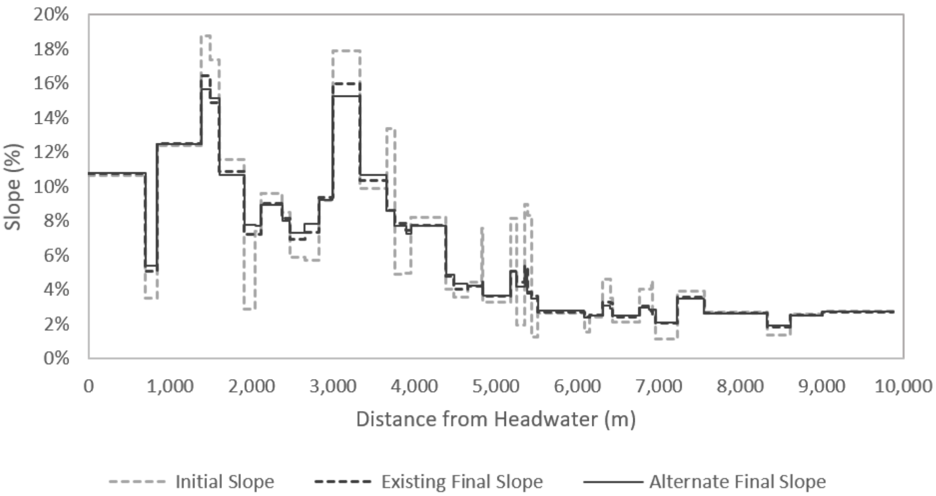

Figure 4-21: Slope change for the Alternate Scenario compared to the Existing Scenario

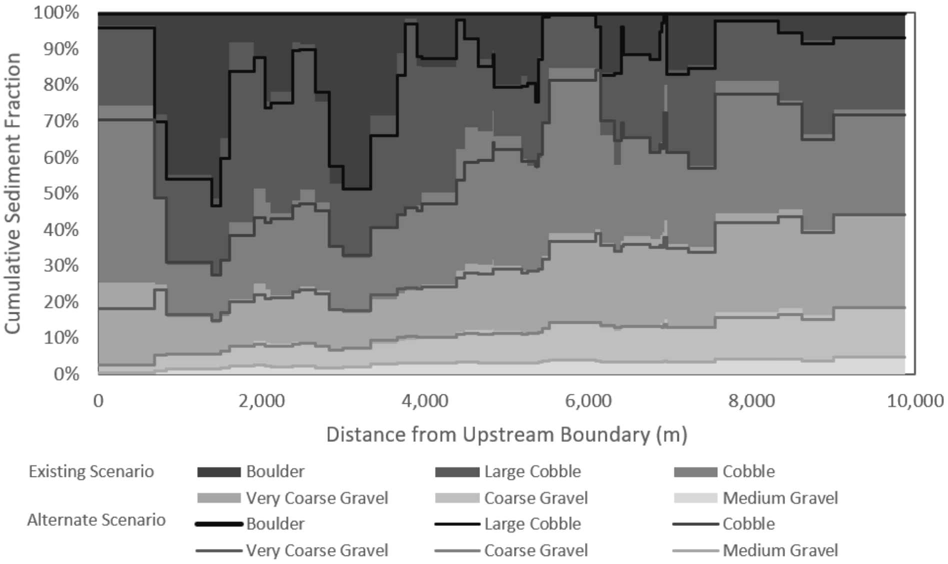

Figure 4-22: Final grain size distribution in the active layer for the Alternate Scenario compared to the Existing Scenario

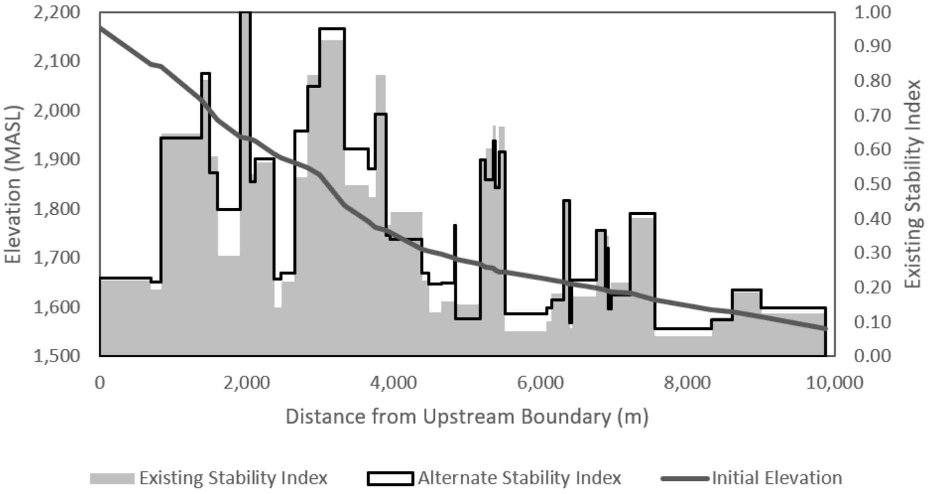

Figure 4-23: Overall stability index for the Alternate Scenario compared to the Existing Scenario

Increased Flow Scenario

The Increased Scenario was similar to the Alternate Scenario in that the flows were greater than the Existing Scenario. The 2-, 5-, and 20-year floods were higher than both the Existing and Alternate Scenarios, but the average flow and 50-year flood was less than the Alternate Scenario. The relative change compared to the Existing Scenario is very similar as the Alternate Scenario, but the extent of the change is between the Existing and Alternate Scenarios.

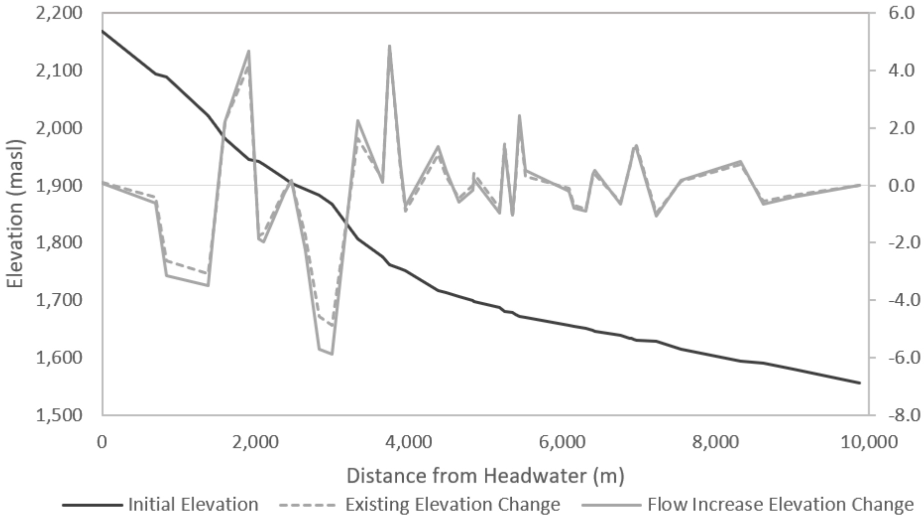

Figure 4-24: Elevation changes for the Increased Scenario compared to the Existing Scenario

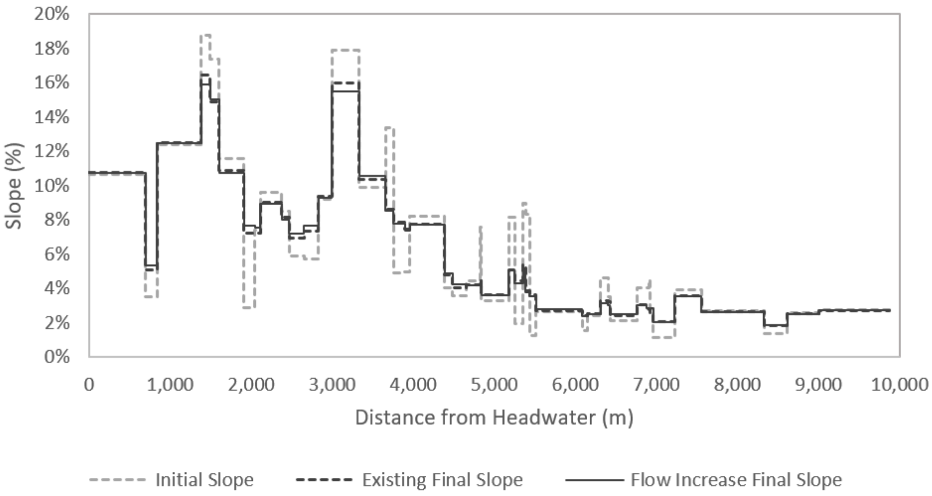

Figure 4-25: Slope change for the Increased Scenario compared to the Existing Scenario

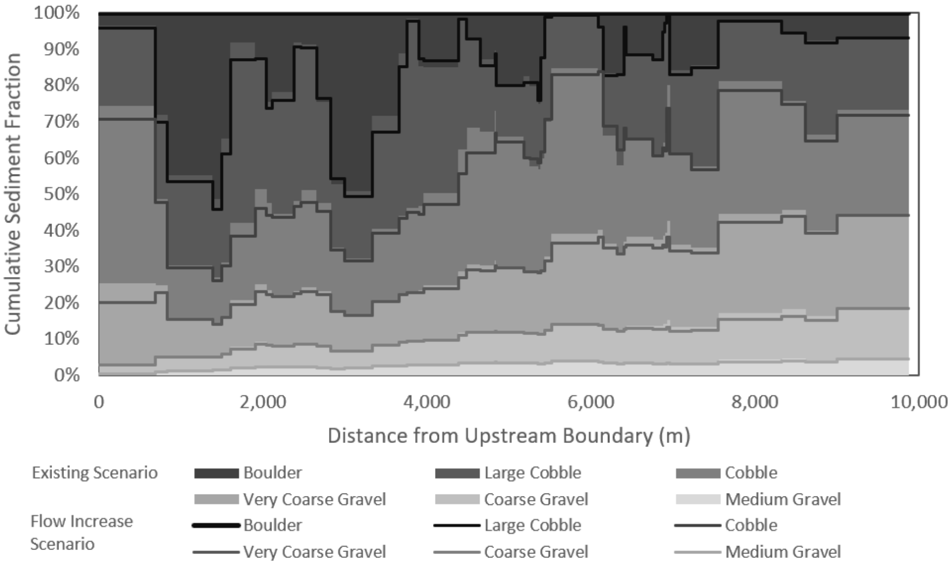

Figure 4-26: Final grain size distribution in the active layer for the Increased Scenario compared to the Existing Scenario

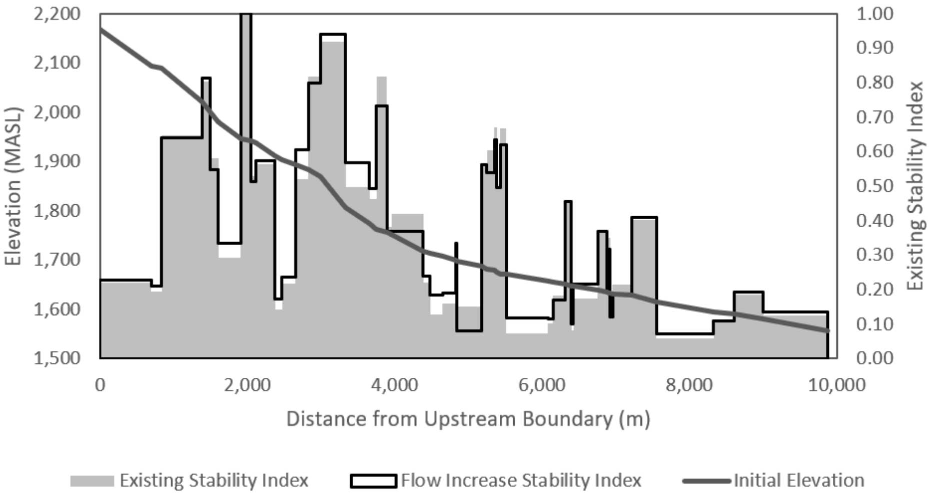

Figure 4-27: Overall stability index for the Increased Scenario compared to the Existing Scenario

Extended Flow Scenario

The Extended Scenario includes flows from both the Existing Scenario and Alternate Scenario. Despite the time series being twice the length, changes in elevation do not increase by such an extent. The change in elevation ranges from 0% to 50% greater, but and one reach that was predicted to increase in elevation for the Existing Scenario was predicted decrease in elevation for the Extended Scenario. The smoothing and coarsening trends predicted for changes to slope and GSD continued, but there were a couple reaches that were predicted to have an increase in proportion of cobbles or large cobbles relative to the boulders. The relative changes in stability between the Existing and Alternate Scenarios were more pronounced for the Extended Scenario.

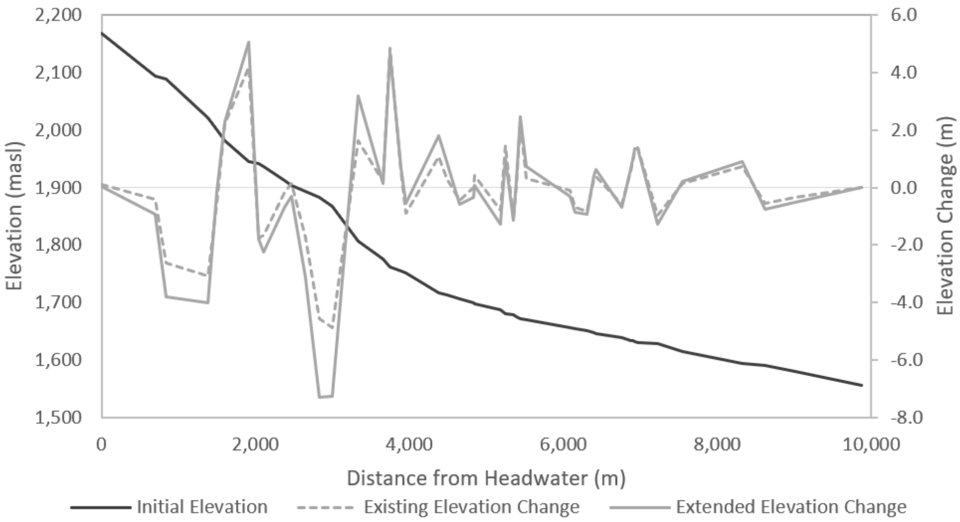

Figure 4-28: Elevation changes for the Extended Scenario compared to the Existing Scenario

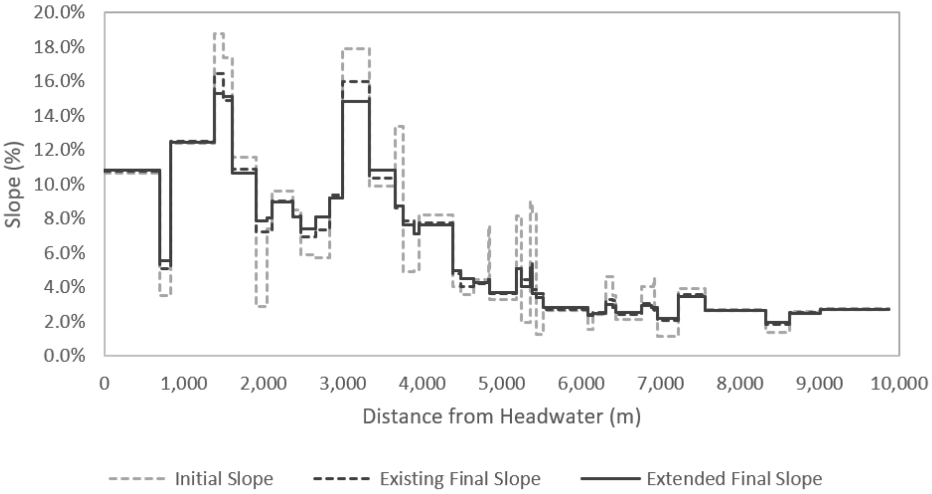

Figure 4-29: Slope change for the Extended Scenario compared to the Existing Scenario

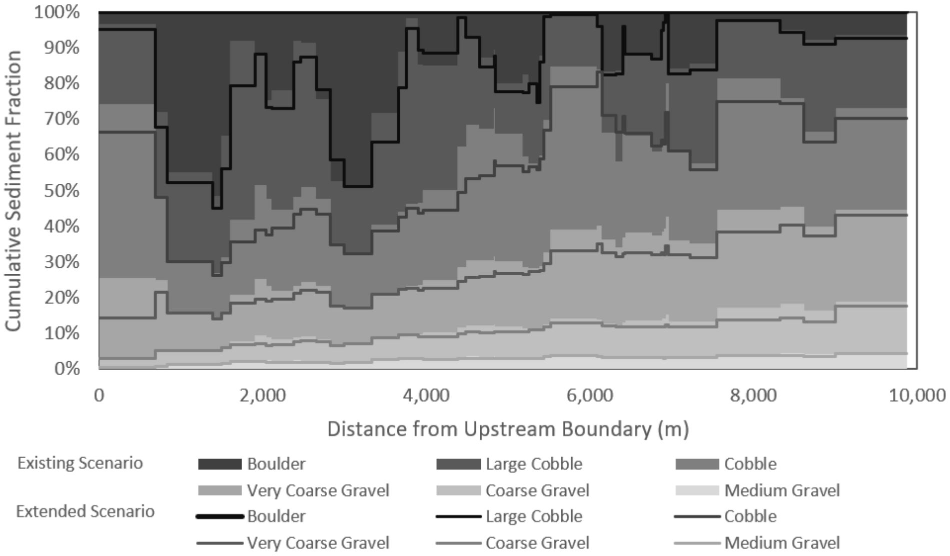

Figure 4-30: Final grain size distribution in the active layer for the Extended Scenario compared to the Existing Scenario

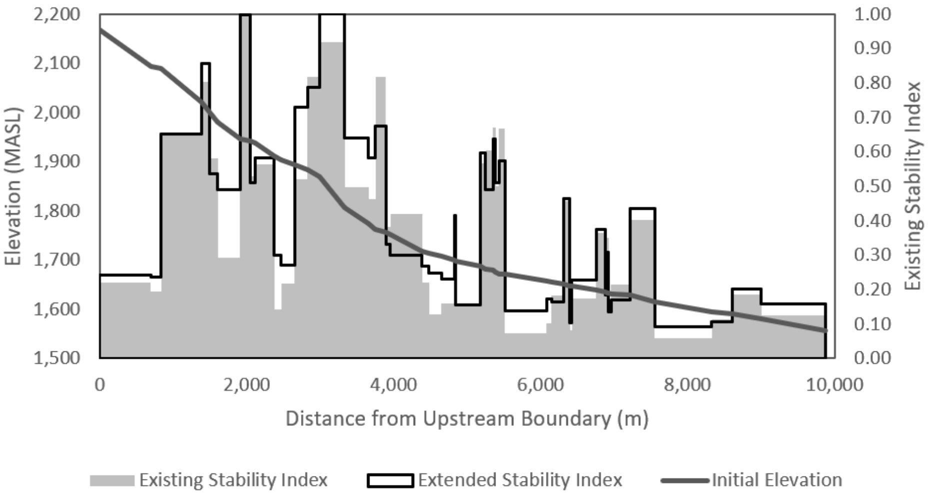

Figure 4-31: Overall stability index for the Extended Scenario compared to the Existing Scenario

Looped Flow Scenario

The Looped Scenario simulates a time period greater than 600 years of flows and some reaches that were relatively stable and were not predicted to change in elevation for any of the previous hydrologic scenarios were predicted to decrease in elevation. The two reaches that are just downstream of convex profiles and near the upstream boundaries of sediment links were predicted to experience the greatest change in elevation. The reaches in the downstream 5 km were predicted to maintain similar elevations despite the longer time series. The trend in slope continued in a smooth direction and the steepest reach decreased from 19% to 13%. The coarsening trend continued and the proportion of medium and coarse gravel ranged from 4% to 10% except for in the reach at the downstream boundary. There were two reaches that were simulated to have an increase in the proportion of cobbles and there were two reaches that were predicted to no longer contain boulders in the active layer. Changes to stability indices varied and the reach downstream of the convex slope 3 km from the upstream boundary of was predicted to be the least stable reach. Again, this corresponds to the top of a sediment link where high volumes of sediment would be expected to enter Chauncey Creek.

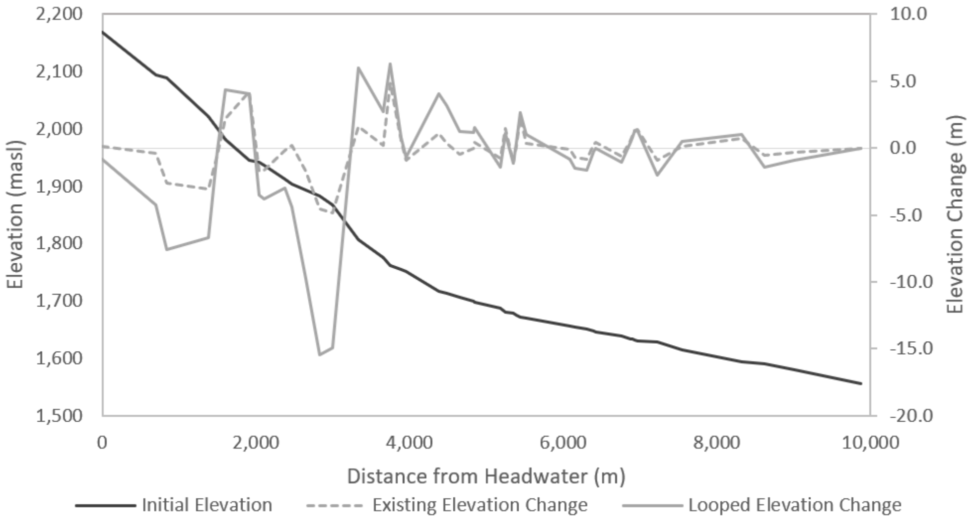

Figure 4-32: Elevation changes for the Looped Scenario compared to the Existing Scenario

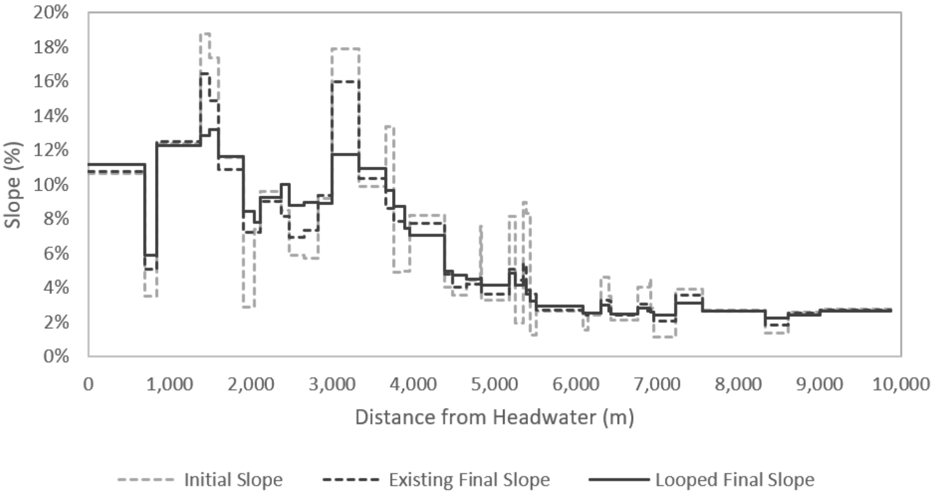

Figure 4-33: Slope change for the Looped Scenario compared to the the Existing Scenario

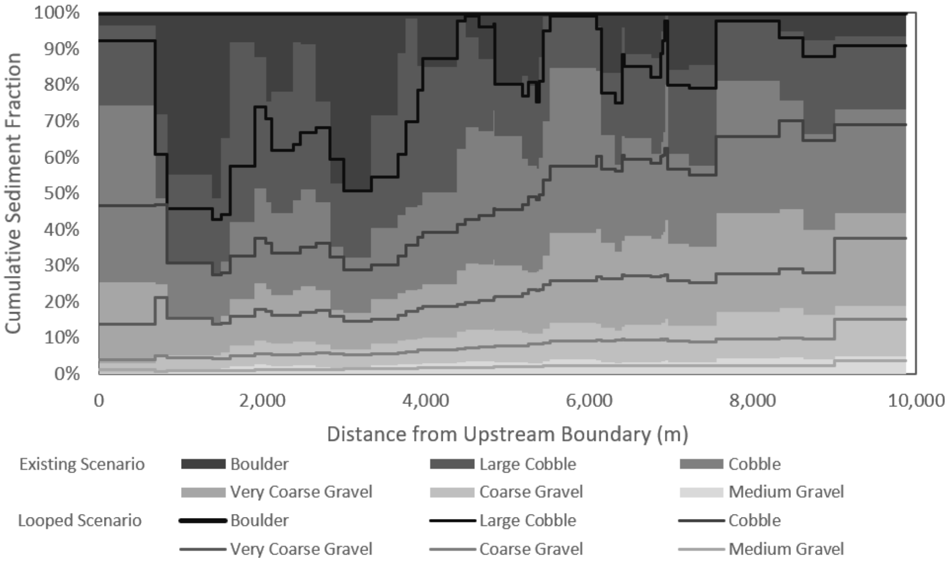

Figure 4-34: Final grain size distribution in the active layer for the Looped Scenario compared to the Existing Scenario

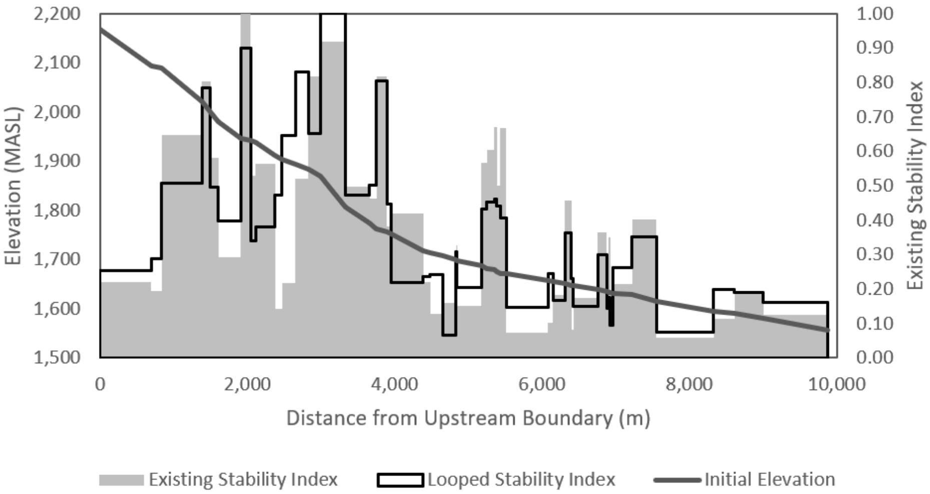

Figure 4-35: Overall stability index for the Looped Scenario compared to the Existing Scenario

4.3.6 Channel Geomorphology Scenarios

Narrow Scenario

The Narrow Scenario was very similar to the Existing Scenario and the width in one 28 m reach was adjusted. Subtle changes to were simulated in elevation, slope, and GSD at the adjusted reach, but the change was not observable in results for reaches that were not immediately adjacent to it. The reach immediately downstream of the adjusted reach was predicted to increase in elevation and be less stable as a result of the narrow condition.

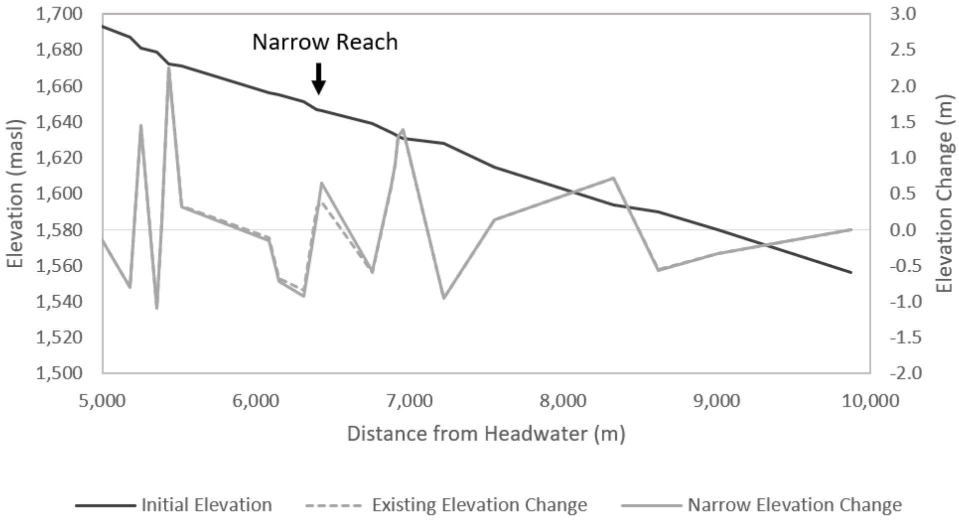

Figure 4-36: Elevation changes for the Narrow Scenario compared to the Existing Scenario

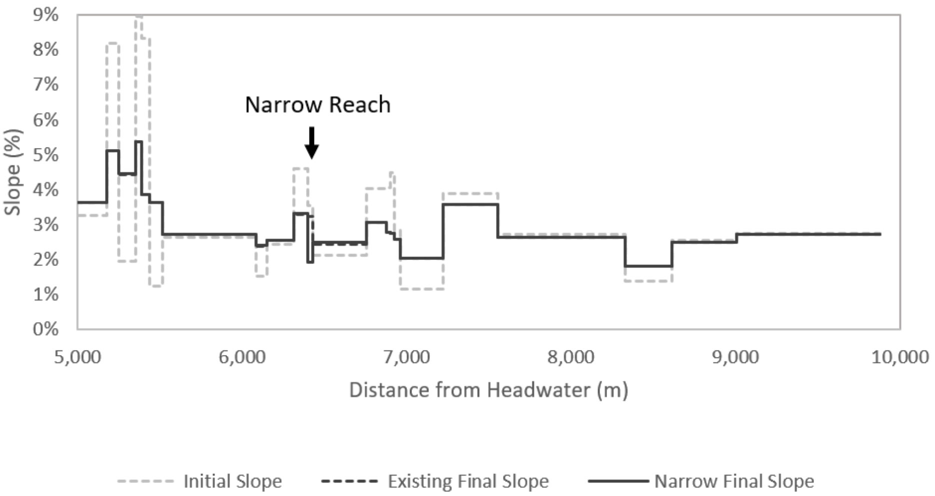

Figure 4-37: Slope change for the Narrow Scenario compared to the Existing Scenario

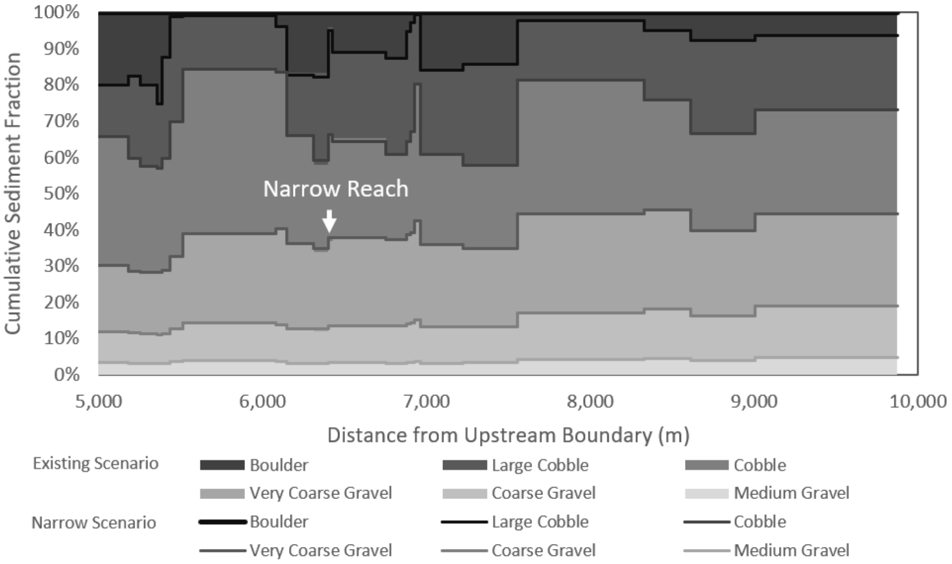

Figure 4-38: Final grain size distribution in the active layer for the Narrow Scenario compared to the Existing Scenario

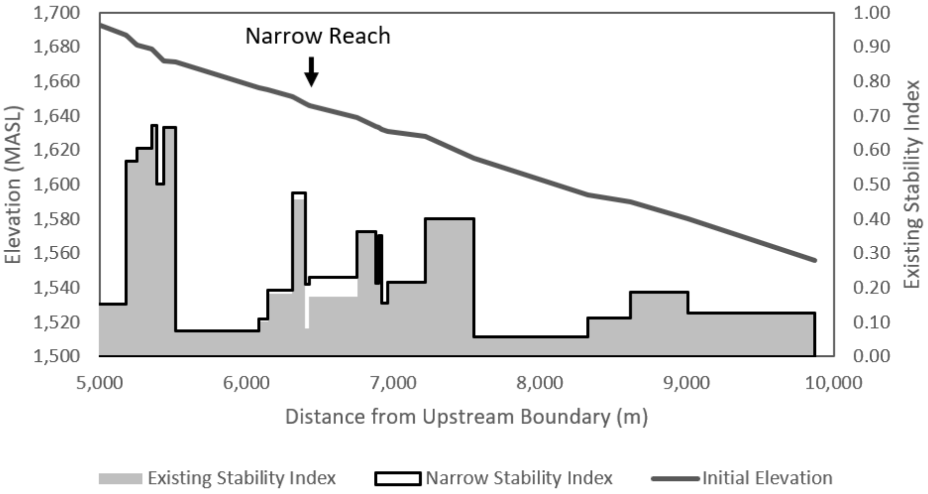

Figure 4-39: Overall stability index for the Narrow Scenario compared to the Existing Scenario

Wide Scenario

The Wide Scenario included one reach that was adjusted, but the change resulted in different results further downstream than for the Narrow Scenario. The change was applied to a reach 6.5 km down from the upstream boundary and was noticeable in every reach downstream of it. The reach that was widened was predicted to have a greater increase to elevation implying that less sediment is being transported out of the reach. Reaches immediately upstream were predicted to not decrease in GSD to as great of an extent as in the Existing Scenario, and the reaches downstream were predicted to have smaller proportions of gravel. The stability was similar to the Existing Scenario and only minor changes were observed in the downstream section of the creek.

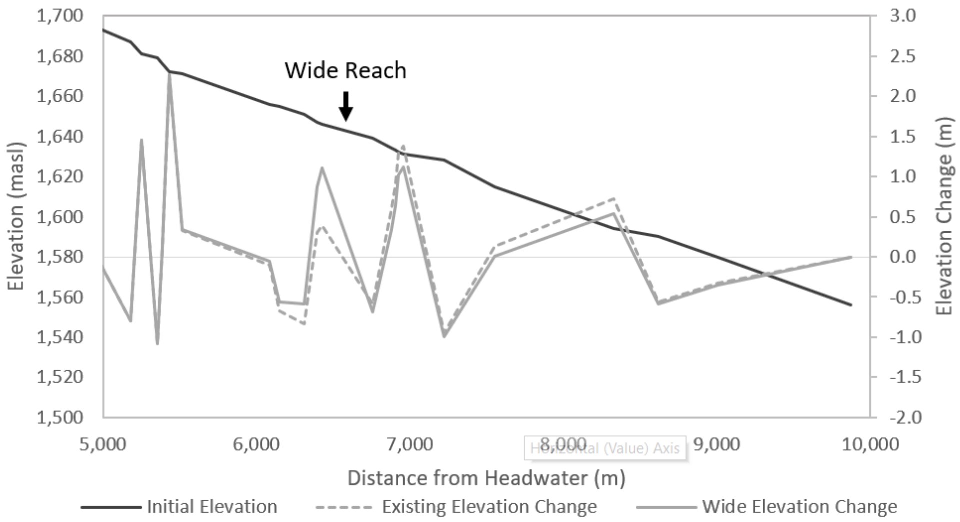

Figure 4-40: Elevation changes for the Wide Scenario compared to the Existing Scenario

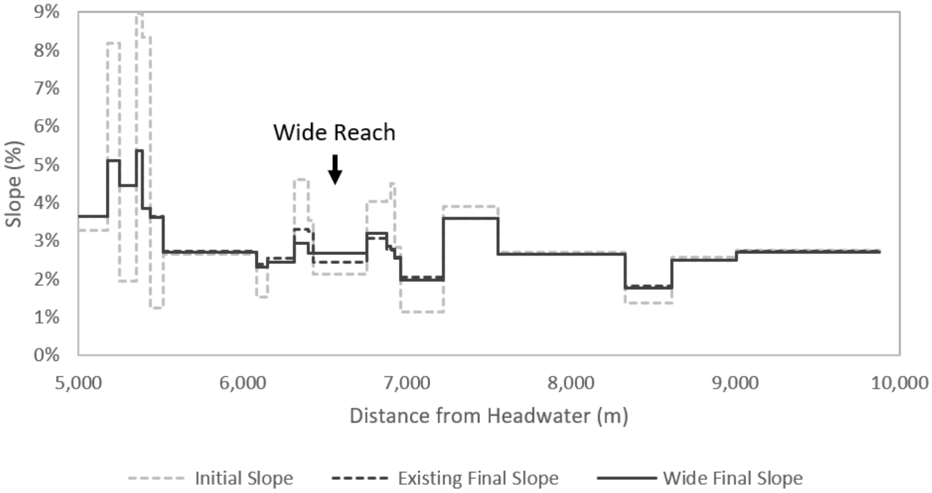

Figure 4-41: Slope change for the Wide Scenario compared to the Existing Scenario

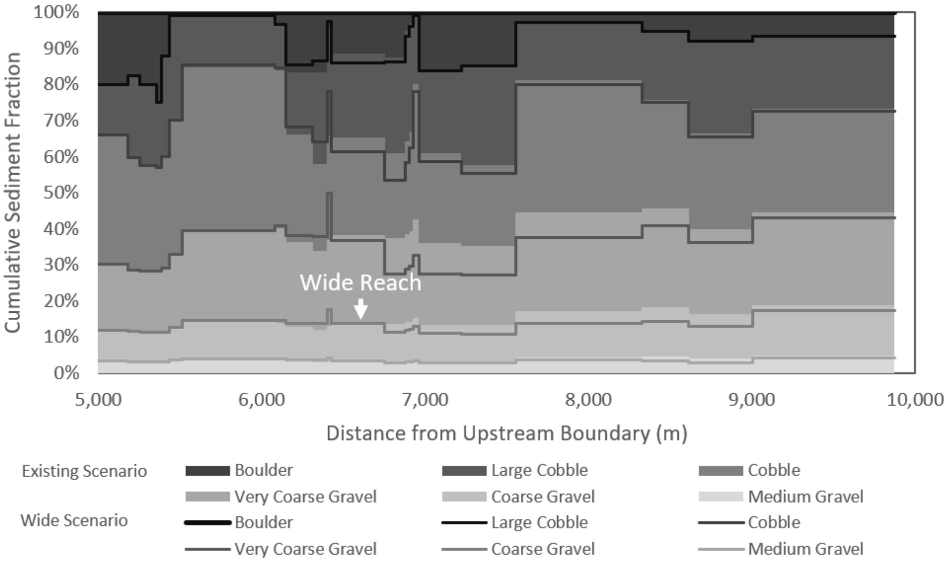

Figure 4-42: Final grain size distribution in the active layer for the Wide Scenario compared to the Existing Scenario

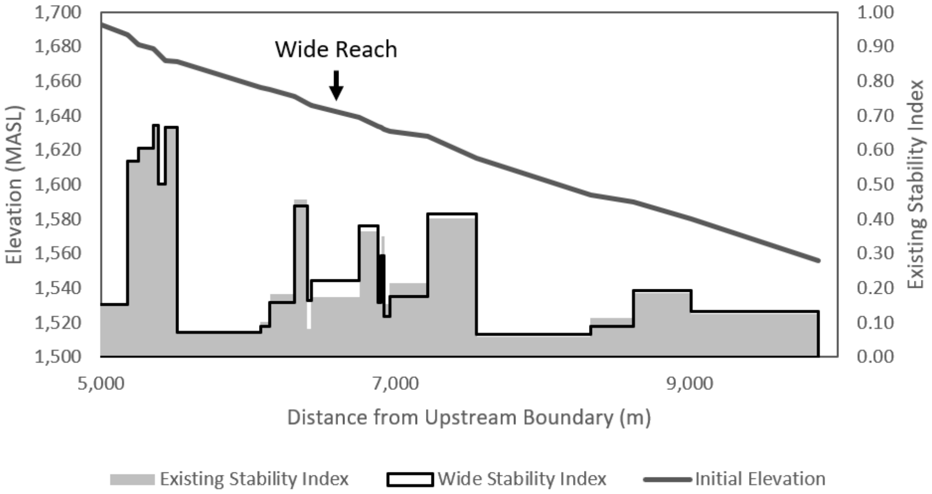

Figure 4-43: Overall stability index for the Wide Scenario compared to the Existing Scenario

4.4 Modelling Discussion

4.4.1 ASIM Performance

A modelling framework that uses 1-D sediment transport principals relating shear stress to bedload transport rates was developed and called ASIM. The objective was to utilize channel properties that can be quickly acquired in the field with the use of UAVs and readily available spatial data to characterize channel stability. ASIM was linked to outputs from software such as FAST and Raven so that it can be directly linked with other deliverables for environmental consulting projects. The continuity of mass in ASIM was confirmed for total sediment, but there was an imbalance within each size class. The functionality of ASIM was compared to a model made available by G. Parker (2004) and was shown to perform similarly for a regular channel with a constant slope, flow, and width. The differences that were identified are from known changes to the boundary conditions and slope calculations and were the result of adjustments made to improve model stability in ASIM. The discretization method in ASIM more closely resembles RubarBE (El Kadi Abderrezzak et al., 2008; El Kadi Abderrezzak & Paquier, 2009) where the hydraulic and sediment transport equations are calculated in cells that are offset from one another.

The results from the Existing Scenario were used to assess the functionality of ASIM for a mountain catchment. In general, the simulation for Chauncey Creek performed as expected, and geomorphological processes follow relationships shown in long-profile evolution models (Wickert & Schildgen, 2019). Reaches located in regions with a concave-up longitudinal profile are predicted to decrease in elevation, and the opposite occurs in convex-up reaches. These elevation changes result in a smoother longitudinal slope profile, which is similar to other 1D model predictions for river networks (Lewicki et al., 2007), for knick-point propagation (S. Schumm & Harvey, 2008), and dam surface erosion (Wu & Wang, 2008). The trend toward a more coarse GSD was also expected because of what is known from graded relationships (Equation 2.1) (Lane, 1955). The sediment loading simulated for Chauncey Creek did not include the majority of sources that would be expected in the field, and a graded river could respond to a reduction in sediment load through a decrease in slope or sediment calibre. An increase in sediment calibre has been shown through flume studies and field investigations (Lisle et al., 1993; Papanicolaou et al., 2004).

The stability results indicate that the steep reaches would be the least stable and have the most substantial change in elevation, slope, and D_{90}. This result initially makes sense because the shear stress and shear velocity increase with slope and are the primary variables used to calculate sediment transport rates. However, these results might be misleading. Bathurst et al. (1987) and Yager et al. (2007) have shown that conventional resistance equations used by Wilcock and Crowe (2003) lead to an over prediction of sediment transport in steep reaches. One correction used for steep channels is to reduce the slope before calculating the shear stress, whereby the slope reduction would account for energy lost due to form roughness (Chiari & Rickenmann, 2011; Nitsche et al., 2011; Schneider et al., 2016). An alternative approach is to calculate critical Shields stress with an equation that accounts for slope and shallow flow such as one suggested by Lamb et al. (2008) or Recking (2009). However, Prancevic and Lamb (2015) indicated that there is no universal trend that relates channel slope, to critical Shields stress, so more research would be required before applying this approach.

There was no suitable data set to calibrate and validate ASIM for Chauncey Creek adequately, so there were some processes that would be expected to occur in the field but were not predicted. The smaller particles were expected to be transported through the system quickly, but this would generally be balanced with a similar supply of small particles entering the river. The lack of sediment entering Chauncey Creek from hill slopes and tributaries in ASIM resulted in there being an insufficient supply of gravel to balance the system. The resulting GSDs no longer resembled a Gaussian distribution after the simulation, and in some situations, half of the sediment was classified as boulders. Without sufficient sediment supply, no equilibrium could be established unless the active layer became so coarse to where sediment transport no longer occurs.

The hydrologic comparisons indicate that there is a common long-term trend. More hydrologic scenarios should be simulated, but from what the Existing, Alternate, and Increased Scenarios show is that peak flow, and average flow are more reliable indicators of high sediment transport rates compared to more common floods.The Looped Scenario shows that the processes occur over a very long term. The slope continues to smooth out, and there is still a significant decrease in elevation change predicted in the long term.

However, it does not appear that an equilibrium condition would be achieved unless the Looped Scenario is extended further into the future.

The geometric comparisons indicate that increasing the width of a reach has a broader effect to changes in elevation and GSDs downstream than making a channel more narrow. This could be because a narrow reach will transfer more sediment downstream, but it will often build up in the next reach because mountain channels are generally transport-limited. The sediment transport thresholds should also be considered when evaluating whether or not narrowing or widening a reach will cause significant changes. Sediment transport is not a linear function, so a change to the channel width could lead to different results depending on the relative values of average shear stress and critical shear that exist before the change.

4.4.2 Model Assumptions and Future Improvements

There were many assumptions made in ASIM. Some assumptions were made out of necessity to simplify the river network and some of the processes with the goal of limiting computational and high-resolution data requirements. Other assumptions were made because of time constraints and should be adjusted before ASIM is fully applied. Assumptions in ASIM that are expected to be maintained through future updates include the following:

- River channels do not bifurcate. The processes in ASIM would not be suitable for rivers that split into multiple channels for extended lengths.
- Seepages and surface water accretion are assumed to be zero along each reach. Channel flow increases at nodes which correspond to confluences with tributaries.
- Channel width is calculated from the catchment area using a power function that was calibrated from field measurements. This assumption was made to reduce the number of field measurements that would be required to run ASIM.
- Abrasion and breakage of particles is not considered.
- Channel width does not vary over time. Erosion of river banks is highly variable due to varied stability from soil cohesion and vegetation and the process is beyond the scope of ASIM.

- The channel does not migrate. Rivers naturally meander, but this process would be difficult to parameterize and is also beyond the scope of ASIM.
- Uplift and hillslope process are not considered. ASIM was designed to assess relative risk and does not prediction future conditions, so these processes were included.

Assumptions in ASIM that should be reviewed and possibly adjusted include the following:

- Flow is linearly related to catchment area. This assumption has been shown to be applicable in the field for annual peak flows (Wohl et al., 2004) but this is an extremely simplified approach. A power function relating flow to catchment area would be more widely applicable, and if time allows, a Raven model that breaks the catchment down into subcatchments could provide more information about the spatial variability in flows.
- Channels are assumed to be rectangular and wide ($w/d > 20$). These assumptions simplify the hydraulic and sediment transport equations, but channels in mountain regions are rarely wide and rectangular. Removing these assumptions would require an assumption to be made about the spatial variability for width-to-depth ratios and channel shape so that the hydraulic radius could be calculated.
- There is no bedrock layer. The depth of bedrock is unknown in Chauncey Creek, but it would be expected to be reached for the depths of degradation that the Looped Scenario is predicting. The existence of bedrock would prevent the channel from degrading after all of the substrate is transported out of a reach, but this was not simulated. ASIM does have a lower boundary of sediment and will not continue if this boundary is reached, but it could be possible to include a process for allowing sediment to be transported across a reach with exposed bedrock.
- Wilcock and Crowe's (2003) has been applied to all channel gradients despite it being most applicable to shallower slopes (<3%). This assumption can be relaxed by calculating an adjusted slope following the approach of Schneider et al. (2016) as long as the hydraulic radius is calculated.

Other improvements that could be made, but that are not linked to existing assumptions include the following:

- Continuity of individual grain sizes should be investigated further to identify the source of discontinuity.
- Additional sediment loading should be included. ASIM is set up to allow for side tributaries to be included which would provide a source for sediment to flow into the main channel. Point sources at locations with steep hillslopes and alluvial fans could be added. More research into sediment generation from debris flows and erosional processes would be required and visual representation for side channels should be developed alongside ASIM.
- The selection of different sediment transport equations could be incorporated within ASIM. It would be possible to add other sediment transport equations that use shear stress (G. Parker, 1990) or stream power (C. Parker et al., 2011). No model is perfect, so this addition would allow for a range of equations to be used and compared.
- The model should be calibrated and validated. A longer set of field data would be required for this step, but it is a crucial process before ASIM can be trusted and applied in industry.
- More simulations should be run to evaluate the significance of each input. Simulations with a variety of initial GSDs should also be included to understand how sensitive the model is to surface conditions.

Chapter 5

Conclusions

This thesis describes the work that was completed to develop a field program and modelling framework that can be used in series to better understand sediment transport and channel stability in remote, mountainous regions. The results of this thesis could be used to better characterize risk to infrastructure that intersects river networks that would otherwise be unidentified.

The field program confirmed that GSD and geometry data can be collected quickly in places with limited access or elevated health and safety risks Data from a UAV was used to and shown to be within an accuracy of 1 - 5% without georeferenced control markers and three passes of survey locations were sufficient to collect high resolution photos and data 3-D models. The comparisons between Wolman pebble counts, paint-and-pick, and photosieving showed that photos from UAVs can be analyzed with BASEGRAIN to acquire GSDs within 8% Ψ. Chauncey Creek was used as the river catchment to test the field program and a least three sediment links were identified from visual inspection of loading sources, channel slope, and grain size. The channel properties in Chauncey Creek appear to follow reasonable relationships relative to a stream power index. The surface particle distributions were found to match Gaussian distributions

The model framework (ASIM) was shown to perform similarly to a model developed by G. Parker (2004) and total continuity of mass was maintained. A discontinuity in the calculations for individual grain sizes was found that should be investigated further. The

Existing Scenario for Chauncey Creek showed that the slope, elevation, and dominant grain size in the steepest sections would change to the greatest degree. Different flow scenarios suggest that the model approaches a common future, but the extent and speed of the changes depend on the magnitude and recurrence of floods. Different geometrical scenarios show that widening a channel could have more noticeable impacts downstream than narrowing a channel, but this conclusion likely will depend on sediment loading and channel geometry in neighbouring reaches.

References

Aberle, J., & Nikora, V. (2006). Statistical properties of armored gravel bed surfaces. *Water Resources Research*, *42*(11), 1–11. doi: 10.1029/2005WR004674

Adams, J. (1979). Gravel size analysis from photographs. *Journal of the Hydraulics Division*, *105*(10), 1247–1255.

Agriculture and Agri-Food Canada. (2013). *Surficial geology by ecoregion.* Retrieved from https://open.canada.ca/data/en/dataset/a88f1437-f93f-42e8-9b44-6cdc2213a172

Alber, A., & Piégay, H. (2011). Spatial disaggregation and aggregation procedures for characterizing fluvial features at the network-scale: application to the Rhône basin (France). *Geomorphology*, *125*(3), 343–360. doi: 10.1016/j.geomorph.2010.09.009

An, C., Cui, Y., Fu, X., & Parker, G. (2017). Gravel-bed river evolution in earthquake-prone regions subject to cycled hydrographs and repeated sediment pulses. *Earth Surface Processes and Landforms*, *42*(14), 2426–2438. doi: 10.1002/esp.4195

Andrews, E. D. (1983). Entrainment of gravel from naturally sorted riverbed material. *Geological Society of America Bulletin*, *94*(10), 1225–1231. doi: 10.1130/0016-7606(1983)94⟨1225:EOGFNS⟩2.0.CO;2

Arnold, J. G., Srinivasan, R., Muttiah, R. S., & Williams, J. R. (1998). Large area hydrologic modeling and assessment part 1: Model development. *Journal of the American Water Resources Association*, *34*(1), 73–89.

Azzalini, A. (1985). A class of distributions which includes the normal ones. *Scandinavian Journal of Statistics*, *12*(2), 171–178.

Azzalini, A. (2005). The skew-normal distribution and related multivariate families. *Scandinavian Journal of Statistics*, *32*(2), 159–188. doi: 10.1111/j.1467-9469.2005.00426.x

Bagnold, R. A. (1966). An approach to the sediment transport problem from general physics. *USGS Professional Paper*, *442*(1), 42. doi: 10.1017/S0016756800049074

Bagnold, R. A. (1977). Bed load transport by natural rivers. *Water Resources Research*, *13*(2), 303–312. doi: 10.1029/WR013i002p00303

Bagnold, R. A. (1980). An empirical correlation of bedload transport rates in flumes and natural rivers. *Proceedings of the Royal Society of London. Series A, Mathematical and Physical Sciences*, *372*(1751), 453–473.

Bathurst, J. C., Graf, W., & Cao, H. (1987). Bed load discharge equation in mountain rivers. In C. Thorne, J. Bathurst, & R. Hey (Eds.), *Sediment transport in gravel-bed rivers* (pp. 453–477). New York: John Wiley.

Belletti, B., Rinaldi, M., Buijse, A. D., Gurnell, A. M., & Mosselman, E. (2015). A review of assessment methods for river hydromorphology. *Environmental Earth Sciences*, *73*(5), 2079–2100. doi: 10.1007/s12665-014-3558-1

Benda, L., & Dunne, T. (1997). Stochastic forcing of sediment supply to channel networks from landsliding and debris flow. *Water Resources Research*, *33*(12), 2849–2863. doi: 10.1029/97WR02388

Bevan, V., MacVicar, B., Chapuis, M., Ghunowa, K., Papangelakis, E., Parish, J., & Snodgrass, W. (2018). Enlargement and evolution of a semi-alluvial creek in response to urbanization. *Earth Surface Processes and Landforms*, *43*(11), 2295–2312. doi: 10.1002/esp.4391

Brabec, E., Schulte, S., & Richards, P. L. (2002). Impervious surfaces and water quality: A review of current literature and its implications for watershed planning. *Journal of Planning Literature*, *16*(4), 499–514. doi: 10.1177/088541202400903563

Bray, D. I. (1982). Regime equations for gravel bed rivers. In R. D. Hey, J. C. Bathurst, & C. R. Thorne (Eds.), *Gravel bed rivers* (pp. 242–245). New York: John Wiley and Sons.

Buffington, J. M., & Montgomery, D. R. (1997). A systematic analysis of eight decades of incipient motion studies, with special reference to gravel-bedded rivers. *Water Resources Research*, *33*(8), 1993–2029. doi: 10.1029/96WR03190

Bunte, K., & Abt, S. R. (2001). *Sampling surface and subsurface particle-size distributions in wadable gravel- and cobble-bed streams for analyses in sediment transport, hydraulics, and streambed monitoring* (Tech. Rep.).

Bush, E., Lemmen, D., & Editors. (2019). *Canada's changing climate report; Government of Canada* (E. Bush & D. Lemmen, Eds.). Ottawa, ON. Retrieved from http://www.changingclimate.ca/CCCR2019

Camenen, B., Béraud, C., Le Coz, J., & Paquier, A. (2018). 1D morphodynamic modelling using a simplified grain size description. *Journal of Hydraulic Research*, *56*(2), 168–180. doi: 10.1080/00221686.2017.1312575

Cao, Z., Pender, G., Wallis, S., & Carling, P. (2004). Computational dam-break hydraulics over erodible sediment bed. *Journal of Hydraulic Engineering*, *130*, 689–703. doi: 10.1061/(ASCE)0733-9429(2004)130

Carbonneau, P. E., Bizzi, S., & Marchetti, G. (2018). Robotic photosieving from low-cost multirotor sUAS: A proof-of-concept. *Earth Surface Processes and Landforms*, *43*(5), 1160–1166. doi: 10.1002/esp.4298

Cazorzi, F., Fontana, G. D., Luca, A. D., Sofia, G., & Tarolli, P. (2013). Drainage network detection and assessment of network storage capacity in agrarian landscape. *Hydrological Processes*, *27*(4), 541–553. doi: 10.1002/hyp.9224

Central Intelligence Agency. (2019). *The world factbook.* Washington DC. Retrieved from https://www.cia.gov/library/publications/resources/

the-world-factbook/index.html

Chansen, H. (1999). *The hydraulics of open channel flow: An introduction.* London, UK: Edward Arnold.

Charlton, R. (2007). *Fundamentals of fluvial geomorphology.* New York, NY: Routledge. doi: 10.4324/9780203371084_chapter_8

Chernos, M., Macdonald, R., & Craig, J. (2017). Efficient semi-distributed hydrological modelling workflow for simulating streamflow and characterizing hydrologic processes. *Confluence: Journal of Watershed Science and Management*, *1*(3), 1–13. doi: 10.22230/jwsm.2017v1n1a3

Chiari, M., Friedl, K., & Rickenmann, D. (2010). A one-dimensional bedload transport model for steep slopes. *Journal of Hydraulic Research*, *48*(2), 152–160. doi: 10.1080/00221681003704087

Chiari, M., & Rickenmann, D. (2011). Back-calculation of bedload transport in steep channels with a numerical model. *Earth Surface Processes and Landforms*, *36*(6), 805–815. doi: 10.1002/esp.2108

Church, M. (1992). Channel morphology and typology. In P. Calow & G. E. Petts (Eds.), *The rivers handbook, vol. 1* (p. 526). Blackwell, Oxford.

Church, M., Mclean, D., & Wolcott, J. F. (1987). River bed gravel: Sampling and analysis. In C. Thorne, J. Bathurst, & R. Hey (Eds.), *Sediment transport in gravel-bed rivers* (pp. 43 – 88). Chichester: John Wiley and Sons.

Clapuyt, F., Vanacker, V., & Van Oost, K. (2016). Reproducibility of UAV-based earth topography reconstructions based on structure-from-motion algorithms. *Geomorphology*, *260*, 4–15. doi: 10.1016/j.geomorph.2015.05.011

Cluer, B., & Thorne, C. (2014). A stream evolution model integrating habitat and ecosystem benefits. *River Research and Applications*, *30*, 135–154. doi: 10.1002/rra

Cui, Y., Paola, C., & Parker, G. (1996). Numerical simulation of aggradation and downstream fining. *Journal of Hydraulic Research*, *34*(2), 185–204. doi: 10.1080/00221689609498496

Cui, Y., & Parker, G. (2005). Numerical model of sediment pulses and sediment-supply disturbances in mountain rivers. *Journal of Hydraulic Engineering*, *131*(8), 646–656. doi: 10.1061/(ASCE)0733-9429(2005)131:8(646)

Czech, W., Plesiński, K., Radecki-Pawlik, A., & Radecki-Pawlik, B. (2016). Dominant discharge – an outline of theory and a case study from the Raba river. *Acta Scientiarum Polonorum Formatio Circumiectus*, *15*(2), 41–53. doi: 10.15576/asp.fc.2016.2.41

Detert, M., Kadinski, L., & Weitbrecht, V. (2017). Feasibility tests to airborne gravelometry for prealpine rivers. *River Sedimentation: Proceedings of the 13th Interational Symposium on River Sedimentation*, 1258–1263.

Detert, M., & Weitbrecht, V. (2012). Automatic object detection to analyze the geometry of gravel grains - A free stand-alone tool. *River Flow 2012*, 595–600.

Detert, M., & Weitbrecht, V. (2013). User guide to gravelometric image analysis by basegrain. *Advances in Science and Research*, *ISBN 978-1*(January), 1789–1795.

Dey, S. (1999). Sediment threshold. *Applied Mathematical Modelling*, *23*, 399–417. doi: 10.1007/978-3-642-19062-9_4

Dey, S., & Ali, S. Z. (2019). Bed sediment entrainment by streamflow: State of the science. *Sedimentology*, *66*(5), 1449–1485. doi: 10.1111/sed.12566

DiBiase, R. A., & Whipple, K. X. (2011). The influence of erosion thresholds and runoff variability on the relationships among topography, climate, and erosion rate. *Journal of Geophysical Research: Earth Surface*, *116*(4), 1–17. doi: 10.1029/2011JF002095

Dietrich, W. E., & Dunne, T. (1978). Sediment budget for a small catchment in mountainous terrain. *Zeitschrift fur Geomorphologie*. doi: 10.1130/0091-7613(2001)029

Diplas, P., & Sutherland, A. J. (1988). Sampling techniques for gravel sized sediments. *Journal of Hydraulic Engineering*, *114*(5), 484–501.

Downs, P., & Gregory, K. (2004). *River channel management; Towards sustainable catchment hydrosystems*. London, UK: Hodder Arnold.

Dugdale, S. J., Carbonneau, P. E., & Campbell, D. (2010). Aerial photosieving of exposed gravel bars for the rapid calibration of airborne grain size maps. *Earth Surface Processes and Landforms*, *35*(6), 627–639. doi: 10.1002/esp.1936

Eaton, B. C., & Church, M. (2011). A rational sediment transport scaling relation based on dimensionless stream power. *Earth Surface Processes and Landforms*, *36*(7), 901–910. doi: 10.1002/esp.2120

Einstein, H. A. (1950). *The bed-load function for sediment transportation in open channel flows*. U.S. Dept. of Agriculture,. Retrieved from http://hdl.handle.net/2027/uiug.30112019331690

El Kadi Abderrezzak, K., & Paquier, A. (2009). One-dimensional numerical modeling of sediment transport and bed deformation in open channels. *Water Resources Research*, *45*(5), 1–20. doi: 10.1029/2008WR007134

El Kadi Abderrezzak, K., Paquier, A., & Gay, B. (2008). One-dimensional numerical modelling of dam-break waves over movable beds: Application to experimental and field cases. *Environmental Fluid Mechanics*, *8*(2), 169–198. doi: 10.1007/s10652-008-9056-9

Environment and Climate Change Canada. (2017). *Climate trends and variations bulletin.* Retrieved from https://assets.publishing.service.gov.uk/government/uploads/system/uploads/attachment{_}data/file/674761/FSRAnnual{_}Report{_}2017{_}v1{_}01.pdf

Environment and Climate Change Canada. (2020). *Water level and flow: Frequently*

Asked Questions. Retrieved 2020-01-30, from https://wateroffice.ec.gc.ca/contactus/faq{_}e.html{#}Q11

Exner, F. M. (1925). Über die Wechselwirkung zwischen Wasser und Geschiebe in Flüssen (in German). *Sitz. Acad. Wiss. Wien Math. Naturwiss.*, *2a*(134), 165–203.

Ferencevic, M. V., & Ashmore, P. (2012). Creating and evaluating digital elevation model-based stream-power map as a stream assessment tool. *River Research and Applications*, *28*, 1394–1416.

Ferguson, R. I. (1994). Critical discharge for entrainment of poorly sorted gravel. *Earth Surface Processes and Landforms*, *19*(2), 179–186. doi: 10.1002/esp.3290190208

Ferguson, R. I. (2005). Estimating critical stream power for bedload transport calculations in gravel-bed rivers. *Geomorphology*, *70*(1-2), 33–41. doi: 10.1016/j.geomorph.2005.03.009

Ferguson, R. I. (2012). River channel slope, flow resistance, and gravel entrainment thresholds. *Water Resources Research*, *48*(5), 1–13. doi: 10.1029/2011WR010850

Ferrer-Boix, C., & Hassan, M. A. (2014). Influence of the sediment supply texture on morphological adjustments in gravel-bed rivers. *Journal of the American Water Resources Association*, *50*(3), 8868–8890. doi: 10.1111/j.1752-1688.1969.tb04897.x

Folk, R. L., & Ward, W. C. (1957). Brazor river bar: A study in the signigicance of grain size parameters. *Journal of Sedimentary Petrology*, *27*(1), 3–26.

García, M. H. (2008a). *Sedimentation engineering - Processes; measurements; modeling; and practice - ASCE manuals and reports on engineering practice (MOP) No. 110.* American Society of Civil Engineers (ASCE). Retrieved from https://app.knovel.com/hotlink/toc/id:kpSEPMMP02/sedimentation-engineering/sedimentation-engineering

García, M. H. (2008b). Sediment transport and morphology. In M. H. García (Ed.), *Sedimentation engineering: Processes, measurements, modeling, and practice* (pp. 21–163). American Society of Civil Engineers.

Gholami, A., Bonakdari, H., Ebtehaj, I., Shaghaghi, S., & Khoshbin, F. (2017). Developing an expert group method of data handling system for predicting the geometry of a stable channel with a gravel bed. *Earth Surface Processes and Landforms*, *42*, 1460–1471. doi: 10.1002/esp.4104

Graham, D. J., Reid, I., & Rice, S. P. (2005). Automated sizing of coarse-grained sediments: Image-processing procedures. *Mathematical Geology*, *37*(1), 1–28. doi: 10.1007/s11004-005-8745-x

Graham, D. J., Rice, S. P., & Reid, I. (2005). A transferable method for the automated grain sizing of river gravels. *Water Resources Research*, *41*(7), 1–12. doi: 10.1029/2004WR003868

Graham, D. J., Rollet, A. J., Piégay, H., & Rice, S. P. (2010). Maximizing the accuracy of image-based surface sediment sampling techniques. *Water Resources Research*, *46*, 1–15. doi: 10.1029/2008WR006940

Gregory, K. J., & Madew, J. R. (1982). Land-use change, flood frequency and channel adjustments. In R. D. Hey, J. C. Bathurst, & C. R. Thorne (Eds.), *Gravel-bed rivers: fluvial processes, engineering and management.* (pp. 757–781).

Harrelson, C. C., Potyondy, J. P., & Rawlins, C. L. (1994). *Stream channel reference sites: an illustrated guide to field technique.* U.S. Dept. of Agriculture, Forest Service, Rocky Mountain Forest and Range Experiment Station,. Retrieved from `http://hdl.handle.net/2027/umn.31951d030011248`

Hassan, M. A., Church, M., Lisle, T. E., Brardinoni, F., Benda, L., & Grant, G. E. (2005). Sediment transport and channel morphology of small, forested streams. *Journal of the American Water Resources Association*, *41*(4), 853–876. doi: 10.1111/j.1752-1688.2005.tb03774.x

Hawley, R. J., Bledsoe, B. P., Stein, E. D., & Haines, B. E. (2012). Channel Evolution Model of Semiarid Stream Response to Urban-Induced Hydromodification. *Journal of the American Water Resources Association*, *48*(4), 722–744. doi: 10.1111/j.1752-1688.2012.00645.x

Hey, R. D., & Thorne, C. R. (1986). Stable channels with mobile gravel beds. *Journal of Hydraulic Engineering*, *112*(8), 671–689. doi: 10.1061/(ASCE)0733-9429(1988)114:3(339)

Hoey, T. B., & Ferguson, R. (1994). Numerical simulation of downstream fining by selective transport in gravel bed rivers: Model development and illustration. *Water Resources Research*, *30*(7), 2251–2260.

Hollis, G. E. (1975). The effect of urbanization on floods of different recurrence interval. *Water Resources Research*, *11*(3), 431–435. doi: 10.1029/WR011i003p00431

IPCC. (2014). *Climate change 2014: synthesis report. Contribution of working groups I, II and III to the fifth assessment report of the Intergovernmental Panel on Climate Change* (Tech. Rep.). Geneva, Switzerland. doi: 10.1017/CBO9781139177245.003

James, M. R., & Robson, S. (2014). Mitigating systematic error in topographic models derived from UAV and ground-based image networks. *Earth Surface Processes and Landforms*, *39*(10), 1413–1420. doi: 10.1002/esp.3609

James, M. R., Robson, S., & Smith, M. W. (2017). 3-D uncertainty-based topographic change detection with structure-from-motion photogrammetry: precision maps for ground control and directly georeferenced surveys. *Earth Surface Processes and Landforms*, *42*(12), 1769–1788. doi: 10.1002/esp.4125

Julien, P. Y. (2015). Downstream hydraulic geometry of alluvial rivers. *Proceedings of the International Association of Hydrological Sciences*, *367*, 3–11. doi: 10.5194/piahs-367-3-2015

Julien, P. Y., & Wargadalam, J. (1995). Alluvial channel geometry: Theory and applications. *J. Hydraul. Eng.*, *121*(4), 312–325.

Kamphuis, J. W. (1974). Determination of sand roughness for fixed beds. *Journal of Hydraulic Research*, *12*(2), 193–203. doi: 10.1080/00221687409499737

Kellerhals, R., & Bray, D. I. (1971). Sampling procedures for coarse fluvial sediments. *Journal of the Hydraulics Division*, *97*(8), 1165–1180.

Kelley, C. (1999). *Iterative optimization*. Society for Industrial and Applied Mathematics. doi: 10.1007/978-94-007-2300-9_4

Kleinhans, M. G., & van den Berg, J. H. (2011). River channel and bar patterns explained and predicted by an empirical and a physics-based method. *Earth Surface Processes and Landforms*, *36*(6), 721–738. doi: 10.1002/esp.2090

Knighton, A. D. (1980). Longitudinal changes in size and sorting of stream- bed material in four English rivers. *Geological Society of America Bulletin*, *91*(1), 55–62. doi: 10.1130/0016-7606(1980)91⟨55:LCISAS⟩2.0.CO;2

Lague, D. (2014). The stream power river incision model: Evidence, theory and beyond. *Earth Surface Processes and Landforms*, *39*(1), 38–61. doi: 10.1002/esp.3462

Lamb, M. P., Dietrich, W. E., & Venditti, J. G. (2008). Is the critical shields stress for incipient sediment motion dependent on channel-bed slope? *Journal of Geophysical Research: Earth Surface*, *113*(2), 1–20. doi: 10.1029/2007JF000831

Lane, E. W. (1955). The importance of fluvial morphology in hydraulic engineering. *American Society of Civil Engineers, Proceedings*, *81*, 1–17. doi: 10.11475/sabo1948.1956.23

Leopold, L. B. (1970). An Improved Method for Size Distribution of Stream Bed Gravel. *Water Resources Research*, *6*(5), 1357–1366. doi: 10.1029/WR006i005p01357

Leopold, L. B., & Maddock Jr., T. (1953). *The hydraulic geometry of stream channels and some physiographic implications* (Tech. Rep.). Washington, D.C.. Retrieved from `http://pubs.er.usgs.gov/publication/pp252` doi: 10.3133/pp252

Leopold, L. B., & Wolman, M. G. (1957). *River Channel Patterns: Braided, Meandering and Straight* (Tech. Rep.). Washington, D.C.. Retrieved from `http://pubs.er.usgs.gov/publication/pp282B` doi: 10.3133/pp282B

Leopold, L. B., Wolman, M. G., & Miller, J. P. (1964). *Fluvial processes in geomorphology*. San Francisco: Freeman, New York.

Lewicki, M., Pizzuto, J. E., Moglen, G. E., & Allmendinger, N. E. (2007). A watershed scale numerical model of the impact of land use change on bed material transport in suburban Maryland, USA. *Water Resources Research*, *43*(7), 1–11. doi: 10.1029/2006WR004959

Liébault, F., & Piégay, H. (2001). Assessment of channel changes due to long term bedload supply decrease, Roubion River, France. *Geomorphology*, *36*(3-4), 167–186.

doi: 10.1016/S0169-555X(00)00044-1

Lisle, T. E., Iseya, F., & Ikeda, H. (1993). Response of a channel with alternate bars to a decrease in supply of mixed-size bed load: A flume experiment. *Water Resources Research*, *29*(11), 3623–3629.

Liverman, D. M. (2009). Conventions of climate change: constructions of danger and the dispossession of the atmosphere. *Journal of Historical Geography*, *35*(2), 279–296. Retrieved from `http://dx.doi.org/10.1016/j.jhg.2008.08.008` doi: 10.1016/j.jhg.2008.08.008

López-Vicente, M., Pérez-Bielsa, C., López-Montero, T., Lambán, L. J., & Navas, A. (2014). Runoff simulation with eight different flow accumulation algorithms: Recommendations using a spatially distributed and open-source model. *Environmental Modelling and Software*, *62*, 11–21. doi: 10.1016/j.envsoft.2014.08.025

Lynas, M. (2008). Six degrees: our future on a hotter planet. *Scitech Book News*, *32*(1). doi: 10.5860/choice.46-3260

Mackin, J. H. (1948). Concept of the graded river. *Bulletin of the Geological Society of America*, *59*, 463–512.

Martin, Y., & Church, M. (2000). Re-examination of Bagnold's empirical bedload formulae. *Earth Surface Processes and Landforms*, *25*(9), 1011–1024. doi: 10.1002/1096-9837(200008)25:9⟨1011::AID-ESP114⟩3.0.CO;2-H

Martin, Y., & Ham, D. (2005). Testing bedload transport formulae using morphologic transport estimates and field data: Lower Fraser River, British Columbia. *Earth Surface Processes and Landforms*, *30*(10), 1265–1282. doi: 10.1002/esp.1200

Martínez-Fernández, V., González, M., & Jalón, D. G. D. (2019). Selecting geomorphic variables for automatic river segmentation : Trade-offs between information gained and effort required. *Geomorphology*, *329*, 248–258. doi: 10.1016/j.geomorph.2019.01.005

Meyer-Peter, E., & Müller, R. (1948). Formulas for bed-load transport. *Proceedings of the 2nd Meeting of the International Association of Hydraulic Research*, 39–64. doi: 1948-06-07

Mizuyama, T. (1977). *Bed-load transport in steep channels* (PhD, Kyoto University). doi: 10.1007/bfb0011185

Mueller, E. N., Batalla, R. J., Garcia, C., & Bronstert, A. (2008). Modeling bed-load rates from fine grain-size patches during small floods in a gravel-bed river. *Journal of Hydraulic Engineering*, *134*(10), 1430–1439. doi: 10.1061/(ASCE)0733-9429(2008)134:10(1430)

Müller, T., & Hassan, M. A. (2018). Fluvial response to changes in the magnitude and frequency of sediment supply in a 1-D model. *Earth Surface Dynamics*(6), 1041–1057.

Nanson, G. C., & Croke, J. C. (1992). A genetic classification of floodplains. *Geomorphology*, *4*, 459–486. doi: 10.1016/0169-555X(92)90039-Q

Nanson, G. C., & Knighton, D. A. (1996). Anabranching rivers: Their cause, character and classification. *Earth Surface Processes and Landforms*, *21*(3), 217–239. doi: 10.1002/(SICI)1096-9837(199603)21:3⟨217::AID-ESP611⟩3.0.CO;2-U

Natural Resources Canada. (2015). *Canadian Digital Elevation Model, 1945-2011.* Retrieved from https://open.canada.ca/data/en/dataset/7f245e4d-76c2-4caa-951a-45d1d2051333

Natural Resources Canada. (2016a). *National Hydro Network, GeoBase Series.* Retrieved from https://open.canada.ca/data/en/dataset/a4b190fe-e090-4e6d-881e-b87956c07977

Natural Resources Canada. (2016b). *Pipelines across Canada.* Retrieved 2018-01-12, from https://www.nrcan.gc.ca/our-natural-resources/energy-sources-distribution/clean-fossil-fuels/pipelines/pipelines-across-canada/18856

Neupane, S., & Yager, E. M. (2013). Numerical simulation of the impact of sediment supply and streamflow variations on channel grain sizes and Chinook salmon habitat in mountain drainage networks. *Earth Surface Processes and Landforms*, *38*(15), 1822–1837. doi: 10.1002/esp.3426

Neverman, A. J., Fuller, I. C., Procter, J. N., & Death, R. G. (2019). Terrestrial laser scanning and structure-from-motion photogrammetry concordance analysis for describing the surface layer of gravel beds. *Progress in Physical Geography*, *43*(2), 260–281. doi: 10.1177/0309133318822966

New, M., Liverman, D., Schroder, H., & Anderson, K. (2011). Four degrees and beyond: The potential for a global temperature increase of four degrees and its implications. *Philosophical Transactions of the Royal Society A: Mathematical, Physical and Engineering Sciences*, *369*(1934), 9–19. doi: 10.1098/rsta.2010.0303

Nielsen, A., Bolding, K., Hu, F., & Trolle, D. (2017). An open source QGIS-based workflow for model application and experimentation with aquatic ecosystems. *Environmental Modelling and Software*, *95*, 358–364. doi: 10.1016/j.envsoft.2017.06.032

Nitsche, M., Rickenmann, D., Turowski, J. M., Badoux, A., & Kirchner, J. W. (2011). Evaluation of bedload transport predictions using flow resistance equations to account for macro-roughness in steep mountain streams. *Water Resources Research*, *47*(8). doi: 10.1029/2011WR010645

O'Connor, J., Smith, M. J., & James, M. R. (2017). Cameras and settings for aerial surveys in the geosciences: Optimising image data. *Progress in Physical Geography*, *41*(3), 325–344. doi: 10.1177/0309133317703092

Olivera, F., Valenzuela, M., Srinivasan, R., Choi, J., Cho, H., Koka, S., & Agrawal, A.

(2006). ArcGIS-SWAT: A geodata model and GIS interface for SWAT. *Journal of the American Water Resources Association*, *42*(2), 295–309. doi: 10.17660/actahortic.2011.893.75

Papanicolaou, A. N., Bdour, A., & Wicklein, E. (2004). One-dimensional hydrodynamic/sediment transport model applicable to steep mountain streams. *Journal of Hydraulic Research*, *42*(4), 357–375. doi: 10.1080/00221686.2004.9728402

Parker, C., Clifford, N. J., & Thorne, C. R. (2011). Understanding the influence of slope on the threshold of coarse grain motion: Revisiting critical stream power. *Geomorphology*, *126*(1-2), 51–65. doi: 10.1016/j.geomorph.2010.10.027

Parker, C., Thorne, C. R., & Clifford, N. J. (2015). Development of ST: REAM: A reach-based stream power balance approach for predicting alluvial river channel adjustment. *Earth Surface Processes and Landforms*, *40*(3), 403–413. doi: 10.1002/esp.3641

Parker, G. (1990). Surface-based bedload transport relation for gravel rivers. *Journal of Hydraulic Research*, *28*(4), 417–436. doi: 10.1080/00221689009499058

Parker, G. (1991). Selective sorting and abrasion of river gravel. I: Theory. *Journal of Hydraulic Engineering*, *117*(2), 131–147. doi: 10.1061/(ASCE)0733-9429(1991)117:2(131)

Parker, G. (2004). *1D sediment transport morphodynamics with applications to rivers and turbidity currents, Copyrighted e-book.* Retrieved from `http://hydrolab.illinois.edu/people/parkerg/default.asp`

Parker, G. (2006). Transport of gravel and sediment mixtures, chapter 3. In *Sedimentation engineering* (pp. 165–252). Retrieved from `http://dx.doi.org/10.1061/9780784408148.ch03{%}0Ahttp://ascelibrary.org/doi/book/10.1061/9780784408230` doi: 10.1061/9780784408230

Parker, G., & Klingeman, P. C. (1982). On why gravel bed streams are paved. *Water Resources Research*, *18*(5), 1409–1423. doi: 10.1029/WR018i005p01409

Petit, F., Gob, F., Houbrechts, G., & Assani, A. A. (2005). Critical specific stream power in gravel-bed rivers. *Geomorphology*, *69*(1-4), 92–101. doi: 10.1016/j.geomorph.2004.12.004

Petit, F., Houbrechts, G., Peeters, A., Hallot, E., Van Campenhout, J., & Denis, A. C. (2015). Dimensionless critical shear stress in gravel-bed rivers. *Geomorphology*, *250*, 308–320. doi: 10.1016/j.geomorph.2015.09.008

Powell, D. M. (2014). Flow resistance in gravel-bed rivers: Progress in research. *Earth-Science Reviews*, *136*, 301–338. doi: 10.1016/j.earscirev.2014.06.001

Prancevic, J. P., & Lamb, M. P. (2015). Unraveling bed slope from relative roughness in initial sediment motion. *Journal of Geophysical Research : Earth Surface*, 474–489. doi: 10.1002/2014JF003323.Received

Purinton, B., & Bookhagen, B. (2019). Introducing PebbleCounts: A grain-sizing tool for photo surveys of dynamic gravel-bed rivers. *Earth Surface Dynamics*, *7*(3), 859–877. doi: 10.5194/esurf-7-859-2019

Radice, A., Giorgetti, E., Brambilla, D., Longoni, L., & Papini, M. (2012). On integrated sediment transport modelling for flash events in mountain environments. *Acta Geophysica*, *60*(1), 191–213. doi: 10.2478/s11600-011-0063-8

Rahuel, J., Holly, F., Chollet, J., Belleudy, P., & Yang, G. (1989). Modeling of riverbed evolution for bedload sediment mixtures. *Journal of Hydraulic Engineering*, *115*(11), 1521–1542. doi: 10.1061/(ASCE)0733-9429(1989)115:11(1521)

Recking, A. (2009). Theoretical development on the effects of changing flow hydraulics on incipient bed load motion. *Water Resources Research*, *45*(4), 1–16. doi: 10.1029/2008WR006826

Rice, S. (1995). *The spatial variation and routine sampling of spawning gravels in small coastal streams.* Retrieved from https://www.for.gov.bc.ca/hfd/pubs/Docs/Wp/Wp06.htm

Rice, S. (1998). Which tributaries disrupt downstream fining along gravel-bed rivers? *Geomorphology*, *22*(1), 39–56. doi: 10.1016/S0169-555X(97)00052-4

Rice, S. P., & Church, M. (2001). Longitudinal profiles in simple alluvial systems. *Water Resources Research*, *37*(2), 417–426. doi: 10.1029/2000WR900266

Rickenmann, D. (2001). Comparison of bed load transport in torrents and gravel bed streams. *Water Resources Research*, *37*(12), 3295–3305.

Rinaldi, M., Surian, N., Comiti, F., & Bussettini, M. (2013). A method for the assessment and analysis of the hydromorphological condition of Italian streams: The Morphological Quality Index (MQI). *Geomorphology*, *180-181*, 96–108. doi: 10.1016/j.geomorph.2012.09.009

Roux, C., Alber, A., Bertrand, M., Vaudor, L., & Piégay, H. (2015). "FluvialCorridor": A new ArcGIS toolbox package for multiscale riverscape exploration. *Geomorphology*, *242*, 29–37. doi: 10.1016/j.geomorph.2014.04.018

Rubin, D. M. (2004). A simple autocorrelation algorithm for determining grain size from digital images of sediment. *Journal of Sedimentary Research*, *74*(1), 160–165. doi: 10.1306/052203740160

Saletti, M., Molnar, P., Zimmermann, A., Hassan, M. A., & Michael, C. (2015). Temporal variability and memory in sediment transport in an experimental step-pool channel. *Water Resources Research*, *51*(11), 9325–9337. doi: 10.1002/2015WR016929

Sangireddy, H., Stark, C. P., Kladzyk, A., & Passalacqua, P. (2016). GeoNet: An open source software for the automatic and objective extraction of channel heads, channel network, and channel morphology from high resolution topography data. *Environmental Modelling and Software*, *83*, 58–73. doi: 10.1016/j.envsoft.2016.04.026

Schleyer, R. (1987). Goodness-of-fit to ideal Gauss and Rosin distributions–a new grain size parameter. *Journal of Sedimentary Petrology*, *57*(5), 871–880. Retrieved from http://search.proquest.com/docview/24464042/

Schneider, J. M., Rickenmann, D., Turowski, J. M., Schmid, B., & Kirchner, J. W. (2016). Bed load transport in a very steep mountain stream (Riedbach, Switzerland): Measurement and prediction. *Water Resources Research*, *52*(12), 9522–9541. doi: 10.1002/2016WR019308

Schumm, S., & Harvey, M. (2008). Engineering geomorphology. In M. H. García (Ed.), *Sedimentation engineering: Processes, measurements, modeling, and practice* (pp. 859–883). American Society of Civil Engineers.

Schumm, S. A. (1963). *A tentative classification of alluvial river channels an examination of similarities and differences among some Great Plains rivers* (- ed.; Tech. Rep.). Retrieved from http://pubs.er.usgs.gov/publication/cir477 doi: 10.3133/cir477

Schumm, S. A. (1977). *The fluvial system*. New York: Wiley.

Schumm, S. A. (1984). *Incised channels : morphology, dynamics, and control*. Littleton, Colo: Water Resources Publications.

Schumm, S. A. (1985). Patterns of alluvial rivers. *Annual Review of Earth and Planetary Sciences*, *13*, 5–27. doi: 10.1146/annurev.ea.13.050185.000253

Schwanghart, W., & Kuhn, N. J. (2010). TopoToolbox: A set of Matlab functions for topographic analysis. *Environmental Modelling and Software*, *25*(6), 770–781. doi: 10.1016/j.envsoft.2009.12.002

Shields, A. (1936). *Anwendung der Aehnlichkeitsmechanik und der Turbulenzforschung auf die Geschiebebewegung* (Tech. Rep.). Retrieved from http://resolver.tudelft.nl/uuid:61a19716-a994-4942-9906-f680eb9952d6

Shvidchenko, A. B., & Pender, G. (2000). Flume study of the effect of relative depth on the incipient motion of coarse uniform sediments. *Water Resources Research*, *36*(2), 619–628.

Smith, M. W., Carrivick, J. L., & Quincey, D. J. (2015). Structure from motion photogrammetry in physical geography. *Progress in Physical Geography*, *40*(2), 247–275. doi: 10.1177/0309133315615805

Snow, R. S., & Slingerland, R. L. (1987). Mathematical modeling of graded river profiles. *Journal of Geology*, *95*(1), 15–33. doi: 10.1086/629104

Soar, P. J., Wallerstein, N. P., & Thorne, C. R. (2017). Quantifying river channel stability at the basin scale. *Water (Switzerland)*, *9*(2), 1–31. doi: 10.3390/w9020133

Sofia, G., Tarolli, P., Cazorzi, F., & Fontana, G. D. (2015). Downstream hydraulic geometry relationships : Gathering reference reach-scale width values from LiDAR. *Geomorphology*, *250*, 236–248. doi: 10.1016/j.geomorph.2015.09.002

Spencer, T., & Lane, S. N. (2017). Reflections on the IPCC and global change science: Time for a more (physical) geographical tradition. *Canadian Geographer*, *61*(1), 124–135. doi: 10.1111/cag.12332

Stähly, S., Friedrich, H., & Detert, M. (2017). Size ratio of fluvial grains' intermediate axes assessed by image processing and square-hole sieving. *Journal of Hydraulic Engineering*, *143*(6), 1–6. doi: 10.1061/(ASCE)HY.1943-7900.0001286

Statistics Canada. (2015). *Canada goes urban.* Retrieved 2018-05-17, from `https://www150.statcan.gc.ca/n1/pub/11-630-x/11-630-x2015004-eng.htm`

Statistics Canada. (2018). *Ecological Land Classification, 2017.* Retrieved from `https://www.statcan.gc.ca/eng/subjects/standard/environment/elc/12-607-x2018001-eng.pdf` doi: Catalogueno.12-607-XISBN978-0-660-24501-0

Strom, K. B., Kuhns, R. D., & Lucas, H. J. (2010). Comparison of automated image-based grain sizing to standard pebble-count methods. *Journal of Hydraulic Engineering*, *136*(8), 461–473. doi: 10.1061/(asce)hy.1943-7900.0000198

Sturm, T. W. (2010). *Open channel hydraulics* (2nd ed. ed.). Dubuque, IA: McGraw-Hill.

Tarboton, D. G., Schreuders, K. A., Watson, D. W., & Baker, M. E. (2009). Generalized terrain-based flow analysis of digital elevation models. *18th World IMACS Congress and MODSIM09 International Congress on Modelling and Simulation: Interfacing Modelling and Simulation with Mathematical and Computational Sciences, Proceedings*(July), 2000–2006.

Toro-Escobar, C. M., Paola, C., & Parker, G. (1996). Transfer function for the deposition of poorly sorted gravel in response to streambed aggradation. *Journal of Hydraulic Research*, *34*(1), 35–53.

United States Bureau Reclamation. (2006). Chapter 5 - Sediment modeling for rivers and reservoirs. In Bureau of Reclamation U.S. Dept. of the Interior (Ed.), *Erosion and sedimentation manual* (pp. 5–1 – 5–93). Washington, D.C.: Sedimentation and River Hydraulics Group. doi: 10.1061/(ASCE)0733-9429(1999)125:5(554)

van den Berg, J. H. (1995). Prediction of alluvial channel pattern of perennial rivers. *Geomorphology*, *12*, 259–279. doi: 10.1016/0169-555X(95)00014-V

Vanoni, V. A. (1964). *Measurements of critical shear stress for entraining fine sediments in a boundary layer.* Pasadena, California: California Institute of Technology.

Vázquez-Tarrío, D., Borgniet, L., Liébault, F., & Recking, A. (2017). Using UAS optical imagery and SfM photogrammetry to characterize the surface grain size of gravel bars in a braided river (Vénéon River, French Alps). *Geomorphology*, *285*, 94–105. doi: 10.1016/j.geomorph.2017.01.039

Vetsch, D., Siviglia, A., Caponi, F., Ehrbar, D., Gerke, E., Kammerer, S., … Faer, R. (2018). *System Manuals of BASEMENT.* Laboratory of Hydraulics, Glaciology and Hydrology (VAW). ETH Zurich. Retrieved from `http://www.basement.ethz.ch`

Vianello, A., & D'Agostino, V. (2007). Bankfull width and morphological units in an alpine stream of the dolomites (Northern Italy). *Geomorphology*, *83*(3-4), 266–281. doi: 10.1016/j.geomorph.2006.02.023

Viparelli, E., Idraulica, I., Cantelli, A., Wilcock, P. R., & Parker, G. (2010). River morphodynamics with creation / consumption of grain size stratigraphy 2: numerical model. *Journal of Hydraulic Research*, *48*(6), 727–741. doi: 10.1080/00221686.2010.526759

Warrick, J. A., Rubin, D. M., Ruggiero, P., Harney, J. N., Draut, A. E., & Buscombe, D. (2009). Cobble cam: grain-size measurements of sand to boulder from digital photographs and autocorrelation analyses. *Earth Surface Processes and Landforms*, *34*, 1811–1821. doi: 10.1002/esp

Whipple, K. X., & Tucker, G. E. (1999). Dynamics of the stream-power river incision model: Implications for height limits of mountain ranges, landscape response timescales, and research needs. *Journal of Geophysical*, *104*, 661–674.

Wickert, A. D., & Schildgen, T. F. (2019). Long-profile evolution of transport-limited gravel-bed rivers. *Earth Surface Dynamics*, *7*, 17–43.

Wilcock, P. R., & Crowe, J. C. (2003). Surface-based transport model for mixed-size sediment. *Journal of Hydraulic Engineering*, *129*, 120 – 128. doi: 10.1061/(ASCE)0733-9429(2003)129:2(120)

Williams, G. (1983). Paleohydrological methods and some examples from Swedish fluvial environments. I. Cobble and boulder deposits. *Geografiska Annaler*, *65*(3), 227–243. doi: 10.1080/04353676.1983.11880088

Williams, G. P. (1978). Bank-full discharge of rivers. *Water Resources Research*, *14*(6), 1141–1154. doi: 10.1029/WR014i006p01141

Wilson, J. P., Lam, C. S., & Deng, Y. (2007). Comparison of the performance of flow-routing algorithms used in GIS-based hydrologic analysis. *Hydrological Processes*, *21*, 1026–1044. doi: 10.1002/hyp.6277

Wohl, E. (2015). Particle dynamics: The continuum of bedrock to alluvial river segments. *Geomorphology*, *241*, 192–208. doi: 10.1016/j.geomorph.2015.04.014

Wohl, E., Kuzma, J. N., & Brown, N. E. (2004). Reach-scale channel geometry of a mountain river. *Earth Surface Processes and Landforms*, *29*, 969–981. doi: 10.1002/esp.1078

Wolman, M. G. (1954). A method of sampling coarse river-bed material. *Transactions, American Geophysical Union*, *35*(6), 951–956. doi: 10.1029/TR035i006p00951

Wolman, M. G., & Leopold, L. B. (1957). River flood plains : Some observations on their formation. *United States Government Printing Office*, *282-C*, 87–107. doi: 10.3133/pp282C

Woodget, A. S., & Austrums, R. (2017). Subaerial gravel size measurement using topographic data derived from a UAV-SfM approach. *Earth Surface Processes and Landforms*, *42*(9), 1434–1443. doi: 10.1002/esp.4139

Wu, W., & Wang, S. S. (2007). One-dimensional modeling of dam-break flow over movable beds. *Journal of Hydraulic Engineering*, *133*(1), 48–58. doi: 10.1061/(ASCE)0733-9429(2007)133

Wu, W., & Wang, S. S. (2008). One-dimensional explicit finite-volume model for sediment transport with transient flows over movable beds. *Journal of Hydraulic Research*, *46*(1), 87–98. doi: 10.1080/00221686.2008.9521846

Yager, E. M., Dietrich, W. E., Kirchner, J. W., & McArdell, B. W. (2012). Prediction of sediment transport in step-pool channels. *Water Resources Research*, *48*(1), 1–20. doi: 10.1029/2011WR010829

Yager, E. M., Kirchner, J. W., & Dietrich, W. E. (2007). Calculating bed load transport in steep boulder bed channels. *Water Resources Research*, *43*(7), 1–24. doi: 10.1029/2006WR005432

APPENDICES

Appendix A

Chauncey Creek River Geometry

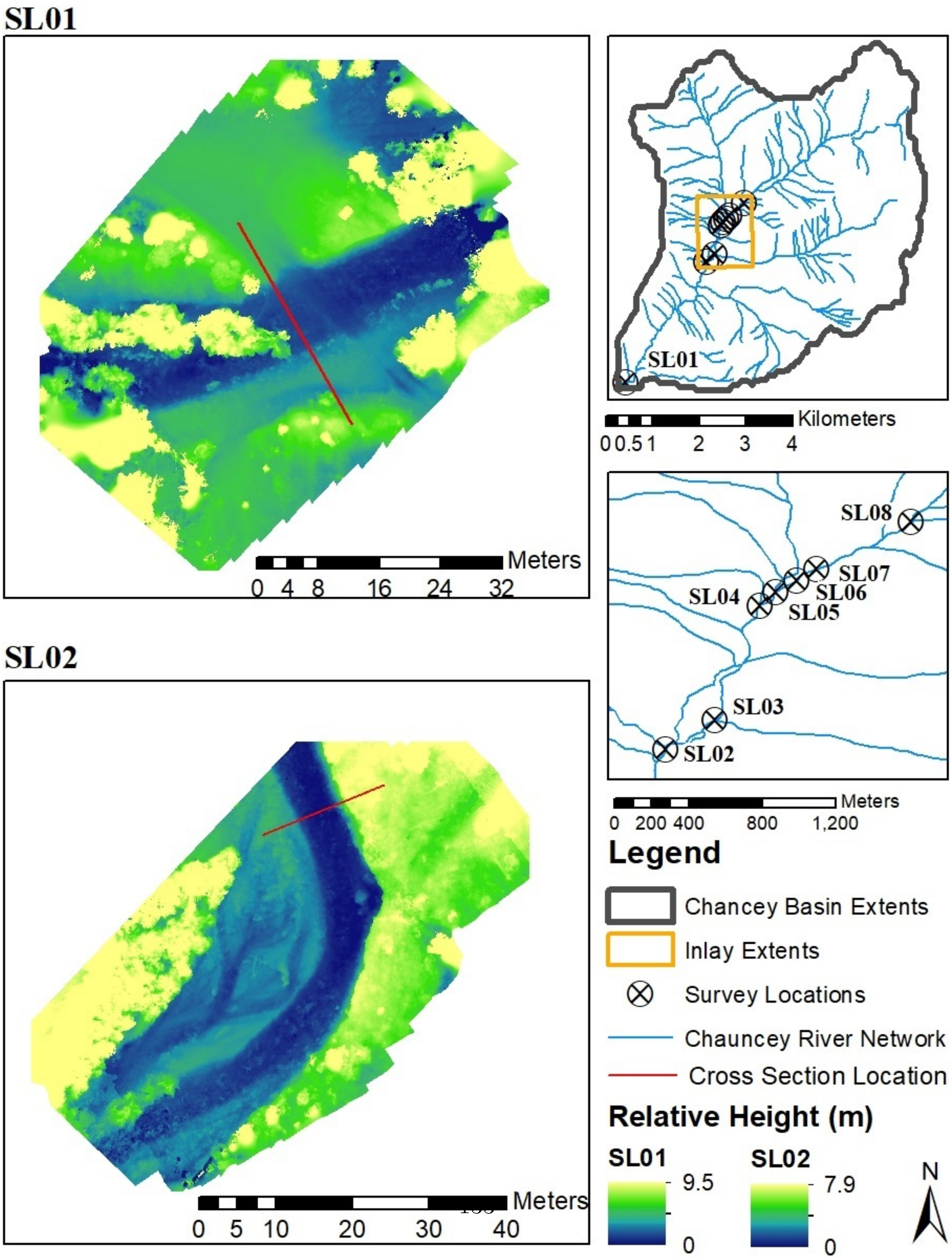

Figure A-1: SL01 and SL02 digital elevation models and cross section locations

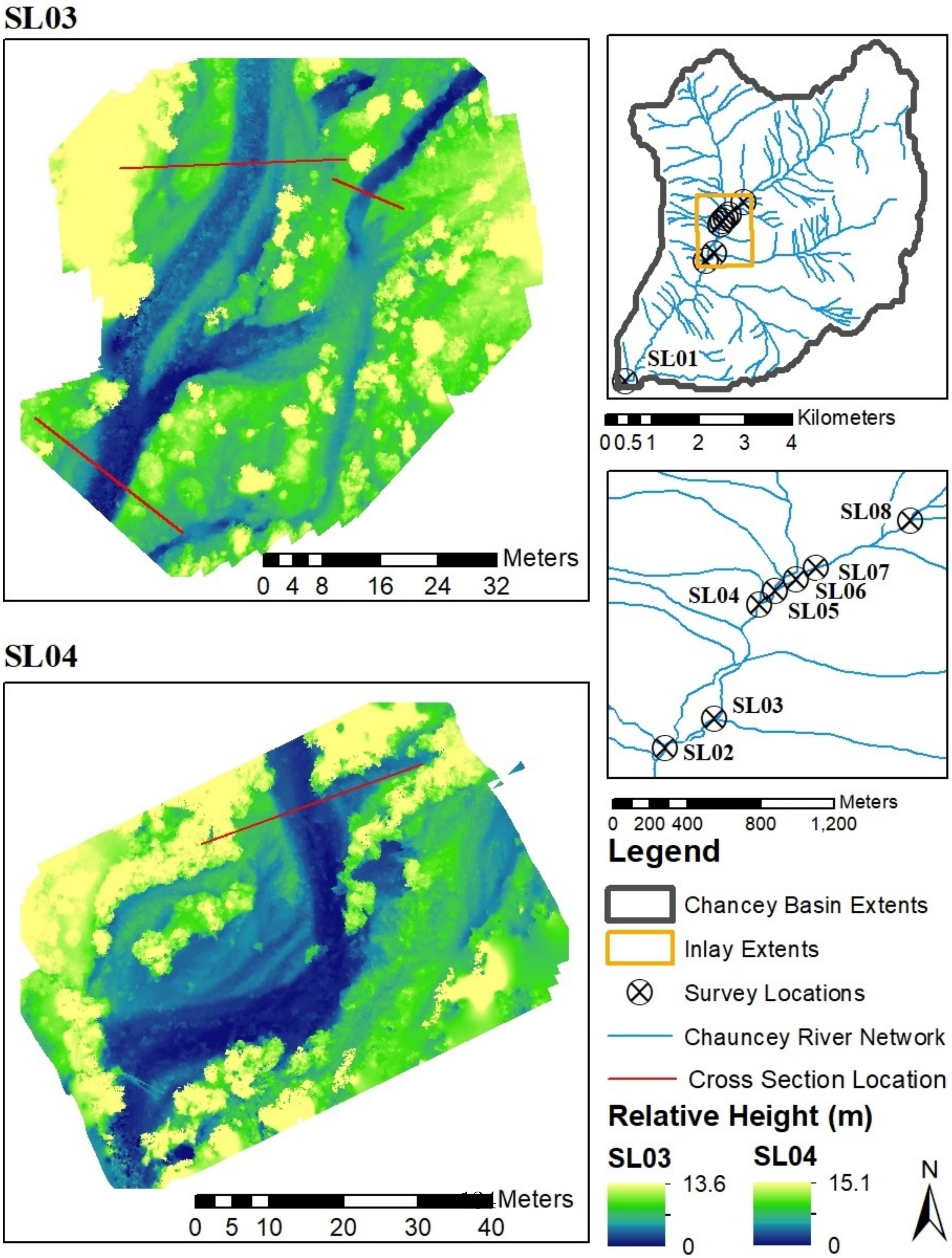

Figure A-2: SL03 and SL04 digital elevation models and cross section locations

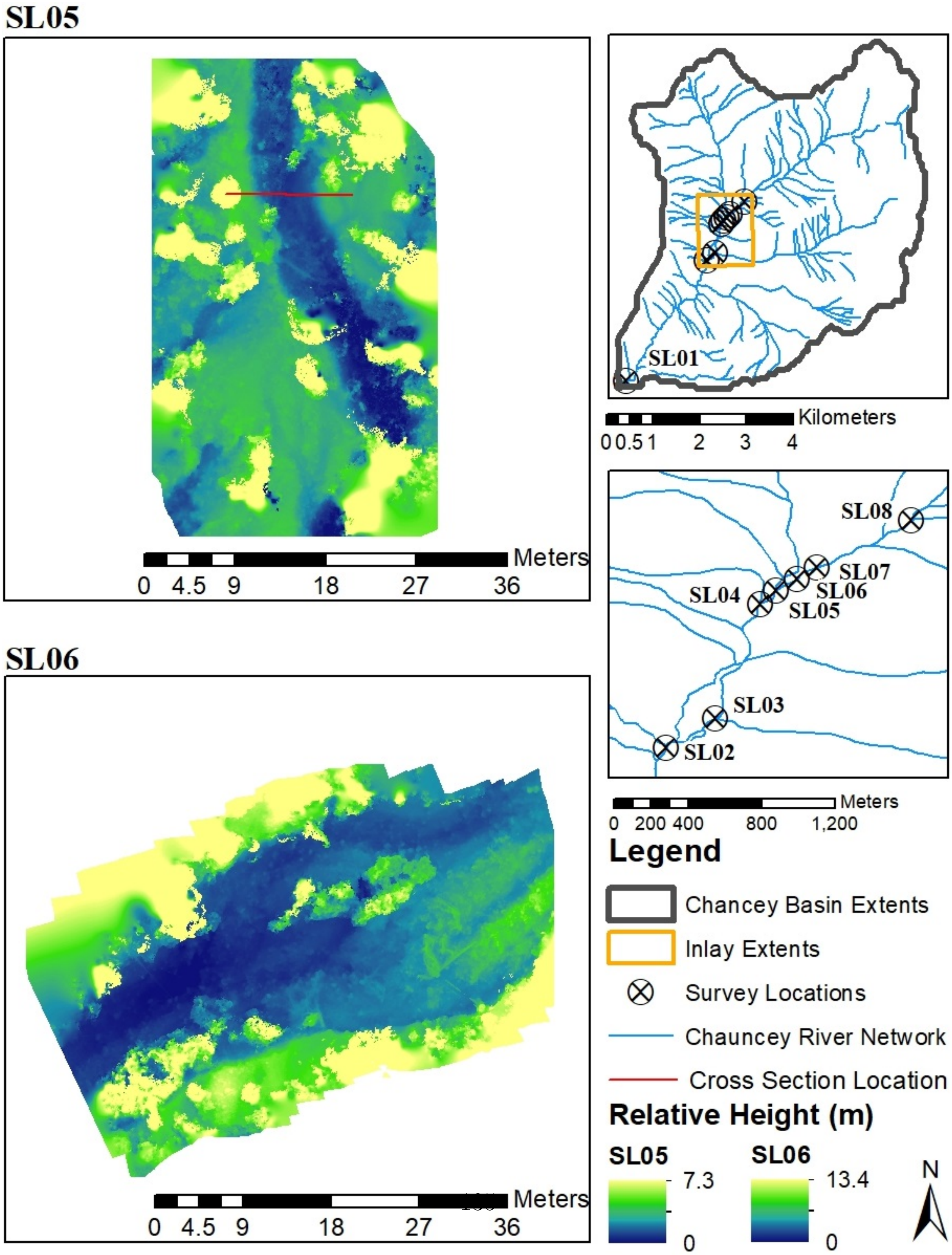

Figure A-3: SL05 and SL06 digital elevation models and cross section locations

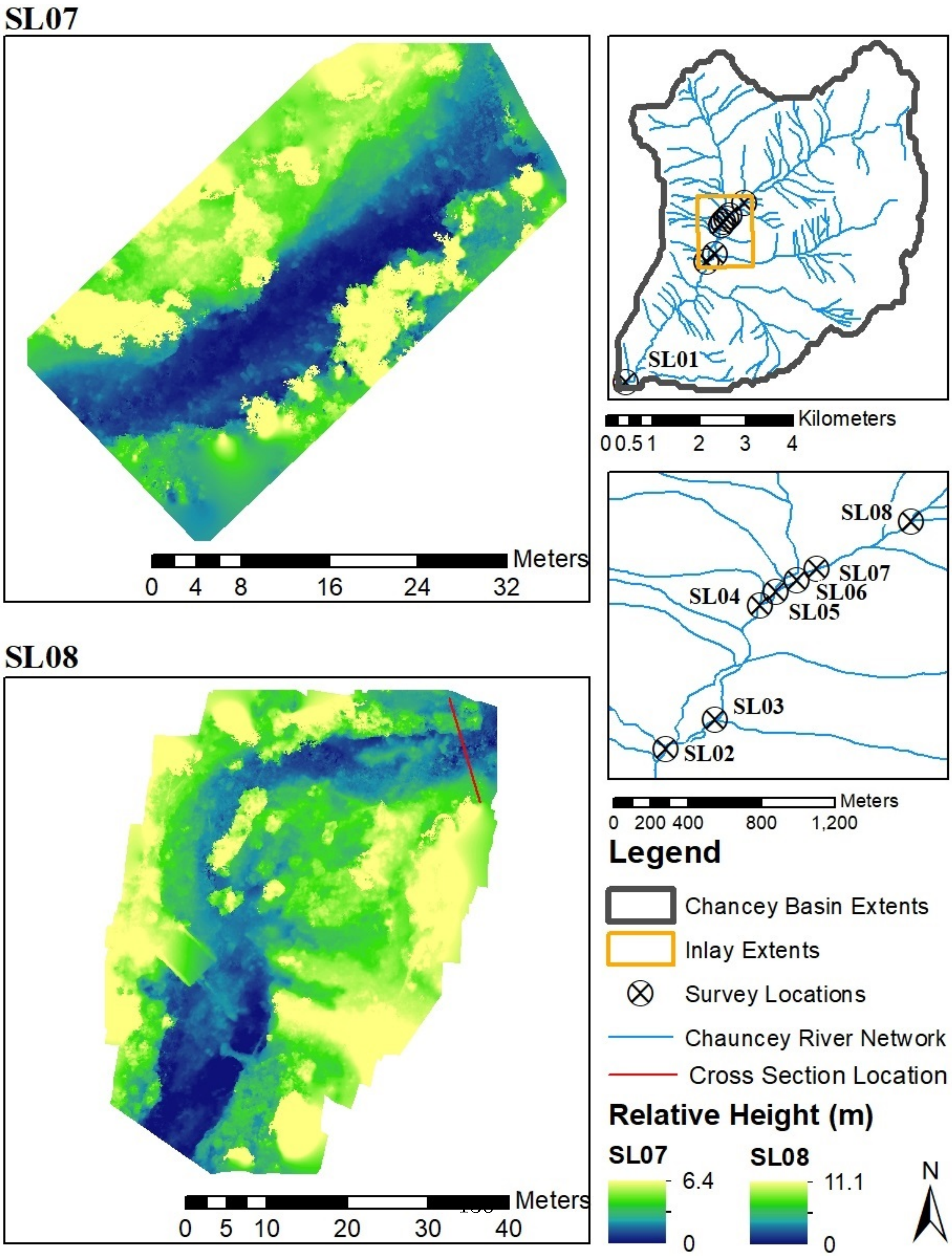

Figure A-4: SL07 and SL08 digital elevation models and cross section locations

Appendix B

Chauncey Creek Photoseiving Locations

Areas that were measured in BASEGRAIN are displayed with a rectangle. Red rectangles indicate measurements that were combined and used to represent the surficial GSD at each survey location.

Figure B-1: Photosieving locations at SL01

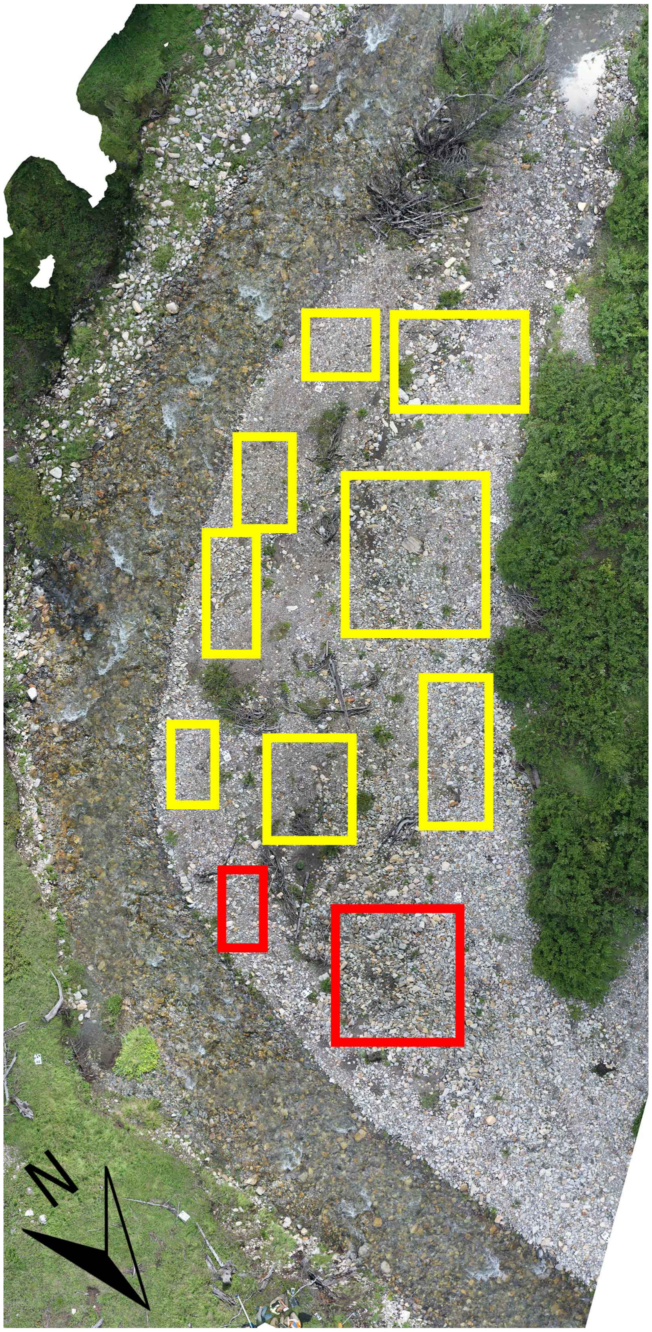

Figure B-2: Photosieving locations at SL02

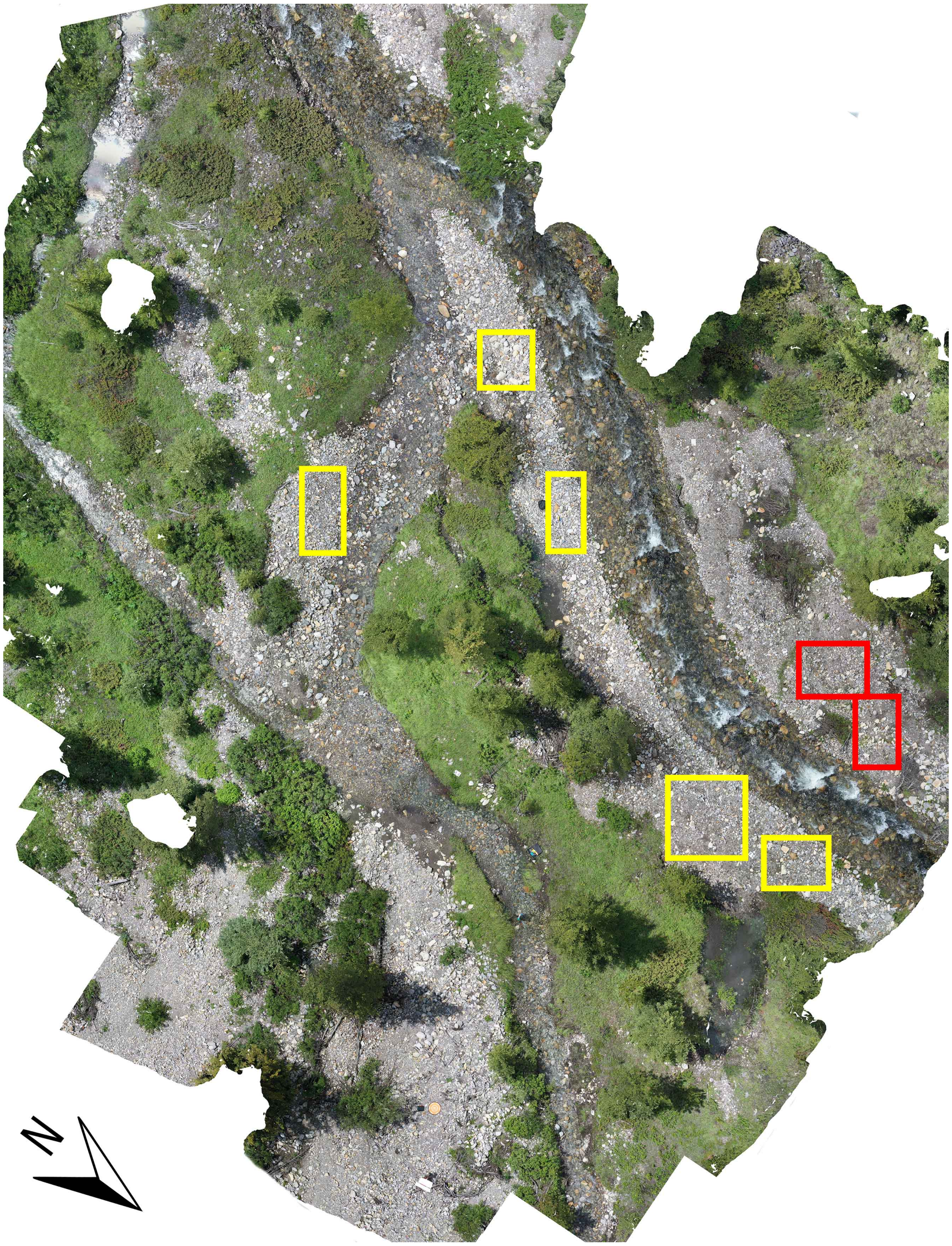

Figure B-3: Photosieving locations at SL03

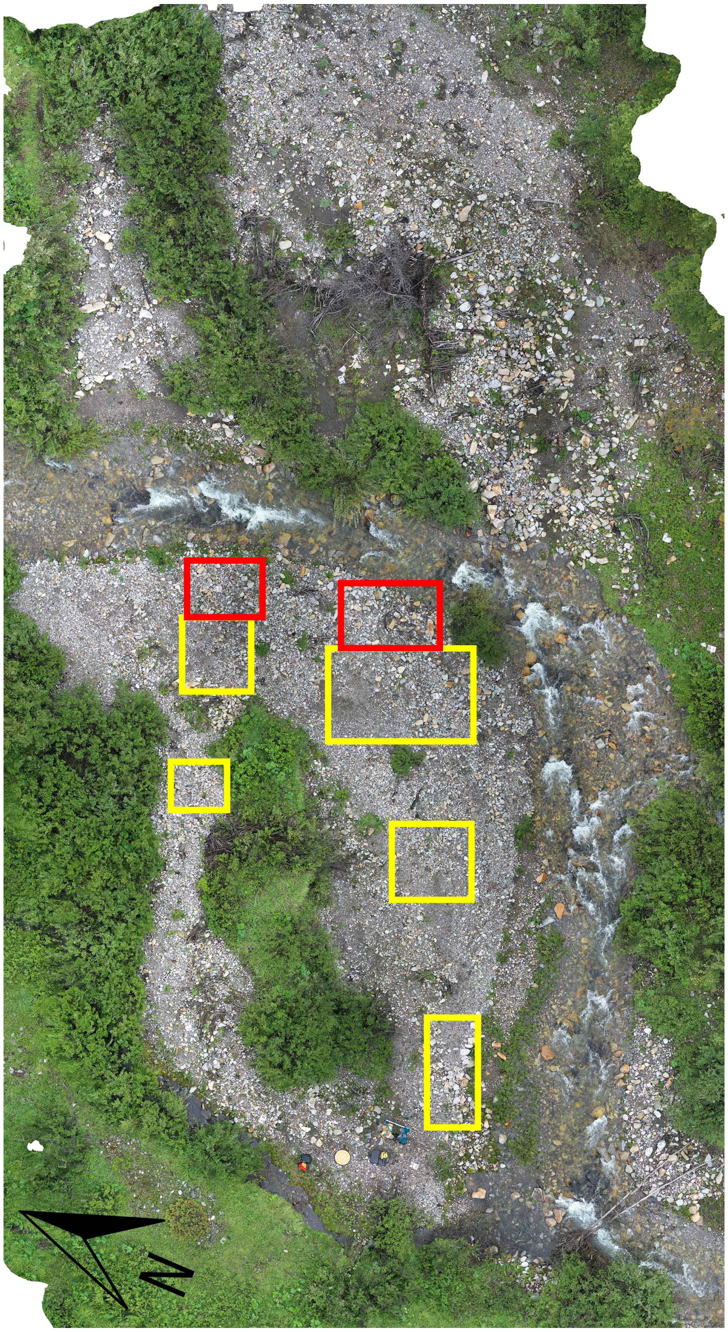

Figure B-4: Photosieving locations at SL04

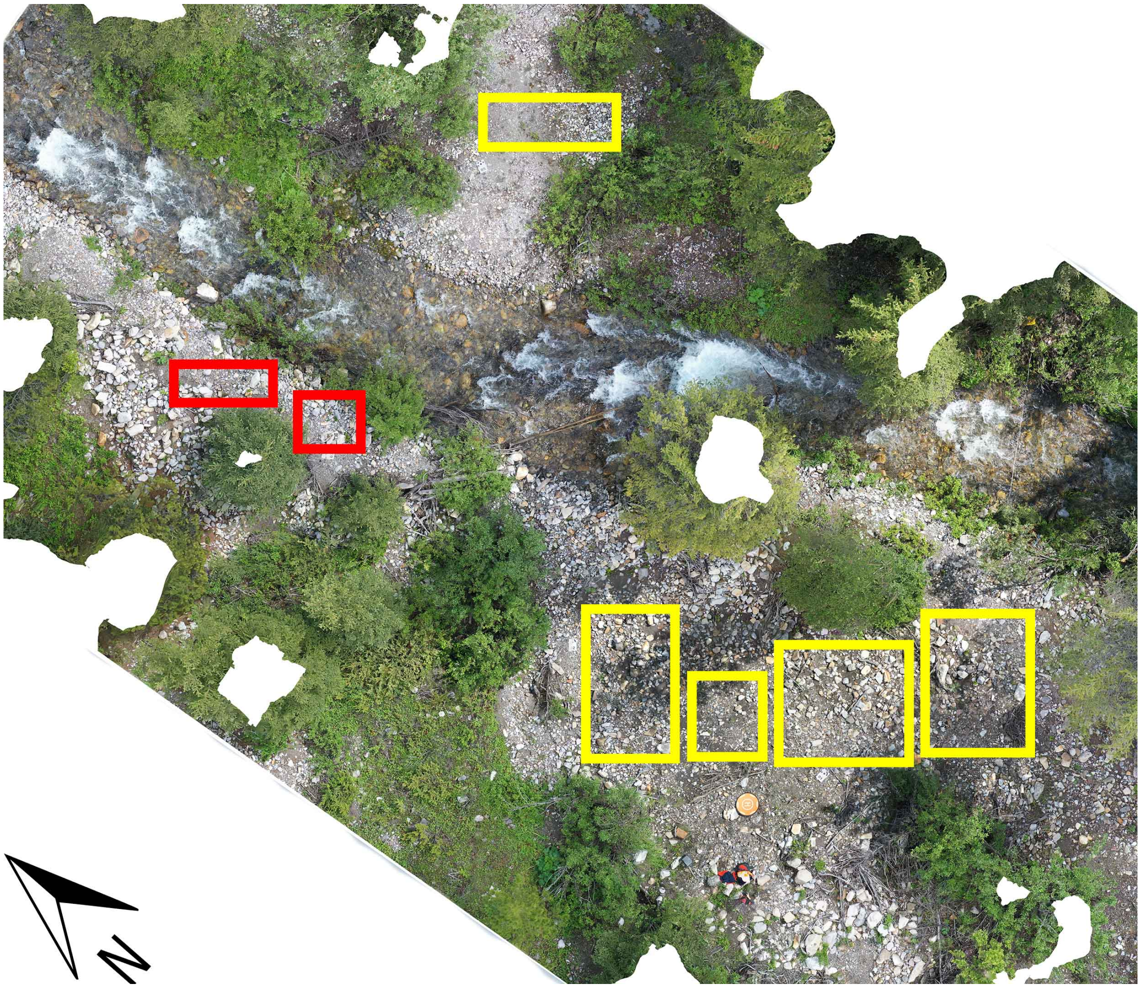

Figure B-5: Photosieving locations at SL05

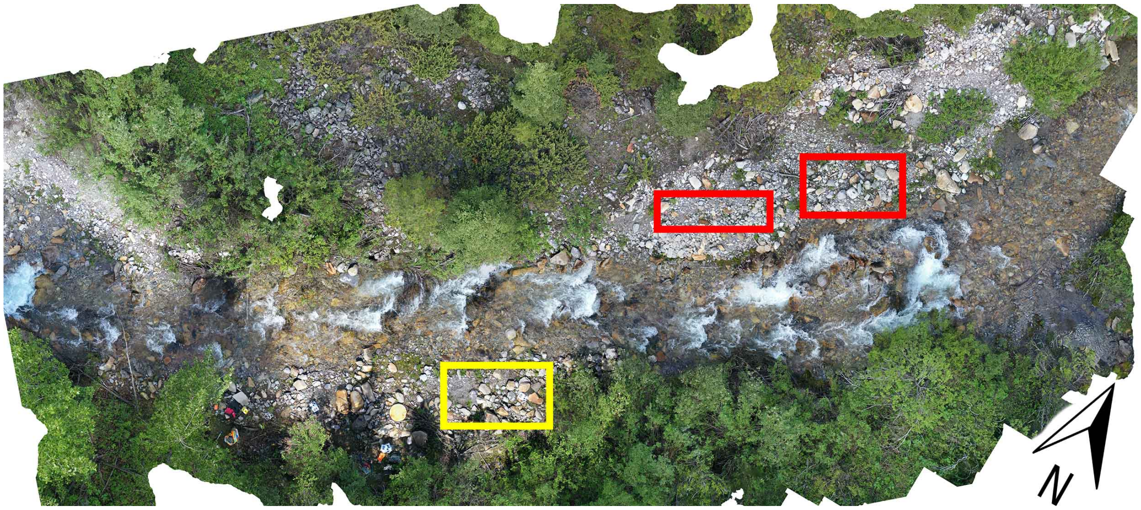

Figure B-6: Photosieving locations at SL07

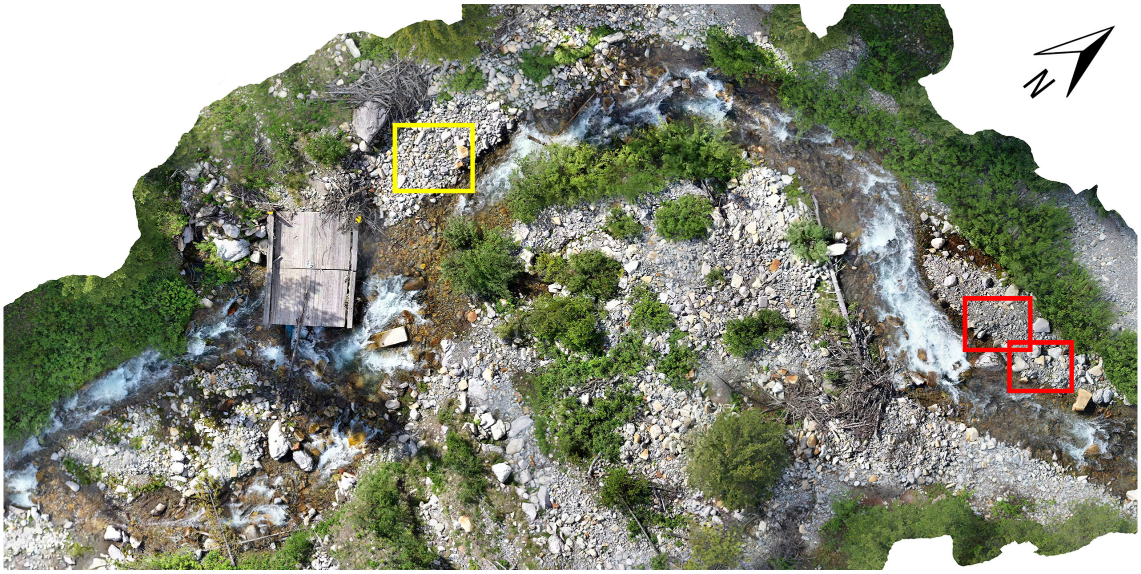

Figure B-7: Photosieving locations at SL08

Appendix C

Software Work Flows

C.1 Photogrammetry work flow: Agisoft

1. Rename photos to include site number, height above landing pad, camera orientation, and a sequential number. A Windows batch script was written to automate this process.
2. Import all photos from a single survey location into Agisoft.
3. Disable all unnecessary photos such as duplicates and photos that do not include exposed sediment.
4. **Estimate Image Quality** of all photos.
5. Disable photos with low quality. A lower quality limit, such as 0.8, could be set. However, it was found that photo quality was generally consistent for an entire survey location and in some cases the lower limit should be adjusted to prevent large sets of photos from being removed.
6. **Autodetect Markers** with a tolerance of 100 to locate as many markers as can be detected.

7. Check marker detection and manually add missing markers to all photos that contain markers that were not detected.

8. Apply a mask to photos that contain people or objects that move between photos.

9. **Align Photos** with high quality accuracy and reference preselection.

10. **Build Dense Cloud** with high quality.

11. **Build DEM** using a local projected coordinate system. NAD83(CSRS) / UTM Zone 11N (ESPG::2955) was used for Chauncey Creek.

12. Get camera distances relative to points directly below the camera locations. This was automated using a Python script.

13. Geometry can be measured directly in Agisoft, or in ArcGIS with an export of the DEM.

14. Optional: **Build Mesh**, **Build Texture**, and **Build Orthomosaic** to produce additional visuals and graphics

C.2 Photosieving work flow: BASEGRAIN

1. Select the photo that will be analyzed. If the photo does not include a known measurement, input the calculated pixel resolution for the photo.

2. Scale the photo with a known measurement with the scale function.

3. Select a particle detection zone to the desired sediment patch using **Crop Section**. The area should primarily be exposed sediment with minimal distruptions such as woody debris or water surfaces. When possible, the particle detection zone should cover and area between 200 and 400 times the size of the largest particle (Graham et al., 2010).

4. Select a test region that includes typical particles within the particle detection zone using **Test Crop Section**.

5. Visually check the performance of the particle detection. If performance is poor, adjust the following parameters and check new performance:

   - facgraythr1 (increase if under-segmented)
   - medfiltsiz10 (decrease if under-segmented)
   - AreaCutWW (increase if under-segmented)

6. Make manual adjustedments with a focus on the largest clasts

7. Adjust the results analysis so **btrunc** matches the minimum detectable grain size.

8. Export results as CSV for post processing.

Glossary

active channel The portion of the bed regularly disturbed by flow. 7

autocorrelation A method of measuring surficial grain size distributions using statistical properties in photos such as contrast and pixel intensity. 19

b'-axis The second-longest axis of a particle when measured using a photosieving method. 38, 55

b-axis The second-longest axis of a particle. This dimension is also referred to as the intermediate axis or grain diameter. 27, 28, 38

bankfull discharge The discharge that flows in a channel without overtopping the banks and partially flowing over the floodplain. 7

decoupled A term to describe a model that has two or more variables that are updated separately for each iteration of the model. 17, 58

dominant discharge The flow associated with the peak of cumulative sediment transport for a given streamflow magnitude and frequency of occurrence. It is the discharge that is generally doing the work (sediment transport) that results in the average morphologic characteristics of alluvial channels. 7

gravelometer A metal template with square holes cut in it to match half Ψ class measurements. 27, 29

ground sampling distance The distance on the ground between pixel centres in a photo. 30

incipient motion The flow condition when the force of water is just strong enough to move sediment of a particular size. 14, 16

modified cube model A modified version of the voidless cube model which accounts for bias when comparing area-by-weight to grid-by-number or volume-by-weight methods. 36

nadir The direction a camera is pointing when it is pointed straight down toward the ground. 33, 34

over-segmentation A result in automatic photosieving where a single particle is defined as multiple smaller particles. 45, 55

photosieving A method of calculating grain size distribution properties using close-range photographs. 3, 30, 38

robotic photoseiving A method of automating photoseiving algorithms using structure-from-motion software to scale photos. 32

sediment link A river segment that is delineated based on water and sediment load sources such as alluvial fans, large tributaries, and non-alluvial inputs. 11, 23, 114

stream power index An index of unit stream power that is calculated from catchment area, channel slope, and channel width. xii, 45, 74, 75, 82, 83

supply-limited A descriptor of alluvial channels that have a capacity to transport sediment that exceeds the supply of sediment. 12

transport-limited A descriptor of alluvial channels that have a sediment supply that exceeds the capacity to transport sediment. 12, 111

under-segmentation A result in automatic photosieving where multiple particles are defined as a single large particle. 45, 55

voidless cube model Geometric relationships that can be used for comparing sediment sampling method. 35, 36

Wolman pebble count A field method for determining the size of coarse material on the bed of a stream whereby a researcher walks in a preset path and records the size of a pebble below their large toe. iv, xi, 18, 25, 27–29, 36, 38, 46, 114